The Inversion of Geodetic Data for Earthquake Parameters

Thesis by

Rowena Lohman

In Partial Fulfillment of the Requirements

for the Degree of

Doctor of Philosophy

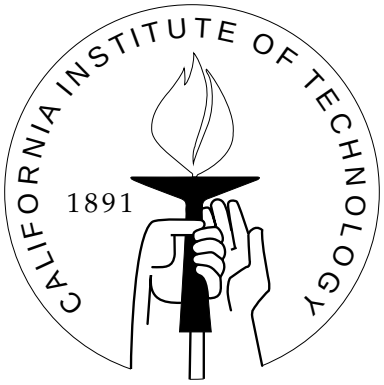

California Institute of Technology

Pasadena, California

2004

(Submitted 5/19/2004)

Acknowledgements

Due to the fact that I spent both my undergraduate and graduate careers at Caltech, I have a great many people to thank for their support of my thesis work. I would like to begin with a special thank you to Barclay Kamb, who first piqued my interest in Caltech when I was a visiting high school senior by telling me I could go to Antarctica if I came here as an undergrad. I spent many hours in Barclay's lab doing glacial research and the three months I spent in Antarctica as his field assistant were some of the best weeks of my life. I also thank Brian Wernicke, Joe Kirschvink and Jason Saleeby for supervising various research projects that expanded the breadth of my scientific experience. Mark Simons first began advising me during my senior year when he handed me a programming book and suggested that if I ever needed to do anything twice, I should write a script for it. Since then, he has proved to be a wonderful resource for topics ranging from inverse theory to tectonics, and a critical sounding board for ideas that came up during my thesis work. He and Martha House have opened their home to me on numerous occasions and I greatly value their hospitality and friendship.

My work at Caltech was supported by many diverse agencies and individuals that I would like to briefly name here. The family of Joseph E. Terraciano provided a significant percentage of my undergraduate tuition and encouraged me to speak publicly about my work to non-scientists. My graduate study was supported in part by the Caltech Henshaw and National Science Foundation graduate fellowships. The data presented in this thesis was acquired as part of a Category 1 research project from the European Space Agency, and through funding from URS Corporation in association with Chandan Saikia. Paul Rosen has facilitated many years of interaction

with people at the Jet Propulsion Laboratory (JPL) and has helped me greatly in my understanding of InSAR through courses and conversations. I benefited greatly from discussions with Yuri Fialko, Luis Rivera, and Tapio Schneider about InSAR and inverse theory. Chapters 2 and 4 include modifications based on the helpful feedback from several anonymous reviewers. I thank Kimo Yap and Mike Black for their efforts to make the the computational framework that we all rely on blend as seamlessly into the background as possible. Rosemary Miller has overseen the logistics of many data orders and shipments over the years. Additional thanks go to my thesis committee for their support and constructive comments.

During the early years of my academic life, my background was repeatedly enriched by my inclusion in scientific classes and research outside of Caltech. I especially thank Maynard Miller, who accepted me into the Juneau Icefield Research Program (JIRP) when I was in high school. That opportunity opened many doors for me in the years to follow, and solidified my basic interest in the earth sciences. My undergraduate summers were enriched by research activities as part of the University of Alaska, Fairbanks, undergraduate research program at the Alaska SAR facility, the Summer of Applied Geophysical Experience (SAGE) and the Summer Undergraduate Research Fellowships (SURF) at Caltech, which was my first introduction to InSAR. I thank Jason Saleeby and Mike Scott for the wonderful opportunity to take a field trip through Southeastern Alaska studying accreted terranes. My parents have always provided me with stimulating environments and outlets for my creativity, including years of car shuttling every afternoon to swim practices and music lessons. I especially thank them for the the week-long camping trips we took every year through the Western U.S, introducing me to the landscapes I would later study.

There are many Caltech students who shared my experiences through the various stages of my academic career. I want to thank Greg Okin, Nathan Niemi, Magali Billen, Anthony Toigo, Emily Brodsky, Francis Nimmo, Sarah Stewart-Mukhopadhyay, Sujoy Mukhopadhyay, and Mark Roulston for their camaraderie on field trips, in classes and through all the other aspects of my life. Many of them acted as advisors and confidants during my undergraduate days and I feel very fortunate that we

have developed lasting friendships that persist despite the distances that now divide us. I also want to thank the roommates I've had during my graduate study: Adam Burgasser, Nathan Downey, Nicole Smith and Emily Schaller, who've provided me with cat sitters, great cooking and relaxing political conversation in the evenings after work. I am indebted to Brent Kious for support during my oral examination and the early years of my graduate student career. All of the members of our reading and knitting groups allowed me to exercise those parts of my brain that were neglected during my thesis work. I thank Chris DiCaprio, Brian Savage, Ryan Petterson and Alisa Miller for helping me realize my dream of a field trip to Afton Canyon. Jennifer Yu, Patricia Persaud, Jean-Luc Margot, Jane Dmochowski, Joe Akins, Viola Carter, Nadine McQuarrie and Marin Clark have all variously shared in stimulating discussions about scientific research, academic life and the world beyond the ivory tower. Matthew Pritchard has always nurtured my curiosity and supported me in every endeavor I approach.

Abstract

The spatial and temporal coverage of geodetic data sets such as Interferometric Synthetic Aperture Radar (InSAR) and Global Positioning System (GPS) is increasing to the point where we can constrain many aspects of the deformation associated with earthquakes and volcanic eruptions. As our understanding of the kinematics of deformation improves, we can begin to explore the dynamic processes that drive seismic and volcanic deformation in tectonically active regions around the world.

In this thesis, I use InSAR data in inversions for earthquake source parameters for both small ($4.0 < M_w < 5.5$) and large ($M_w > 7$) earthquakes. For small earthquakes, I focus on constraining the hypocenter location and seismic moment. I examine data for small earthquakes in the Basin and Range province of the Western United States, and in the Zagros mountains of Southern Iran. For large earthquakes, I place constraints on the coseismic slip distribution for a pre-determined fault plane geometry and explore how sensitive the inversion is to inadequacies in the fault plane parameterization. I perform inversions for both the 1999 M_w 7.1 Hector Mine earthquake in Southern California and the 1995 M_w 8.1 Antofagasta earthquake in Chile.

I also describe some advances in the technical details of using InSAR observations in inversions for deformation source parameters. I use the full noise covariance matrix in my inversions and compare inferred noise covariances for several interferograms covering the Mojave desert, Southern California, with GPS observations of tropospheric structure functions. I provide an algorithm for resampling (or averaging) InSAR data to minimize the computational burden by reducing the number of data points used as input to inversions. I also explore techniques for regularizing poorly determined inversions of geodetic data for coseismic fault slip.

Contents

List of Figures

List of Tables

Overview

0.1 Introduction

Over the last few decades, space agencies around the world acquired a catalog of Interferometric Synthetic Aperture Radar (InSAR) data covering much of the Earth's surface with a varying number of observations in time. Networks of continuous Global Positioning System (GPS) receivers in tectonically active regions provide temporal coverage of the full seismic cycle, while InSAR and pixel tracking using various types of remote sensing imagery (e.g., Landsat, Aster, SAR, air photos) can provide spatially dense observations of deformation over regions several 100 km^2 in extent.

This unprecedented set of geodetic data allows both direct observation of processes such as secular deformation, aseismic fault slip transients or volcanic deformation rate changes, and the inference of deformation source properties such as distributions of coseismic fault slip and earthquake or magma chamber locations. As the quantity and quality of kinematic models grow, we can begin to examine the dynamics of deforming systems, including placing constraints on fault zone friction laws and earthquake triggering processes, and understanding the relationship between the spatial distribution of short term processes such as coseismic fault slip in subduction zone earthquakes and longer time-scale characteristics of the system such as gravitational or topographic anomalies (e.g., *Song and Simons*, 2003; *Wells et al.*, 2003).

I examine ways of best using the rich geodetic datasets to understand localized deformation sources, with specific application to deformation associated with earthquakes. I begin with methods for describing and accounting for the structure of atmospheric noise in interferograms, and with a data resampling technique that re-

duces the number of data points used as input to our inversions without significantly degrading the information content.

The main body of my thesis is concerned with earthquakes at opposite ends of the earthquake magnitude scale. Small earthquakes (M_w 4.5-6) can delineate active structures in remote areas where we have little other information about the processes accommodating plate tectonic motions. The distribution of small earthquakes also helps us understand the style of deformation and the depth range within which deformation is accommodated seismically. In addition, the eventual creation of a catalog of precise, geodetically-determined hypocenters will aid in resolving the tradeoff between location and velocity structure that frequently plagues seismic tomography. I locate several small earthquakes in the western U.S. and in the Zagros Mountains of Southern Iran and comment on the implications of their distribution on the regional tectonics.

Large earthquakes ($M_w > 7$) create a step function of stress in time along the fault, which the crust then responds to by a variety of postseismic processes. In order to interpret the observed postseismic deformation, we must have a full understanding of the coseismic slip distribution, including how the uncertainties in fault plane location, rheology of the crust, and observational errors map into uncertainties on the inferred slip distribution. There have been many inversions of geodetic data for coseismic fault slip over the past few decades (e.g., *Segall and Harris*, 1987; *Ward and Valensie*, 1989; *Barrientos and Ward*, 1990; *Freymueller et al.*, 1994; *Pritchard et al.*, 2002; *Simons et al.*, 2002), employing a wide range of regularization techniques. I present a semi-automatic technique for regularizing inversions for subsurface fault slip from observations of surface deformation. I use several synthetic scenarios to illustrate the sensitivity of fault slip inversions to data noise, errors in fault geometry, and data distribution. I present results for the Southern California 1999 Hector Mine earthquake, illustrating how my regularization technique runs into difficulties when the fault plane geometry is poorly determined. This problem is magnified for strike-slip earthquakes where data points can be very close to the fault plane and errors in geometry become more significant. I also apply my technique to the M_w

8.1 Antofagasta subduction zone earthquake that occurred in Chile in 1995. In the subduction zone setting the fault plane is much further from the data observations, so that the inversion is less sensitive to fault plane geometry errors than in the Hector Mine earthquake inversion.

0.2 Thesis outline

This thesis is divided between InSAR data analysis techniques and applications of these techniques to inversions for earthquake source parameters. In Chapter 1, I address two aspects of the treatment of InSAR data in inversions for earthquake parameters. I develop methods for describing the spatial covariance of InSAR noise and incorporating this covariance into inversions. InSAR provides spatially dense measurements over length scales of 100s of km, potentially resulting in tens of millions of data points. I demonstrate a method for greatly improving computational efficiency by reducing the number of data points used as input to inversions without losing significant information.

In Chapters 2-3, I examine nonlinear inversions of geodetic observations for earthquake locations and mechanisms. Chapter 2 describes my inversion technique, applies this technique to the Little Skull Mountain earthquake, and compares inversions of InSAR data alone with joint inversions of seismic, GPS and InSAR data. I comment on the implications of the inferred earthquake location on the stability of the region around Yucca Mountain, a proposed hazardous waste repository site.

In Chapter 3, I show the results of a survey of surface deformation associated with mid-sized earthquakes in Southern Iran. The Zagros mountains of southern Iran are the result of the ongoing collision between Arabia and Eurasia. Due to the poor seismic station coverage in this region, earthquake locations for smaller events ($M_w < 5.5$) often have errors of up to 50 km in map view and depth. I performed a search through the existing InSAR catalog and examined all earthquakes with magnitudes $M_w > 4.5$ spanned by interferometric pairs with spatial baselines ($B_\perp$) less than 150 m and time periods less than 3-4 years. 5 events have detectable ground

deformation significantly above the level of the noise, and/or that is visible in more than one independent interferogram. I describe each deformation source and comment on the significance of their locations in the regional tectonic framework of the Zagros mountains.

Chapters 4-5 deal with inversions for the best-fitting coseismic slip distributions due to large ($M_w > 7$) earthquakes. The focus here on larger events stems merely from the fact that the earthquakes in question produce surface deformation with a rich structure that requires we move beyond fitting the data with a single fault patch or point source. A small, but very shallow, earthquake may require the same treatment, whereas a large, but very deep earthquake may be sufficiently fit by a point source. In Chapter 4, I describe the ${}_j\mathcal{R}_i$ method and variable smoothing, two improvements on earlier techniques for regularizing this style of inverse problem. In Chapter 5, I apply the ${}_j\mathcal{R}_i$ method and other techniques discussed above to the 1995 M_w 8.1 Antofagasta subduction zone earthquake in Chile and to the 1999 M_w 7.2 Hector Mine earthquake in Southern California. I discuss the inversion results for each event and comment on how the different types of model-data geometry affect the inversion. I end this thesis with a discription of the future directions of this work.

Chapter 1

Some thoughts on the treatment of InSAR data

Abstract

Repeat-pass Interferometric Synthetic Aperture Radar (InSAR) provides spatially dense maps of surface deformation with potentially millions of data points. Typically, any covariance of the noise between individual InSAR data points is neglected and each data point is assumed to be independent. Here, we examine this assumption by estimating the actual covariance structure of noise in InSAR data. We compare the results for several independent interferograms with a large ensemble of GPS observations of tropospheric delay and discuss how the processing of InSAR data affects the inferred covariance structure. Motivated by computational concerns associated with numerical modeling of deformation sources, we then combine the data-covariance information with the inherent resolution of an assumed source model to develop an efficient algorithm for spatially variable data resampling (or averaging). We illustrate these technical developments with two earthquake scenarios at different ends of the earthquake magnitude spectrum. For the larger events, our goal is to invert for the coseismic fault slip distribution. For smaller events, we infer the hypocenter location and moment, with the mechanism constrained by seismic data. We compare the results of inversions using several different resampling algorithms, and we assess the importance of using the full noise covariance matrix, including the magnitude of errors introduced when data containing correlated noise is inverted under the assumption of uncorrelated noise.

1.1 Introduction

The continually improving spatial and temporal coverage of geodetic data sets such as those provided by Interferometric Synthetic Aperture Radar (InSAR) motivates us to better quantify the sources of error in these datasets in order to rigorously characterize how well we can resolve the evolution of deformation sources in space and time. Typical deformation sources include magma chambers, dike intrusions, and slipping faults. The large volume of available observations presents us with a number of challenges, including the characterization and treatment of data noise and practical considerations of how to minimize the computational cost of examining such large datasets. In this paper we explore these two aspects of the treatment of InSAR data with applications to inversions for subsurface fault slip and earthquake location.

First, we present a technique for estimating the covariance structure of noise in InSAR data. To properly combine InSAR and Global Positioning System (GPS) data, and to assess the uncertainties on inferred model parameters, we require an understanding of the character of InSAR data noise. We compare results derived from an ensemble of interferograms with the noise covariance structure derived from GPS data from Southern California (*Emardson et al.*, 2003). Second, driven by a desire to minimize the computational burden involved in our studies, we demonstrate how we reduce the number of data points used as input to our inversions. Whereas researchers working with earlier, sparser datasets needed to use all the available observations in order to extract as much information as possible about the system of interest (e.g., *Harris and Segall*, 1987; *Segall and Harris*, 1987), we now have the luxury of acquiring nearly spatially continuous measurements of ground deformation. Practical considerations, such as the frequent need to perform Monte Carlo tests requiring the calculation of a large number of forward models, lead us to develop methods of spatial sampling and averaging of interferograms in a manner that reduces the number of data points while retaining as much information as possible (e.g., *Jónsson et al.*, 2002; *Simons et al.*, 2002).

We end with demonstrations of the application of these techniques on two earth-

quakes where the goals of our inversions are quite different. For large earthquakes (>M_w 7) we typically perform linear inversions for the distribution of coseismic fault slip on a plane fixed by the mapped surface trace and aftershock distributions. We use the correct covariance matrices for the noise estimated directly from the data, and illustrate how our resampling algorithm performs compared with previous resampling techniques. For smaller events (<M_w 6), our goal is often simply to constrain the location of the fault plane, earthquake mechanism and moment. We perform nonlinear inversions for the best-fitting fault plane geometry, using the Neighborhood Algorithm (*Sambridge*, 1998a; *Lohman et al.*, 2002, Chapter 2, this thesis). We demonstrate how neglecting the off-diagonal components of the noise covariance matrix affects the error bounds that we place on our hypocenter estimate.

1.2 Effect of correlated noise

InSAR and GPS data both contain spatially correlated noise (e.g., InSAR data in Figure 1.1). This correlation is primarily due to atmospheric and ionospheric structures that are commonly correlated over length scales of 10s to 100s of km. Variations in atmospheric water vapor with elevation can also introduce errors in the measurement of satellite line-of-sight (LOS) that are correlated with topography (e.g., *Goldstein*, 1995; *Zebker et al.*, 1997; *Williams et al.*, 1998; *Hanssen*, 2001; *Jónsson*, 2002; *Emardson et al.*, 2003). In order to assess the significance of features of an inferred source model, we must estimate confidence intervals and model parameter covariances. The degree to which the data noise is correlated affects both these quantities (e.g., *Menke*, 1989).

To estimate the noise covariance matrix, C_n, for individual interferometric pairs, we assume that the noise is spatially stationary and isotropic, or that the covariance between any two points depends only on the distance between them. We define the

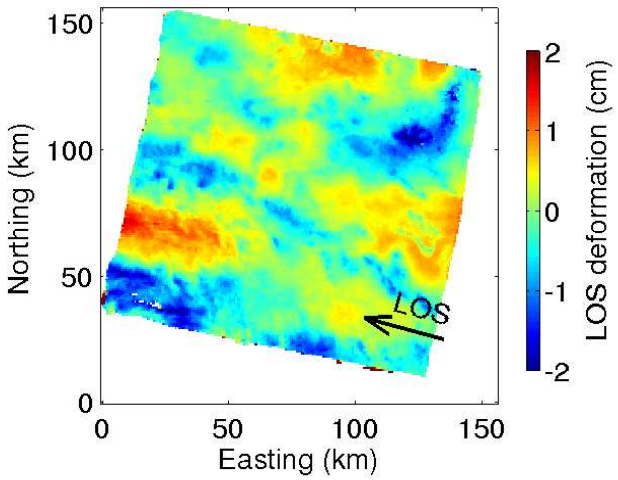

Figure 1.1: Sample interferogram from the Mojave desert in Southern California, illustrating the spatial covariance of atmospheric noise. Interferogram covers Track 127, Frame 2925, spanning 1995/10/10 to 1995/12/19, with perpendicular baseline $(B_\perp) = 37$ m. Arrow indicates the horizontal projection of the LOS vector.

covariance between two points separated by a scalar distance, r, as:

$$\begin{aligned} C(r) &= Cov(\mathbf{x}, \mathbf{x}+\mathbf{r}) \\ &= E[f(\mathbf{x})f(\mathbf{x}+\mathbf{r})] \end{aligned} \tag{1.1}$$

where $r = |\mathbf{r}|$, $f(\mathbf{x})$ is the atmospheric noise at position $\mathbf{x}$ within the interferogram and where we assume that the average value of the noise is zero. We also consider the structure function, which is typically defined (e.g., *Williams et al.*, 1998; *Hanssen*, 2001; *Jónsson*, 2002) as the variance of the difference between two points separated by a distance r:

$$S(r) = E[(f(\mathbf{x}) - f(\mathbf{x}+\mathbf{r}))^2] \tag{1.2}$$

so that

$$C(r) = \sigma^2 - S(r)/2 \tag{1.3}$$

where σ^2 is the variance of noise within the image. Our assumption of stationary,

isotropic noise implies that both C and S are functions only of the scalar distance r.

We examine two methods of calculating C and S for a given interferogram. First, we explicitly compare all pairs of points within the interferogram, Φ, by calculating the full autocorrelation matrix, $\mathbf{A}$. The average of $\mathbf{A}$ vs. distance is equivalent to $C(r)$.

$$\mathbf{A}_{dx,dy} = \frac{1}{ng} \sum_{i=dx}^{nx} \sum_{j=dy}^{ny} \Phi_{i,j} \Phi_{i-dx+1,j-dy+1}, \;\; dx = 1 : nx, \;\; dy = 1 : ny \tag{1.4}$$

where nx and ny are the number of columns and rows in the interferogram and ng is the number of valid values within the overlapping region at each shift (dx, dy). We keep track of the difference between each pair of points to form $\mathbf{S}$:

$$\mathbf{S}_{dx,dy} = \frac{1}{ng} \sum_{i=dx}^{nx} \sum_{j=dy}^{ny} \left(\Phi_{i,j} - \Phi_{i-dx+1,j-dy+1}\right)^2 \tag{1.5}$$

In Figure 1.2 we show the radial averages of $\mathbf{A}$ and $\mathbf{S}$ ($C(r)$and $S(r)$, red curves). Neither average is sensitive to anisotropy in the atmospheric noise.

Our second technique for computing C and S is a sample variogram, where we choose a large number of random pixel pairs within the interferogram, binned by distance (blue curve in Figure 1.2). For the example shown in Figures 1.1 and 1.2 we use an interferogram that has been subsampled down to less than a hundredth of its original size (i.e., in radar processing parlance, the interferogram has been looked down 10 times in range and 50 times in azimuth). For larger images, computation of the autocorrelation and structure function using all possible pairs of points within the image becomes computationally prohibitive. Figure 1.2 indicates that it is sufficient to use a sample variogram instead, as long as the number of random pairs of points is sufficiently large.

Both theoretical work on atmospheric turbulence (e.g., *Tatarski*, 1961), GPS observations of tropospheric delay (e.g., *Emardson et al.*, 2003) and previous studies of InSAR data (e.g., *Goldstein*, 1995; *Zebker et al.*, 1997; *Hanssen*, 2001; *Jónsson*, 2002) indicate that the spatial structure of the atmosphere exhibits power-law behavior that is correlated over length scales of several 100s of km. However, we wish to note some

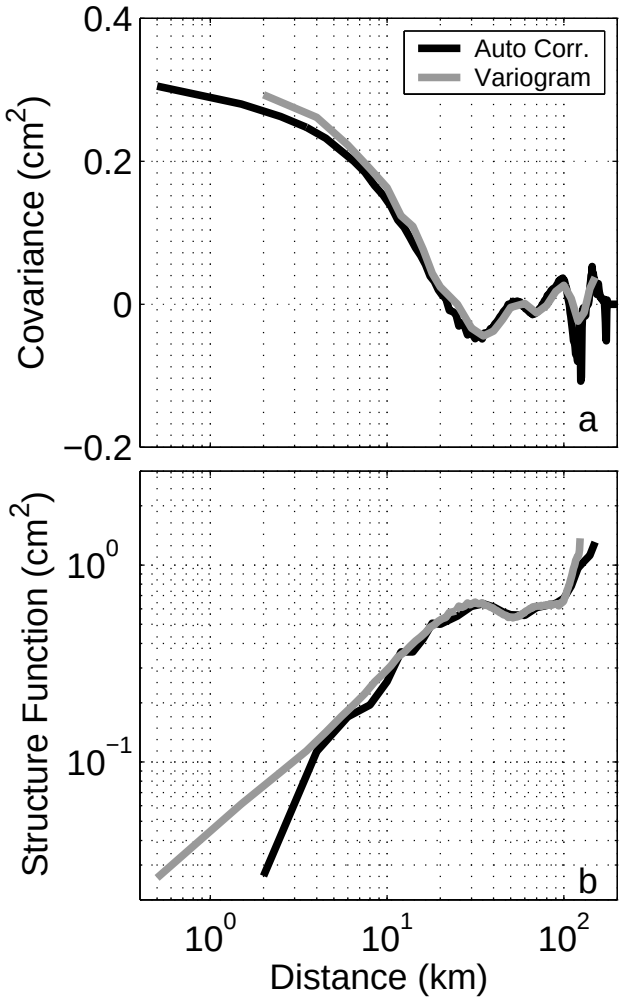

Figure 1.2: Covariance and structure function vs. distance for the interferogram in Figure 1.1. a) Covariance, $C(r)$, determined from autocorrelation matrix (black) and by variogram (gray). b) Structure function, $S(r)$, determined using all pairs of points (black) and from variogram (gray). Note that for most distances the variogram agrees with the result from the full dataset.

differences between the character of noise observed in InSAR data and that observed in GPS time series. First, interferograms are sensitive to the difference between atmospheric delays at two discrete times, so that we observe the covariance in space rather than in time. Second, the limited spatial scale of the interferogram, the fact that we observe phase delays relative to some arbitrary constant, and the fact that orbital errors introduce an uncertainty approximately corresponding to a quadratic ramp across the image, all mean that the covariance we observe within the interferogram is different than the actual covariance between points across that particular time interval. Many of the interferograms examined in this thesis have empirical C_d that have a logarithmic decay over some scale length L_c (i.e., Figure 1.2).

The covariance we infer for any particular set of noise depends in part on the spatial extent of the dataset. We explore the difference between inferred and actual covariances with several synthetic tests. We create synthetic correlated noise, n_c, from a pre-determined covariance matrix, C_d, using the following relation:

$$n_c = v d^{1/2} n_n \tag{1.6}$$

where n_n is uncorrelated noise and v and d are the matrices of eigenvectors and eigenvalues of C_d, respectively. Not surprisingly, we find that the variance we estimate for subsets of pixels within synthetically generated correlated noise only approaches the input variance when the window size is several times larger than the correlation length scale of the noise (Figure 1.3). Furthermore, the covariance we infer from data with power-law correlated noise changes when we begin by removing the mean or a quadratic ramp from the data (Figure 1.4). When we remove a quadratic ramp over an image approximately 100 km in extent, the remaining signal is only correlated on length scales of around 50 km. The removal of the mean of the signal corresponds to the case where we believe we have good information on the orbital baselines and are confident that our interferogram characterizes the noise to within an arbitrary constant. Note that the blue and black lines overlay each other in Figure 1.4e, because the structure function is insensitive to the mean value of the noise. In Figure 1.4f, we

show the inferred covariance for the real interferogram from Figure 1.1, both with and without the removal of the best-fitting ramp, analogous to the red and blue curves in Figures 1.4d and 1.4e.

We compare inferred noise covariances for several individual interferograms in the region surrounding the 1999 M_w Hector Mine (CA) earthquake with previous work based on simulating expected InSAR covariances by using a large ensemble of GPS observations of tropospheric delay in Southern California (*Emardson et al.*, 2003). In Figure 1.5a, we show the inferred spatial structure function for interferograms spanning different time intervals over the same location. Interferograms spanning the time of the Hector Mine earthquake are shown in black, and those using interseismic interferograms are shown in gray. When the interferogram spans the earthquake, we remove a model of the coseismic deformation before we examine the noise structure. The similarity in the spatial scale of the noise between coseismic and interseismic interferograms ($\sim$ 10 km) indicates that our estimate of the noise structure is insensitive to our method for removing the coseismic signal. In our inversions, we fit a spline to the function of covariance vs. distance (Figure 1.5b, Section 1.4).

The disagreement in functional form between our observations and the GPS data at distances greater than 10^2 km results from the fact that we perform a series of filtering operations on the InSAR data during the formation of the interferogram, including the absorption of a quadratic ramp by an interferometric baseline reestimation procedure. The dashed curves indicate the structure function we would infer if we did not remove a ramp from the final interferogram. One benefit of empirical covariance and structure functions compared with theoretical calculations of noise structure is that we include the effect of the filtering, averaging, variations of atmospheric H_2O, and DEM errors that are part of the interferogram processing.

1.3 Resolution-based resampling

Inversion of interferograms at full resolution can require evaluating the forward problem at over 10^7 points, which is computationally expensive. This expense is magnified

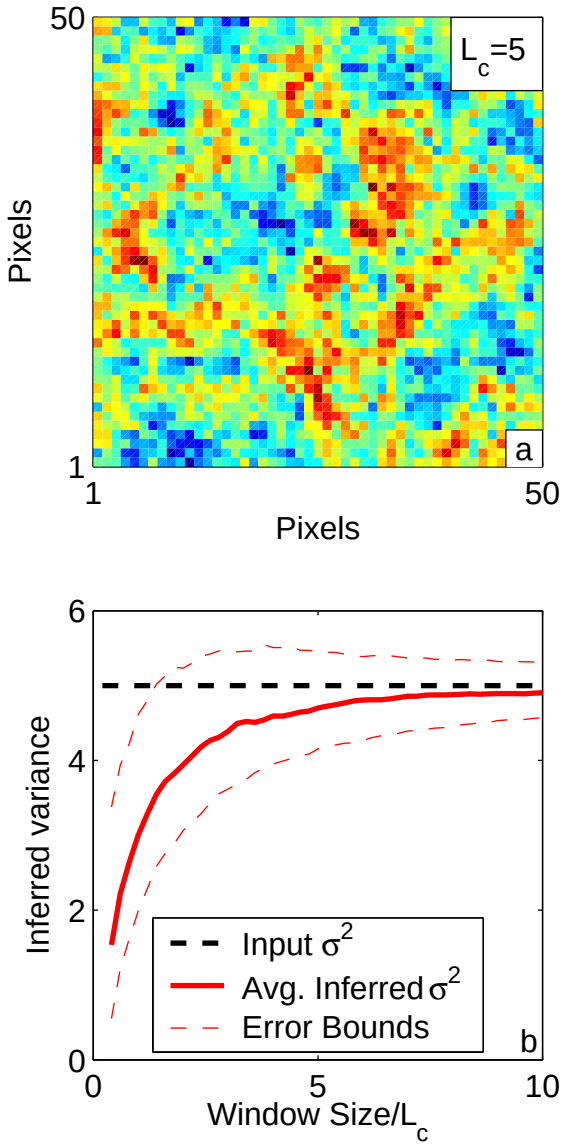

Figure 1.3: Dependence of inferred variance on window size: a) Synthetic noise with covariance following logarithmic decay with scale length, $L_c = 5$ pixels. b) Inferred variance of pixels vs. window size. Note that the inferred variance approaches the input variance when the scale length of the noise is several times smaller than the window size.

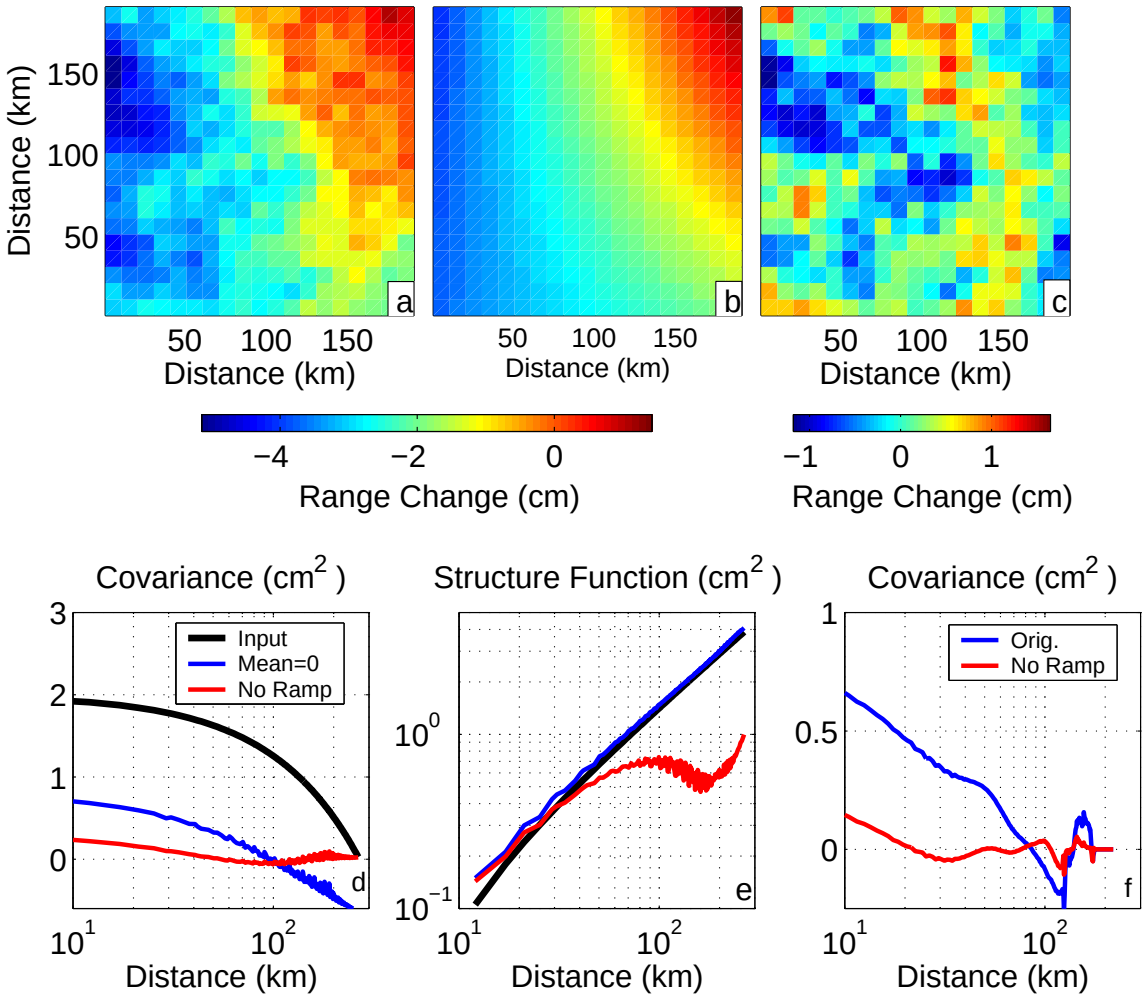

Figure 1.4: Effect of ramp removal on character of noise: a) One realization of noise with power law structure function. b) Best-fit quadratic ramp to (a). c) Remaining signal after ramp removal. d) Input covariance (Heavy line) and inferred covariance for synthetic noise in (a) after removal of mean (blue) and quadratic ramp (red). e) Structure function for same scenario. f) Covariance inferred for real data in Figure 1.1, with and without the removal of the best-fitting quadratic ramp.

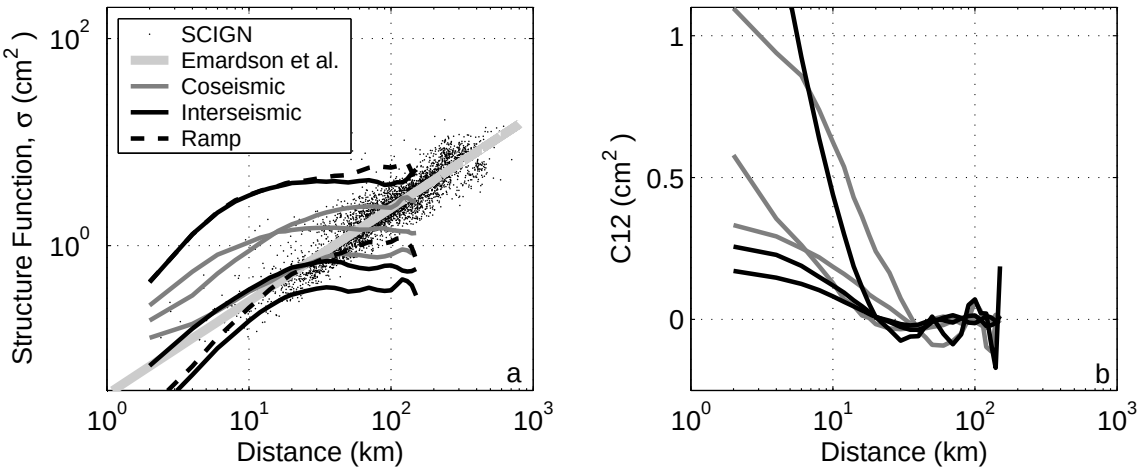

Figure 1.5: a) Spatial structure function vs. distance for each of the 3 interferograms spanning the Hector Mine event (black), and three interferograms spanning time periods before or after the earthquake (gray). Dashed lines indicate the structure function for the interferogram before a quadratic ramp was removed. GPS data (small dots) are from the Southern California Integrated GPS Network (SCIGN) (adapted from *Emardson et al.*, 2003). The thick grey line indicates the functional form used in *Emardson et al.* (2003). b) Covariance vs. distance for the coseismic and interseismic interferograms from (a).

for nonlinear problems where we adopt Monte Carlo optimization techniques. We can reduce the number of data points without losing significant information by taking appropriate spatial averages. These averages take advantage of the fact that individual neighboring pixels far from the deformation source contribute approximately the same information to the inversion. We define a set of n orthogonal boxcar functions, a_i, such that:

$$\sum_x a_i(x)a_j(x) = 0 \tag{1.7}$$

$$D_i = \sum_x a_i(x)d(x) \tag{1.8}$$

where x is a spatial coordinate covering the interferogram, d are the original, full resolution data, and D are the resulting resampled data points. We retain our earlier assumption of spatially stationary and isotropic noise, or we would need to include a covariance term in Equation 1.8. For linear problems, we infer a slip model, m, from a given D using the relation:

$$Gm = D \tag{1.9}$$

where G is the design matrix of Green's functions. The goal of any resampling algorithm is to reduce the size of G and D, which control the number of computationally expensive forward models that we have to compute, without reducing the information about m contained in the inversion. The character of G controls the shape of the optimal distribution of D.

Previous techniques for resampling InSAR data include uniform sampling, in which the a_i form a regular grid across the image (e.g., *Pritchard et al.*, 2002), and resampling techniques based on the spatial complexity of d. Examples of the latter approach include the Variable-Resolution (*Simons et al.*, 2002) and Quadtree (e.g., *Jónsson et al.*, 2002) algorithms which both sample the data according to its spatial variance. Both methods begin by dividing the data into quadrants and subdividing each quadrant until the variance within each smaller quadrant is below a preset threshold. The two techniques differ in the function removed from each sub-quadrant before estimating the variance. The Quadtree algorithm removes the local mean, and the Variable-Resolution algorithm removes the best-fitting local bilinear ramp. Variable-Resolution is sensitive only to the curvature of the signal, whereas the sampling density of the Quadtree algorithm also depends on the local slope, and therefore the absolute amplitude, of the deformation field.

Uniform sampling is not ideal for deformation sources which approach or break the surface because to achieve dense sampling near the source where the data has the most detailed structure, you may be required to include an unnecessarily large number of data points in the inversion. For subduction zone events or other deep sources of deformation (e.g., *Pritchard et al.*, 2002), uniform sampling is a reasonable approach, although the issue of data covariance must not be neglected when the sampling rate is smaller than L_c, the correlation length of the noise. In the presence of small-scale perturbations to the data from noise, decorrelation or phase-unwrapping errors, both the Variable-Resolution and Quadtree algorithms may produce high densities of data far from the deformation source.

We introduce an algorithm that uses the design of the inverse problem to determine the optimal data sampling density. We examine the data resolution matrix for a

given set of a_i, beginning with a coarse uniform sampling. If any particular a_i is resolved above a prescribed threshold, we partition it into four smaller regions and re-examine the new data resolution. Our data resolution-based (R-based) specific sampling algorithm is as follows:

1. Define the source parameterization (e.g., fault plane geometry)
2. Begin with a coarse grid of a_i and form D_i
3. Compute Green's functions
4. Form generalized inverse, $G^{-g} = (GG')^{-1}G'$ (e.g., *Menke*, 1989)
5. Calculate data resolution matrix, $N = GG^{-g}$
6. Find all D_i where the diagonal of N is above preset threshold
7. Subdivide points from (6) into 4 parts, forming new a_i
8. Repeat (3-7) until all D_i are just below threshold

where G is the matrix of Green's functions augmented by a weighted finite difference approximation of the Laplacian smoothing matrix (e.g., *Menke*, 1989). Our two tuning parameters are the resolution threshold (between 0 and 1) and the weighting of smoothing included in G. For a reasonably small size of fault patch, we must apply some smoothing to avoid numerical difficulties in the inversion. If the resolution threshold is close to zero or if the smoothing is small then the final number of D_i, n, will be higher. Currently, the choice of tuning parameters is somewhat arbitrary and is driven simply by the desire to have a low number of points (so that the computational cost is reasonable) that are concentrated near the fault. In our implementation, we also remove samples corresponding to regions that cross the fault. The number of data points in each box does not simply scale with box size, since some boxes contain decorrelated regions. We illustrate how the sampling evolves over several steps using data for the Hector Mine interferogram that we will examine in Section 1.4 (Figure 1.6).

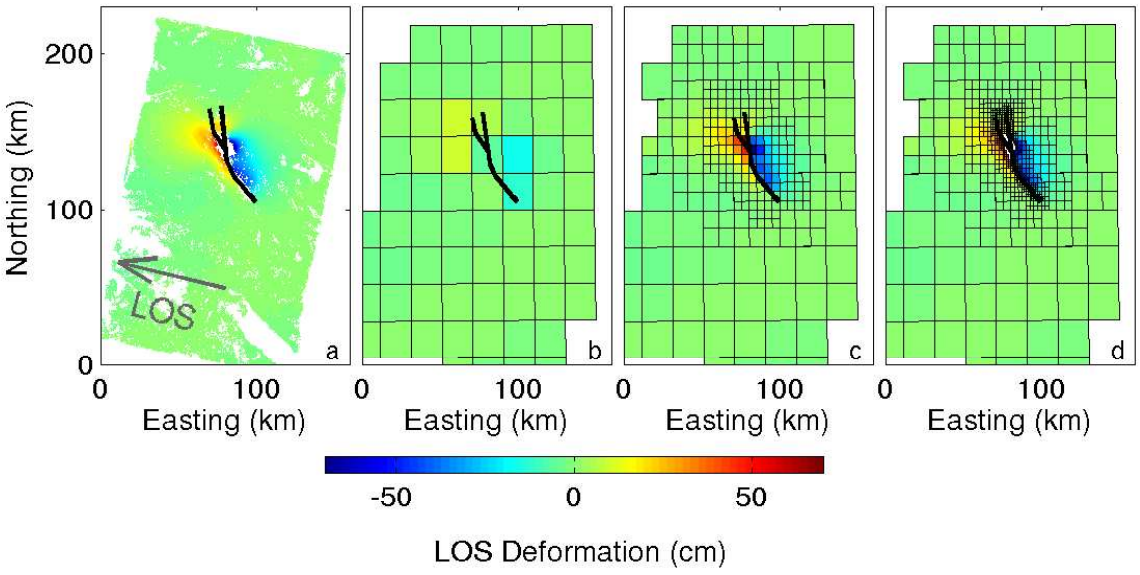

Figure 1.6: a) Input unwrapped interferogram for Hector Mine earthquake: Track 127, Frame 2907, spanning 1999/01/13 to 1999/10/20. Color indicates the line-of-sight (LOS) change towards or away from the satellite in the direction indicated by the grey arrow. Black lines indicate the fault plane. (b-d) Iterations 1, 3 and 6 of the R-based resampling algorithm. Color indicates the average LOS value for all non-NAN points contained within each box.

Our inversion would not be complete without a data covariance matrix associated with our resampled D_i. Recognizing that each D_i is a sum over a subset of d's, we express the covariance between any D_i and D_j as:

$$Cov(D_i, D_j) = Cov(\frac{1}{n_i} \sum_{x=a_i} d(x), \frac{1}{n_j} \sum_{x=a_j} d(x)) \tag{1.10}$$

or

$$Cov(D_i, D_j) = \frac{1}{n_i n_j} \sum_{x_i=a_i} \sum_{x_j=a_j} Cov(d(x_i)d(x_j)) \tag{1.11}$$

The covariance between any two D_i is the sum of the covariance between all points included in their averages, as determined in Section 1.2. Likewise, the variance of any individual D_i accounts for all the data points averaged by a_i.

When we perform an inversion of geodetic data (InSAR or GPS), we transform our system of equations by premultiplying with $P = Q^{-1}$, where Q is the Cholesky factorization of C_d such that $QQ^T = C_d$. If we use the correct C_d, this transform

results in reweighted data with unit variance (e.g., *Harris and Segall*, 1987; *Segall and Harris*, 1987).

1.4 Example 1: A large shallow strike-slip earthquake

We demonstrate the behavior of our resampling algorithm on inversions for subsurface fault slip using synthetic data similar to the InSAR data spanning the 1999 Hector Mine Earthquake (M_w 7.1). We consider only synthetic scenarios because we can separate out the effects of noise and data distribution from model errors in fault plane geometry and elastic models of the crust. We use the fault plane geometry described in *Simons et al.* (2002), and determine the noise structure as described in Section 1.2.

To make our synthetic examples similar to a real-world scenario, we generate synthetic data using an input slip model loosely based on one inferred from the real InSAR data (Figure 1.6a). The slip model inferred from real data is already a smoothed representation of the actual slip distribution, so we add Gaussian peaks in slip at several locations on the fault plane to restore a more realistic complexity to the input slip distribution.

To compare our algorithm with the other styles of resampling, we tune each resampling technique so that it produces approximately the same number of data points (Figure 1.7). Because this example is for demonstration purposes, we add a slightly higher level of random noise to several regions around the outside of the interferogram shown in Figure 1.6a to simulate DEM and unwrapping errors. We apply each resampling algorithm to the real data set (3×10^6 data points). We then compute Green's functions for the resulting resampled data geometry and generate synthetic data using the synthetic slip model shown in Figure 1.8. We add noise using the covariance matrix estimated from the interferogram as described in Section 1.2. We then compare the inferred slip model for each set of D. To pick the optimal value of

smoothing in each case, we use the "Jury" technique (Described in Chapter 4).

The uniform algorithm is clearly non-ideal in this example, as is shown by the lower resolution of the slip model in Figure 1.8. The Variable-Resolution and Quadtree algorithms have high concentrations of data near the fault, but there are also clusters of data points associated with the noisy regions on the edges of the interferogram. Even though they use a few more data points, the Variable-Resolution and Quadtree slip models retain fewer of the features in the original slip model than does the R-based slip model.

We note that the R-based algorithm will concentrate sampling around the fault plane even if there is not a large variation in the actual data values associated with a given part of the fault trace. Therefore, we can resolve regions of the fault plane that did not slip during the earthquake, a feature that can be as important as finding the peaks in the slip distribution. The large data gap at the north end of the fault in Figure 1.7b results from the fact that the data-based Variable-Resolution algorithm did not sample the ends of the fault well, so that when we removed all boxes crossing the fault plane, we removed a box that sampled a large area.

1.5 Example 2: A small shallow earthquake

We show how InSAR data can constrain the location of shallow earthquakes to within a few km even when the event is fairly small by teleseismic standards. Precise earthquake locations can be used as input to seismic structural studies, analysis of styles of continental deformation, and can help calibrate earthquake location techniques otherwise based only on seismology. Our ability to locate small, shallow seismicity is an important part of the Comprehensive Nuclear Test Ban Treaty (CTBT) program. Equally important to all of these applications is our ability to place confidence limits on our inferred location for a given event.

We examine a M_w 5.1 reverse-faulting event that occurred in the Zagros mountains of Southern Iran on 1999/04/30 (Figure 1.9). We infer the best-fitting hypocenter, fault plane area and fault slip using the Neighborhood algorithm (*Sambridge*, 1998a).

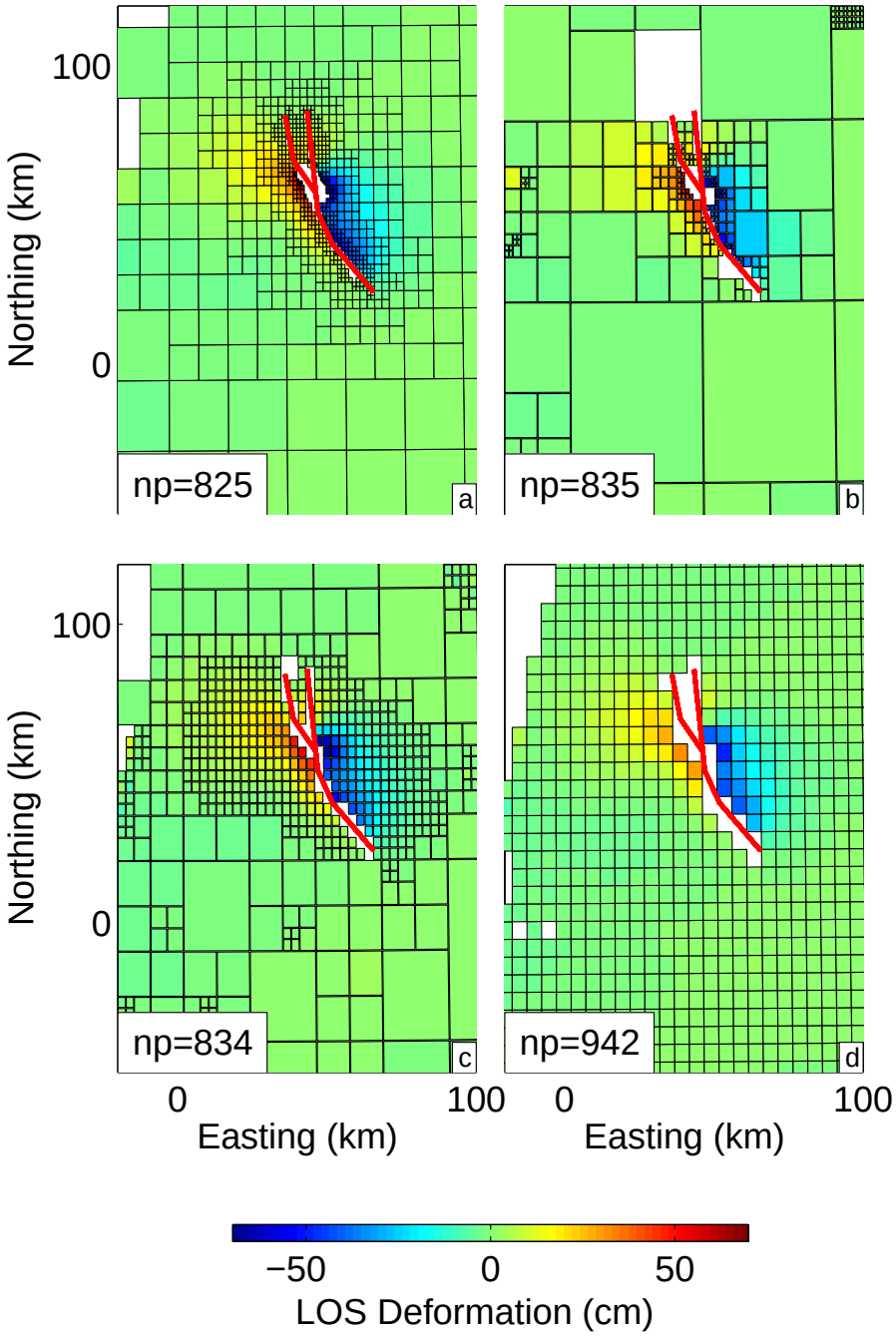

Figure 1.7: Resampling results using each algorithm discussed in the text. a) R-based algorithm b) Variable-Resolution algorithm c) Quadtree d) Uniform sampling.

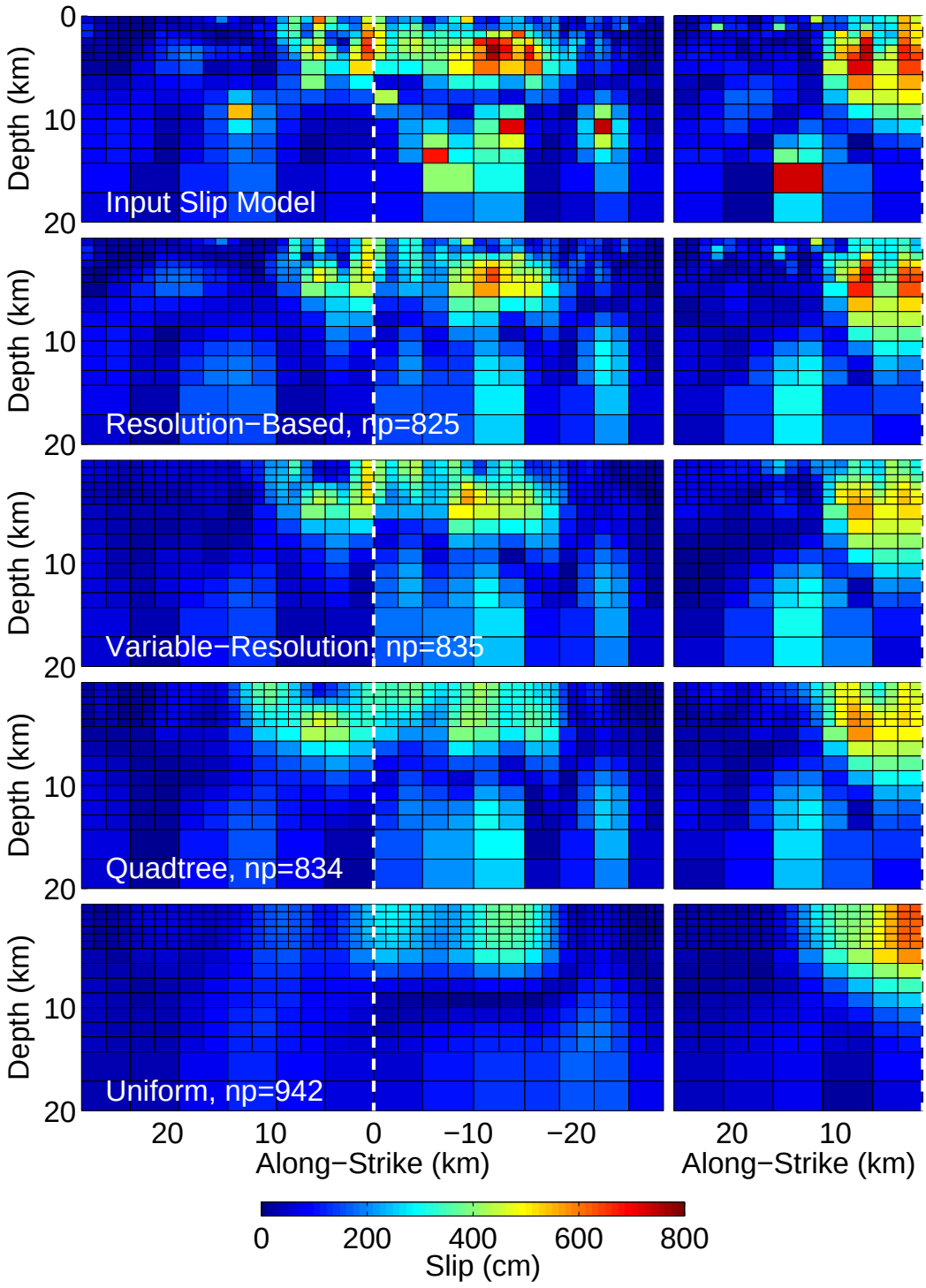

Figure 1.8: Input slip model and comparison of slip models inferred from R-based algorithm, Variable-Res, Quadtree, and uniform sampling. The abscissa corresponds to the horizontal distance from the "Y"-intersection (indicated by dashed white lines) of the Hector Mine fault plane (Figure 1.6), with north in the positive direction. Left and right panels correspond to the eastern and western sides of the "Y", respectively. Note that inferred slip is similar for all inversions, but that R-based resampling better distinguishes between shallow slip features.

The satellite line-of-sight (LOS) of about 23° from vertical results in measurements that are about twice as sensitive to vertical deformation than to horizontal deformation. Since the existing dataset is limited to observations from only one LOS direction, we fix the strike, dip and rake to the values inferred from the International Seismological Center (ISC) and Harvard Centroid Moment Tensor (HCMT) catalogs, which agree with the surrounding structural trends. Our best-fitting location is more than 50 km from the HCMT location, and our hypocenter depth is about 5 km, vastly different from the 45 and 35 km depths in the HCMT and ISC catalogs, respectively. We resampled the full InSAR data set (Figure 1.9a) using an initial guess for the fault plane parameters, then redid the resampling once we performed the NA optimization (Figure 1.9b).

In order to assess what error bounds we should associate with our location, we perform a Monte Carlo sensitivity analysis. We create a large number of independent sets of synthetic noise drawn from the covariance matrix of the noise as estimated from the original interferogram, and add the best-fitting synthetic model from our nonlinear inversion. For each realization of the noise, we invert for the new best-fitting earthquake parameters using the NA algorithm. In Figure 1.10, we show the result of the inversion of each synthetic data set as a small red dot, with 1σ confidence ellipse (red) over the entire distribution of synthetic models. If we only use the diagonal of the covariance matrix, neglecting any spatial correlation of the noise, we get the smaller error bounds indicated in blue. In this case, use of the incorrect covariance matrix would result in overly optimistic error bounds on our best-fitting location. This effect results from the fact that the characteristic length scale of the noise is approximately the same spatial scale (about 10 km) as the deformation signal due to the earthquake.

1.6 Conclusions

By making the assumption that the noise is spatially stationary and isotropic, we ignore the fact that interferograms often contain azimuthally dependent noise due to

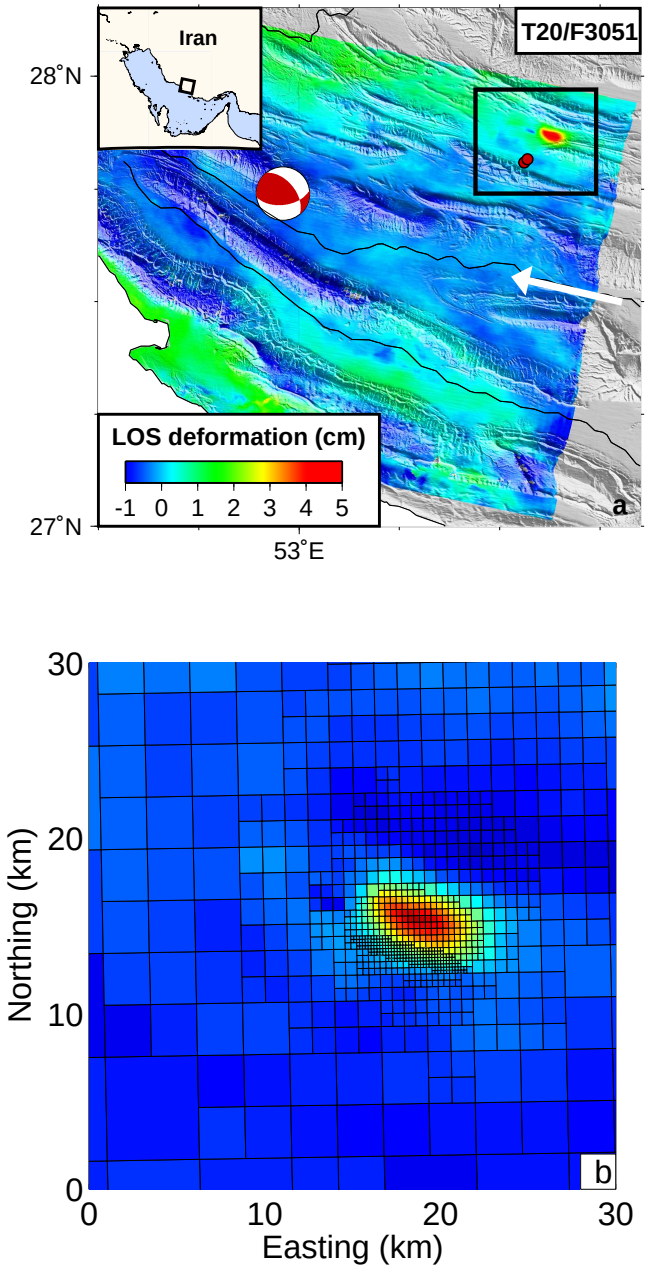

Figure 1.9: a) Interferogram spanning the Apr 30, 1999 M_w 5.1 thrust fault earthquake in the Zagros Mountains of Southern Iran, with HCMT (red mechanism) and ISC (red dot) locations. Inset map shows the location of the InSAR frame. Color indicates LOS deformation in cm, draped over shaded relief topography, with LOS from satellite to ground indicated by white arrow. Black outline indicates location of (b). Note that features of the interferometric noise have a preferred orientation parallel to the structural trend of the Zagros mountains. This azimuthal dependence is not accounted for in our modeling of the noise. b) Resampled data used in inversion.

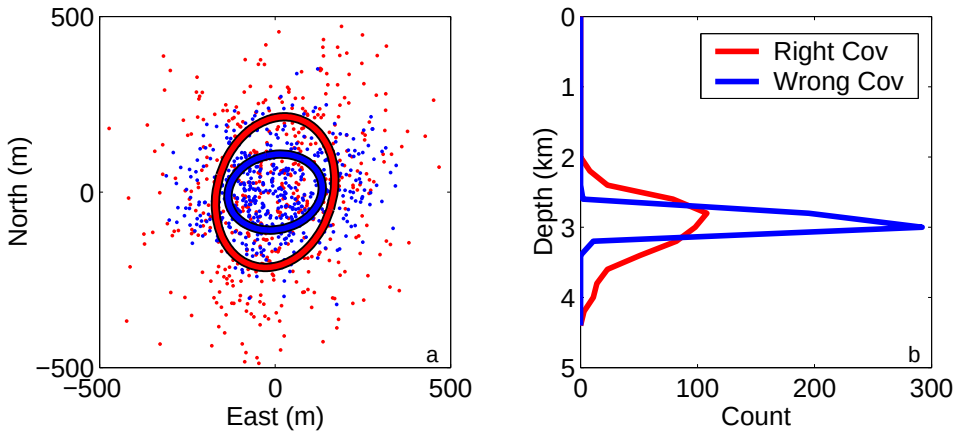

Figure 1.10: Comparison of confidence intervals for correct and incorrect noise covariance matrices, C_n. a) Each dot indicates the inferred map view location for one independent realization of the noise, drawn from either the correct (red) or incorrect (blue) covariance matrix. Solid lines correspond to the 1σ confidence intervals. b) Histogram of inferred depths for each of the 500 Monte Carlo tests. Note how the confidence intervals for each quanitity are much smaller if we use the incorrect covariance matrix.

the correlation between topographic structures and atmospheric water vapor (Figure 1.9a). However, the treatment of noise covariance presented in this paper is an improvement over the neglect of spatial correlation of noise between individual data points. We find that the covariance structure inferred directly from the InSAR data will be different than the actual covariance between data points at a given distance, because of the limited spatial aperture of an InSAR scene and the tradeoff between spatial covariance and satellite orbital errors. We note that a combination of error bounds on the satellite orbits and dense GPS observations at the time of the InSAR data acquisitions may potentially be used to reduce this tradeoff.

We conclude that the R-based resampling is a robust technique that circumvents some of the problems that other resampling techniques have with noisy data, but that still provides dense sampling in regions where the data has the most relevant structure for the deformation source of interest. In this paper we only considered InSAR data, but our resampling algorithm could be easily applied to other forms of spatially dense geodetic imagery such as pixel tracking using optical or radar images (e.g., *Michel and Avouac*, 2002; *Simons et al.*, 2002). We also demonstrate the need to include the

spatial correlation of InSAR noise in inversions for earthquake parameters, especially when the signal of interest has approximately the same spatial scale as the noise. Combining these two techniques optimizes the amount of information we can extract from InSAR data.

Chapter 2

Little Skull Mountain earthquake

Published by American Geophysical Union in *Journal of Geophysical Research* by R. B. Lohman, M. Simons and B. Savage.

Abstract

We use Interferometric Synthetic Aperture Radar (InSAR) and broadband seismic waveform data to estimate source parameters of the June 29, 1992, M_s 5.4 Little Skull Mountain (LSM) earthquake. This event occurred within a geodetic network designed to measure the strain rate across the region around Yucca Mountain. The LSM earthquake complicates interpretation of the existing GPS and trilateration data, as the earthquake magnitude is sufficiently small that seismic data does not tightly constrain the epicenter, but large enough to potentially affect the geodetic observations. We model the InSAR data using a finite dislocation in a layered elastic space. We also invert regional seismic waveforms both alone and jointly with the InSAR data. Due to limitations in the existing data set, InSAR data alone can not determine the area of the fault plane independent of magnitude of slip, nor the location of the fault plane independent of the earthquake mechanism. Our seismic waveform data tightly constrains the mechanism of the earthquake, but not the location. Together, the two complementary data types can be used to determine the mechanism and location, but cannot distinguish between the two potential conjugate fault planes. Our preferred model has a moment of about 3.2×10^{17} Nm (M_w 5.6) and predicts a line length change between the Wahomie and Mile geodetic benchmarks of about 5 mm.

2.1 Introduction

Yucca Mountain, a proposed long-term (10^3-10^5 yrs) disposal site for high-level radioactive waste, is located within the Nevada Test Site in the southwestern Basin and Range province (Figure 2.1). The Basin and Range is an extensional province characterized by Cenozoic faulting and volcanism. Estimates of the current earthquake and volcanic hazard of the proposed site are complicated by the very low strain rates and short period of time within which they have been measured geodetically (i.e., less than 20 years). As a result, strain rates derived from the long-term geologic record may not be representative of current conditions since the space-time-dependence of strain is not well understood (e.g., *Wallace*, 1984).

Yucca Mountain lies within the southwestern Nevada volcanic field, a series of middle Miocene (15-7.5 Ma) silicic ashflow tuffs that have been tilted slightly eastwards since their formation (*Frizzell and Shulters*, 1990; *Sawyer et al.*, 1994). Several small basaltic eruptions occurred during the Quaternary within 10-20 km of Yucca Mountain, with estimates of the most recent age at 81-77 kyr b.p. (*Zreda et al.*, 1993; *Heizler et al.*, 1999). Crater Flat and Jackass Flat to the west and east of the site (Figure 2.1) both contain active faults (*Ferrill et al.*, 1996; *Fridrich*, 1999; *Fridrich et al.*, 1999).

A network of geodetic benchmarks was established in 1983 to characterize the deformation across this region (*Savage et al.*, 1994). This network has been subsequently resurveyed in campaigns using both trilateration and Global Positioning System (GPS) surveys. A trilateration survey using measurements from 1983, 1984 and 1993 (*Savage et al.*, 1994) indicates 8 ± 20 nstrain yr^{-1} of strain accumulation in a N65degW direction. A re-estimate of the strain rate using campaign GPS observations spanning 1991-1997 suggests strain accumulation of 50 ± 9 nstrain yr^{-1} in the N65degW direction (*Wernicke et al.*, 1998).

Differences between these two studies depend, in part, on the treatment of the M_s 5.4 Little Skull Mountain (LSM) earthquake that occurred on June 29, 1992, approximately 30 km to the southeast of Yucca Mountain (Figure 2.1). The LSM

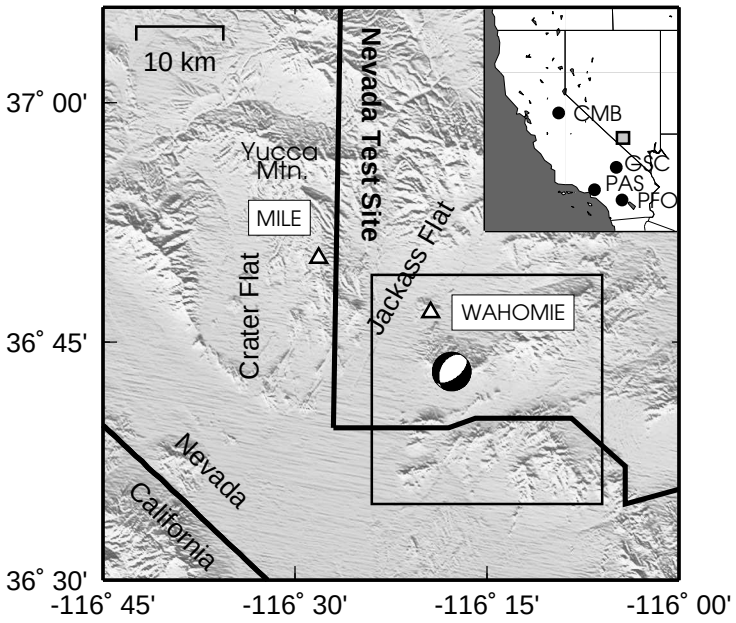

Figure 2.1: Shaded relief map showing the Mile and Wahomie geodetic benchmarks as triangles, the LSM focal mechanism from the Southern Great Basin Seismic Network (SGBSN), and the boundary of the Nevada Test Site. The box shows the location of Figure 2.2. The inset in the upper right of the figure indicates the locations of seismic stations used in this study. Mercator projection.

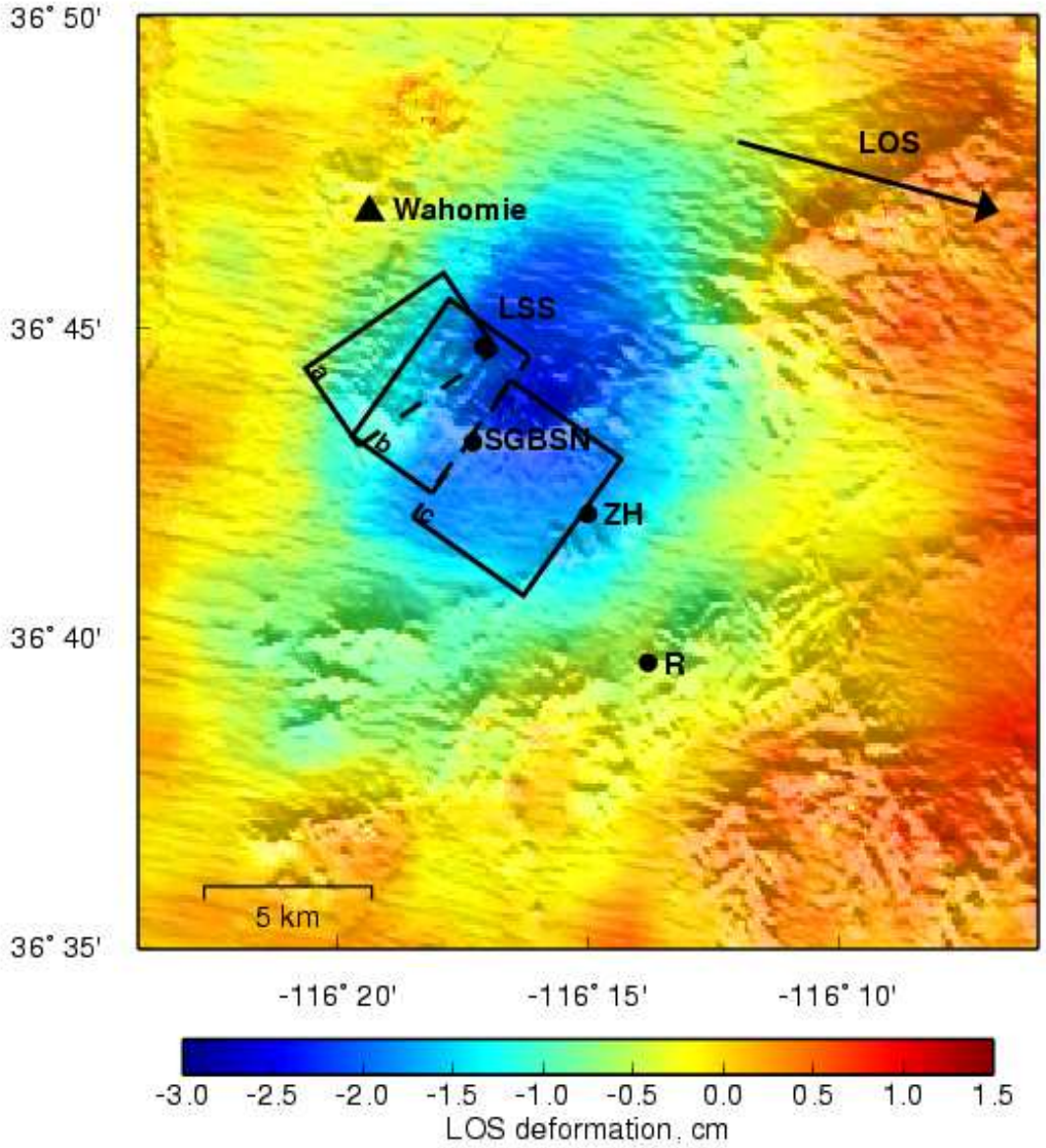

Figure 2.2: Averaged interferometric LOS displacement field used in the inversions. The arrow indicates the surface projection of the LOS vector from the ground to the satellite. Small-scale fluctuations in the displacement field are due to tropospheric and ionospheric variations between scene acquisition dates. Geodetic benchmark Wahomie is shown as a filled triangle. Solid circles indicate the LSM epicenter locations from the Southern Great Basin Seismic Network (SGBSN), *Zhao and Helmberger* (1994) (ZG), *Romanowicz et al.* (1993) (R) and from our joint inversion using the Mojave layered model (LSS). Rectangles show the map view projections of the fault planes used by (a) *Savage et al.* (1999), and the (b) SE-dipping and (c) NW-dipping planes in *Wernicke et al.* (1998). The dashed line indicates the bottom of the plane in all cases. Mercator projection.

earthquake was small enough that we expect it to affect only the southeastern-most stations in either network, most notably the horizontal changes in line length, ΔL_{wm}, between the Wahomie and Mile benchmarks. While the mechanism of the earthquake is constrained from seismic studies (Table 2.1), determining the fault area and which nodal plane ruptured is difficult due to the small size of the earthquake. In addition, the seismically located epicenters vary over a spatial range of about 11 km (Table 2.1). Studies of aftershock hypocenters show that they cluster near the SE-dipping plane (*Harmsen*, 1994; *Meremonte et al.*, 1995; *Smith et al.*, 2000). Based on the orientation of surface faults in the area, *Wernicke et al.* (1998) prefer the NW-dipping plane. A model with a finite dislocation on the SE-dipping plane in an elastic half-space (*Okada*, 1985) predicts horizontal elongation of ΔL_{wm} by about 7 mm, while slip on the NW-dipping plane predicts ΔL_{wm} changes of less than 1 mm (*Wernicke et al.*, 1998).

The interpretations of *Savage et al.* (1999) and *Wernicke et al.* (1998) differ in that they use seismic locations for the earthquake that are several kilometers apart (Figure 2.2). Both studies assume a fault area of 5×5 km, but *Wernicke et al.* (1998) assume that the two planes that they model share a common base, not their center. This assumption results in the top of the NW-dipping plane being around 6 km to the southeast of their candidate SE-dipping plane, such that models using the NW-dipping plane affect the geodetic benchmark Wahomie much less than those using the SE-dipping plane.

We investigate the mechanism and location of the LSM earthquake using Interferometric Synthetic Aperture Radar (InSAR) data from the ERS 1 satellite and regional broadband seismic waveform data. In the process of determining the best-fitting earthquake parameters, we demonstrate the complementary nature of the InSAR and seismic data for use in studies requiring precise earthquake locations.

Reference/Model	Lat (deg)	Lon (deg)	Depth (km)	Strike (deg)	Dip (deg)	Rake (deg)	Moment (Nm)
Romanowicz et al. (1993)[a]	36.66	116.23	8	43	66	-73	3.5×10^{17}
Romanowicz et al. (1993)[b]	36.66	116.23	8	34	44	-70	2.6×10^{17}
Walter (1993)[c]	36.718	116.289	10	35	54	-87	4.1×10^{17}
Harmsen (1994)[d]	36.72	116.295	10	55	56	-72	-
Zhao and Helmberger (1994)[e]	36.7	116.25	11	45	55	-60	3.0×10^{17}
Meremonte et al. (1995)[d]	36.72	116.295	10-11	55	56	-72	-
Wernicke et al. (1998), SE	36.707	116.263	8.0	35	54	-90	4.5×10^{17}
Wernicke et al. (1998), NW	36.726	116.299	7.5	215	36	-90	4.5×10^{17}
Savage et al. (1999)	36.741	116.312	8.3	55	56	-90	4.0×10^{17}
Smith et al. (2000)[d]	36.719	116.296	9.0	60	70	-70	4.5×10^{17}
This study-InSAR only							
Half space	36.743	116.242	10.6	47	38	-55	4.4×10^{17}
Standard Southern California[1]	36.742	116.247	11.1	39	37	-61	5.8×10^{17}
Mojave[2]	36.745	116.243	11.2	52	40	-51	5.0×10^{17}
This study-seismic only							
Standard Southern California[1]	36.613	116.441	10.9	35	48	-80	3.32×10^{17}
Mojave[2]	36.597	116.439	11.8	35	43	-81	2.47×10^{17}
This study-joint seismic and InSAR							
Standard Southern California[1]	36.747	116.283	9.5	38	58	-76	4.1×10^{17}
Mojave[2]	36.745	116.285	9.4	36	58	-78	3.2×10^{17}

Table 2.1: Little Skull Mountain Earthquake Parameter Estimates: Latitude, longitude, and depth for finite fault planes refer to the center of the fault plane. Moment is calculated using μ=35 GPa for the Mojave model, 42 GPa for the Standard Southern California model, and 33 GPa for all others. Superscripts refer to method used in each inversion: (a) Regional surface waves (b) Regional body waves (c) Single very broadband station (d) Aftershock hypocenters (e) Broadband waveforms, and layered elastic spaces from (1) *Hadley and Kanamori* (1977) and (2) *Jones and Helmberger* (1998)

Table 2.2: ERS 1 data used in this study: $B_\perp$ refers to the perpendicular component of the baseline between satellite locations and H_a is the ambiguity height for a given pair of SAR images, all with respect to the first image on 1992/04/24 (e.g., *Massonnet and Feigl*, 1998; *Rosen et al.*, 2000).

Date	Track	Frame	Orbit	$B_\perp$ (m)	H_a (m)
1992/04/24	399	2871	4051	-	-
1993/05/14	399	2871	9562	62	128
1993/06/18	399	2871	10063	40	198
1995/09/24	399	2871	21930	131	60

2.2 InSAR and seismic waveform data

We use ROI_PAC, the Caltech/JPL InSAR processing suite, to produce unwrapped geocoded interferograms. We combine the one existing SAR image acquired before the earthquake with three post-earthquake images to create three interferograms spanning different time periods (Table 2.2). We neglect any potential time-dependent post-seismic deformation and average the three interferograms to reduce ionospheric and tropospheric noise. As there is only one pre-seismic scene, any noise within it is carried through to our final averaged interferogram. We remove the effects of topography in the interferograms using a 90 m digital elevation model [*http://earthexplorer.usgs.gov*], leaving a measurement of surface deformation in the satellite line-of-sight (LOS) direction (Figure 2.2).

The relative LOS displacement reaches a maximum of 2.4 cm across an elliptical region in the center of the interferogram (Figure 2.2). Because the LOS vector is approximately 23° from vertical, we infer that this deformation is mostly due to subsidence. We interpret the smaller amorphous features, with magnitudes of around 1 cm and dimensions of 1-5 km that are visible across the image, as radar phase delays introduced by tropospheric and ionospheric perturbations. These delays are approximately 20% of the main earthquake signal and therefore introduce a large error term that is difficult to quantify. Only data from descending orbits is available, therefore only one component of the displacement field is observable. Since we can only measure deformation in the LOS direction, we must rely on models of coseismic deformation in order to make predictions of ΔL_{wm}. In addition, the atmospheric

Table 2.3: Layered elastic models used in this chapter. Superscripts refer to (1) *Jones and Helmberger* (1998) and (2) *Hadley and Kanamori* (1977)

Mojave[1]			Standard SoCal[2]		
Depth (km)	Density (g/cm^3)	Vp (km/s)	Depth (km)	Density (g/cm^3)	Vp (km/s)
2.5	2.40	5.00	5.5	2.40	5.50
5.5	2.40	5.50	16.0	2.67	6.30
28.0	2.67	6.30	35.0	2.80	6.70
half space	3.42	7.85	half space	3.00	7.80

errors are large enough that comparisons of individual points of the interferogram are unreliable, such that comparisons of models which fit the entire interferogram are more robust than direct measurements of LOS displacement.

We model the InSAR data for the earthquake using a finite dislocation model. We consider both an elastic half space (*Okada*, 1985) and the Standard Southern California (*Hadley and Kanamori*, 1977) and Mojave (*Jones and Helmberger*, 1998) layered elastic models (Table 2.3). We sample the interferogram on a non-uniform grid with a spacing proportional to the curvature of the LOS component of the displacement field (Simons et al., manuscript in preparation, 2001). This sampling reduces the number of Green's functions that must be evaluated for each iteration and therefore greatly improves the speed of our inversions.

We use regional seismic waveform data for the LSM earthquake recorded at distances of 150 to over 1000 km, at four stations (CMB, GSC, PAS and PFO) in the TERRAscope and Berkeley Digital Seismic Networks (Figure 2.1). Seismic data at these ranges is dominated by refracted compressional energy (Pnl), reflected shear waves, and large amplitude surface waves. Refracted energy arrives much earlier than the shear and surface waves, but the waveforms are dominated in amplitude and duration by the later arriving surface waves. Since Pnl arrivals are sensitive to the depth of the earthquake and fault plane orientation, we enhance the Pnl section of the seismic signal relative to the surface waves using the method of *Zhao and Helmberger* (1994).

Attempts to fit Pnl and surface waves are difficult in absolute time, since approxi-

mations of the elastic structure of the lithosphere introduce errors into the synthetics. Therefore, we shift and filter the data and synthetics so that they only reflect the general properties of the crust and lithosphere. Aligning the synthetics with the data in time acknowledges that our seismic data lacks the power to well-resolve the epicenter location. Pnl waveforms are filtered to include higher frequencies (0.01 - 0.2 Hz) than the full waveforms (0.01 - 0.05 Hz) to better identify the depth phases that constitute Pnl. We compute synthetics using an F-K double integration (*Wang and Herrmann*, 1980) in both the Standard Southern California and Mojave layered elastic models (Table 2.3) and compare these synthetics to the data on a point by point basis in a least squares sense.

2.3 Source parameter inversions

The root mean squared (RMS) misfit between the data and our model depends on the value of nine parameters defining the location and orientation of the fault plane and the amount and direction of slip that occurred during the earthquake. Traditional gradient searches may fail to find the true minimum in such a nonlinear problem. Rather than using a grid search to explore the parameter space associated with this event, which involves evaluating the forward model many times in regions with potentially high misfit, we use the Neighborhood algorithm (NA) developed by *Sambridge* (1998a,b).

The NA method has advantages over techniques such as genetic algorithms and simulated annealing in that it produces a more complete image of the misfit function over the entire parameter space, while concentrating sampling in the regions with lowest misfit. This approach is important for studies such as ours with multi-dimensional, nonlinear parameter spaces, where inferring the global minimum is only part of the full characterization of the misfit behavior. The ensemble of models and misfits produced by the NA algorithm illustrates the broadness and uniqueness of the minima, and shows the tradeoffs that may exist between sets of parameters.

2.4 Results and implications

For the InSAR-only inversion, we allow the inversion to search through the entire possible range for each parameter, letting strike, dip and rake vary as well as area, location and amount of slip, all assuming a square fault plane. We find a large tradeoff between slip and area (Figure 2.3a), whereas the seismic moment is well-constrained to be about 4.4×10^{17} Nm (M_w 5.7, Figure 2.3b). Since the area is not well-constrained by our data, we adopt a value of 25 km^2 as estimated from aftershock distributions (*Harmsen*, 1994; *Meremonte et al.*, 1995; *Smith et al.*, 2000) and that is used in previous studies (*Wernicke et al.*, 1998; *Savage et al.*, 1999). This assumption does not affect our conclusions regarding the line length changes between geodetic benchmarks Wahomie and Mile. The inversion slightly prefers models with SE-dipping planes, but this is only for planes that are larger than about 100 km^2 (Figure 2.3c). As the fault planes get smaller, they approach a point source and are, by definition, indistinguishable from each other. Even for the larger fault planes, the difference in misfit is small and our InSAR data cannot unambiguously distinguish between the two potential rupture planes.

When we invert using only the InSAR data, and assume a fixed fault area of 25 km^2, a search through the entire range of potential mechanisms suggests a best fitting mechanism with a rake of $-55°$. This estimate of the rake is much shallower (i.e., with a greater component of strike-slip faulting) than predictions from previous seismic studies (Table 2.1). Figure 2.3d shows the map view locations of best-fitting fault planes of area 25 km^2 from inversions where we fixed the rake at values between $-20°$ and $-100°$. All of these models have similar misfits to the InSAR data, illustrating the tradeoff between earthquake mechanism and fault plane location inherent with this set of InSAR data. If additional InSAR data existed with a different LOS direction, we would be better able to determine the mechanism.

To explore the dependence of these inversions on the availability of different LOS components, we produced synthetic data similar to the LSM earthquake for both ascending and descending tracks. We added several different sets of noise taken from

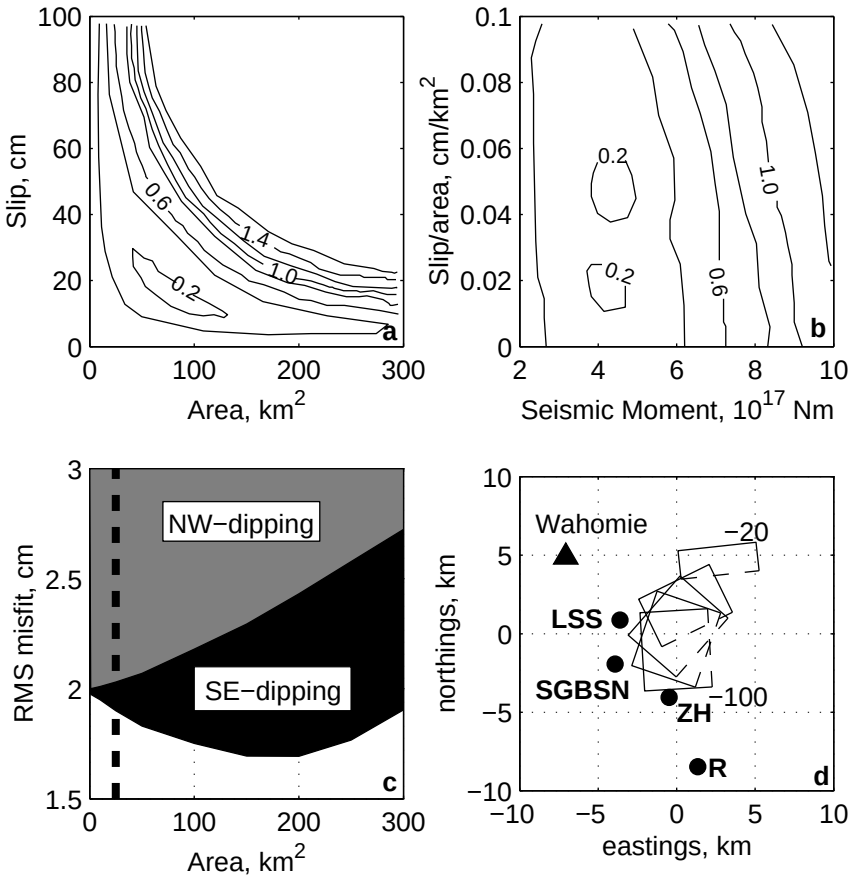

Figure 2.3: (a) Contours of RMS model misfit versus fault plane area and amount of slip. Misfit continues to increase to the upper right of the panel. (b) Contours of RMS model misfit versus moment and slip/area. Moment is calculated using μ=33 GPa. (c) Area versus RMS model misfit for SE-dipping fault planes (black) and NW-dipping fault planes (gray). The 25 km^2 area used by previous workers is indicated by a heavy dashed line. (d) Map view location of best-fitting planes with area 25 km^2 and rake fixed at values between -20 deg and -100 deg. Solid circles indicate LSM epicenter locations as in Figure 2.2. All panels show results from inversions using only InSAR data and assuming an elastic half space. The inversion behavior is similar for the layered spaces and our joint inversions. This and all subsequent maps use a UTM (zone 11) projection.

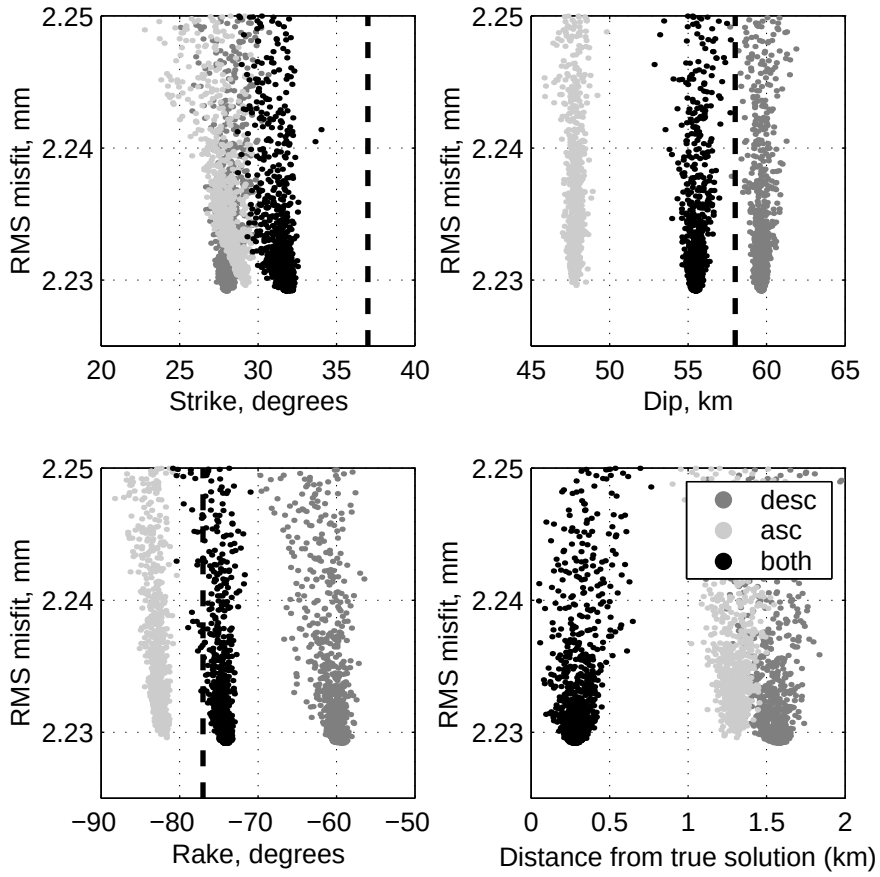

Figure 2.4: RMS model misfit versus strike, dip, rake and the absolute distance from the true solution, indicated by the black dashed line. These inversions use synthetic data with noise taken from the real, observed interferogram. The light gray and dark gray dots correspond to models from inversions using just data from ascending or descending satellite tracks. The black dots are models that use both sets of synthetic data.

sections of our observed interferogram to this synthetic data. We ran inversions on each data set separately and then compared them to the inversion using both data sets simultaneously. Figure 2.4 shows the RMS value versus strike, dip, rake and the absolute distance from the true solution for models produced during these inversions. As expected, for each parameter the inversion using both LOS directions (black dots) comes closest to the real value used to compute the synthetic data. For this example, we find that we can estimate the hypocenter location to within half a kilometer.

Despite the tradeoff between fault area and slip, as well as between location and mechanism, some earthquake parameters are well-determined by the InSAR data.

The InSAR-only inversion using an elastic half space model tightly constrains ΔL_{wm} to be around 6 mm. InSAR-only inversions using both the Standard Southern California and Mojave layered elastic models predict results similar to that of the half space inversion, except that the inferred hypocenter depths are around 400-500 m deeper and the moment is slightly larger for the layered models (Table 2.1). Inversions in layered elastic models involve a tradeoff between the layered structure and the distribution of slip. Both of the layered models that we use have less-rigid layers above the earthquake than below, which results in a greater predicted depth than from inversions in a half space. In our inversion, the increase in depth suggested by the inversion using less rigid layers above the earthquake than below requires that more slip be placed on the fault plane to match the surface deformation. We prefer the Mojave layered elastic model because it includes more realistic structure in the upper 10 km than does the Standard Southern California model.

Our seismic data tightly constrains the mechanism of the LSM earthquake, but contains relatively little information on the location. The Mojave model predicts a slightly deeper event (11.8 km) than the Standard Southern California model (10.9 km), but most other parameters are similar. Both layered elastic models predict mechanisms that are well within the range of predictions from previous seismic studies. Both of these mechanisms fit our seismic data very well, but do not fit the InSAR data well because of the poorly constrained location. Table 2.4 shows the misfit to InSAR and seismic data for our different sets of models and for some of the seismic locations and mechanisms.

Our initial attempt at a simultaneous joint inversion calculates misfits to both our seismic and InSAR data. The correct relative weighting of the two data types is difficult to determine, as errors in InSAR data are poorly understood. We weighted the data based on the RMS value of each data type. This inversion approach results in models that average the parameters from the InSAR-only and seismic-only inversions and fit neither data set well. Using the InSAR data to relocate the best-fitting mechanism inferred from only our seismic data produces a better result. We iterate between seismic-only and InSAR-only inversions multiple times. This process is much

Table 2.4: Misfit values in this study. Superscripts as in Table 2.1.

Reference/Model	RMS misfit (mm) (InSAR)	RMS misfit (seismic)
Romanowicz et al. (1993)[a]	7.504	1.285
Romanowicz et al. (1993)[b]	5.316	1.260
Walter (1993)[c]	3.441	1.391
Zhao and Helmberger (1994)[e]	4.172	1.287
Wernicke et al. (1998), SE	4.710	1.593
Wernicke et al. (1998), NW	5.137	1.618
Savage et al. (1999)	4.607	2.254
Smith et al. (2000)[d]	4.726	1.287
This study-InSAR only		
Half space	2.616	1.444
Standard Southern California[1]	2.455	1.426
Mojave[2]	2.557	1.436
This study-seismic only		
Standard Southern California[1]	5.960	1.067
Mojave[2]	5.743	1.086
This study-joint seismic and InSAR		
Standard Southern California[1]	2.853	1.185
Mojave[2]	2.923	1.179

more cost-effective than the computationally expensive simultaneous inversion. Table 2.1 summarizes the results of this inversion and Figure 2.5 shows the mechanism for the Mojave elastic model and the associated misfits. This result fits both our seismic and the InSAR data well (Table 2.4. Synthetic waveforms calculated from the best-fitting mechanism from the inversion using only InSAR data do not fit our seismic data nearly as well as does the one from the joint inversion (Figure 2.5). The joint InSAR/seismic inversion in the Mojave layered produces a mechanism that is 1 km shallower than the InSAR-only inversion in a half space and predicts a moment of 3.2×10^{17} Nm (M_w 5.6). Our joint inversion constrains ΔL_{wm} to be around 5 mm. Figure 2.8 shows ΔL_{wm} versus the RMS misfit to our InSAR data for models calculated during our joint inversion in the Mojave layered elastic model.

Since the InSAR data provides additional constraint on the location of any given mechanism, it is useful to examine previous solutions for the LSM earthquake and their effects on the estimates of ΔL_{wm}. We first compare predictions from the fault plane solutions used previously by *Wernicke et al.* (1998) and *Savage et al.* (1999) with the InSAR data (Figure 2.6). All three models have significant residuals when subtracted from the InSAR data (Figure 2.6). We relocate these three mechanisms, allowing the location and amount of slip to vary, but keeping the strike, dip, rake, and fault area fixed. All three mechanisms relocate to within 500 m of each other (Figure 2.7) and predict similar residuals (Figure 2.6). These relocated fault planes fit the InSAR data almost as well as our best-fitting solutions, and predict Wahomie-Mile line length changes of 4-5 mm. These relocations show that, although the InSAR and seismic data cannot unambiguously distinguish between the two potential rupture planes, they require that both fault planes centers are at approximately the same location. The two planes therefore affect the ΔL_{wm} similarly, since they are effectively point sources. We also relocate the mechanism of *Smith et al.* (2000), resulting in a hypocenter that is within 2 km of our best model. This model fits the InSAR and seismic data worse than either our best model or the other relocated mechanisms.

Figure 2.5: Mechanisms, observed waveforms, and synthetic waveforms from the joint and InSAR-only inversions using the Mojave layered model. Pnl waveforms are filtered from 0.01-0.2 Hz, while full waveforms are filtered from 0.01-0.05 Hz. Data are shown as black lines and synthetics as gray lines. The time scale is shown at the base of each group of plots, with the 20 second bar referring to the Pnl waveforms and the 60 second bar referring to the full waveforms.

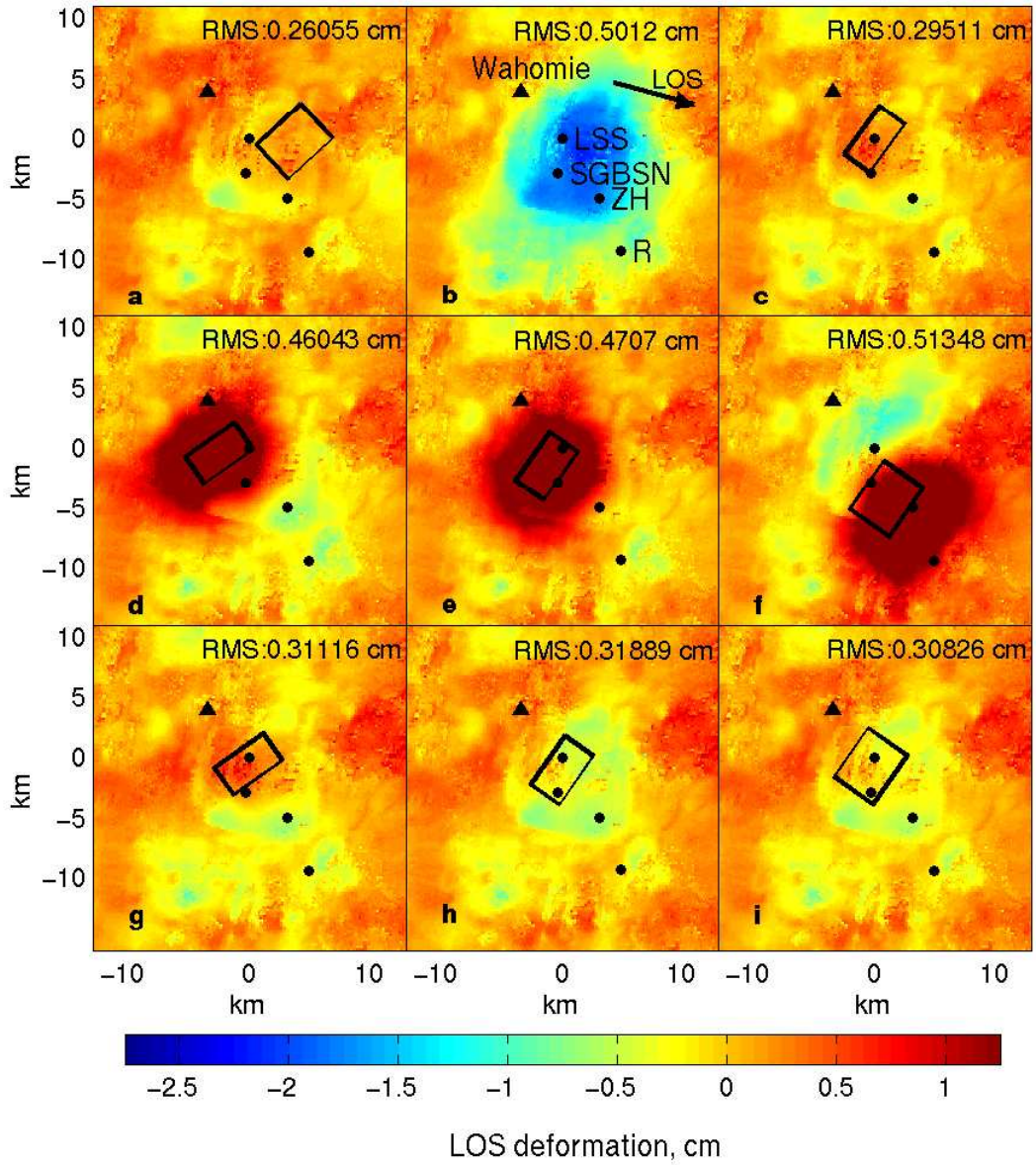

Figure 2.6: RMS residuals between various models and the interferogram. The color scale is the same for each panel. The surface projection of the fault plane used in each case is shown as the black rectangle, with the bottom of the plane as a thin line. The location of benchmark Wahomie is shown as a triangle. (a) Residual between the interferogram and the best model from our inversion in the Mojave layered space using just InSAR data, area fixed at 25 km^2. (b) The original interferogram. (c) Residual between the interferogram and the best model from our joint InSAR-seismic inversion in the Mojave layered model. (d,e,f) Residuals for the models used in *Savage et al.* (1999) and the SE-dipping and NW-dipping planes of *Wernicke et al.* (1998), respectively. (g,h,i) Residuals for the same three models after relocation. We fix the strike, dip, rake, and area of each of the three models, and allow the (x,y,z)-position and amount of slip to vary. Solid circles indicate LSM epicenter locations as in Figure 2.2.

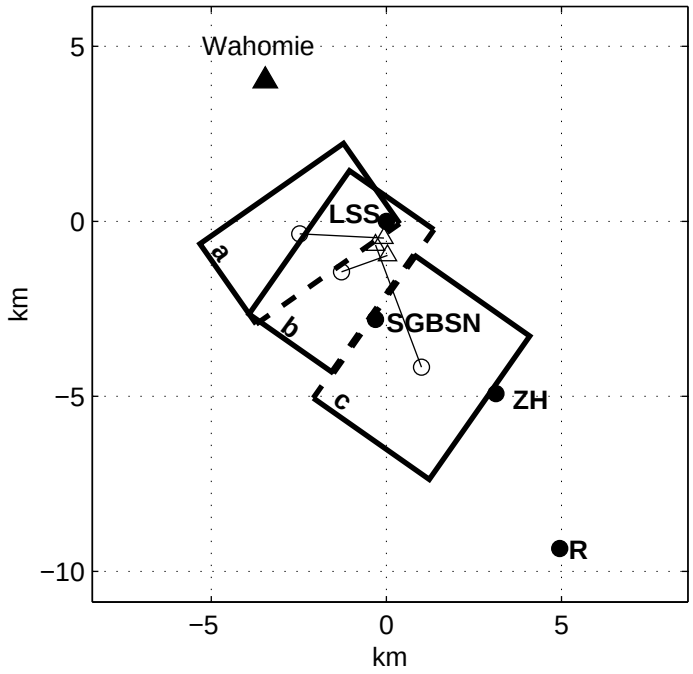

Figure 2.7: Rectangles indicate original positions of (a) the SE-dipping plane used by *Savage et al.* (1999) and the (b) SE and (c) NW-dipping planes in *Wernicke et al.* (1998). The bottom of each plane is dashed, and the center of the original plane is shown as a circle. Our relocated centers are plotted as triangles, demonstrating that all three cluster within a few hundred meters of each other. Solid circles indicate LSM epicenter locations as in Figure 2.2.

2.5 Conclusions

InSAR data can effectively locate shallow earthquakes that are too small or too distant to accurately locate using traditional seismic methods. In this study, the InSAR data is sensitive to the seismic moment of the earthquake, but suffers from a tradeoff between mechanism and location. Our seismic data is sensitive to the mechanism, but not very sensitive to the location. For the LSM earthquake, both data types are unable to separate area from magnitude of slip, or to distinguish which of the two potential conjugate planes ruptured. The main observational limitations of this study are the availability of only one SAR image before the earthquake and the existence of only one component of deformation.

Despite the lack of many independent interferograms, the different sets of models that we consider all have less than 3 mm of RMS misfit with the InSAR data, with peak misfits of about 1.5 cm. All earthquake mechanisms that fit both the InSAR and seismic data have similar effects on ΔL_{wm}, with a predicted elongation of 4 to 8 mm (Figure 2.8). This estimate of ΔL_{wm} is consistent with predictions from the SE-dipping planes of both *Wernicke et al.* (1998) and *Savage et al.* (1999). Regional strain rates predicted using these corrections agree within 2σ error but not at the 1σ level (*Wernicke et al.*, 1998; *Savage et al.*, 1999).

We find that it is important to consider the effect of layered elastic models in inversions of this type. In this case, inversions in layered models produced deeper events than those in a half space, with up to 25% differences in estimated moment release. Hopefully, future studies of small earthquakes will have more independent interferograms and therefore will permit greater averaging to reduce noise. We must also be able to measure multiple components of the deformation in order to improve the ability of InSAR data to determine earthquake mechanisms.

Beyond the discussion of the LSM earthquake, this study supports the feasibility of the formation of a catalog of earthquakes located using both InSAR and seismic data. This catalog could support tomographic studies which can benefit from improved bounds on source locations. In many regions of the world, local seismic networks do

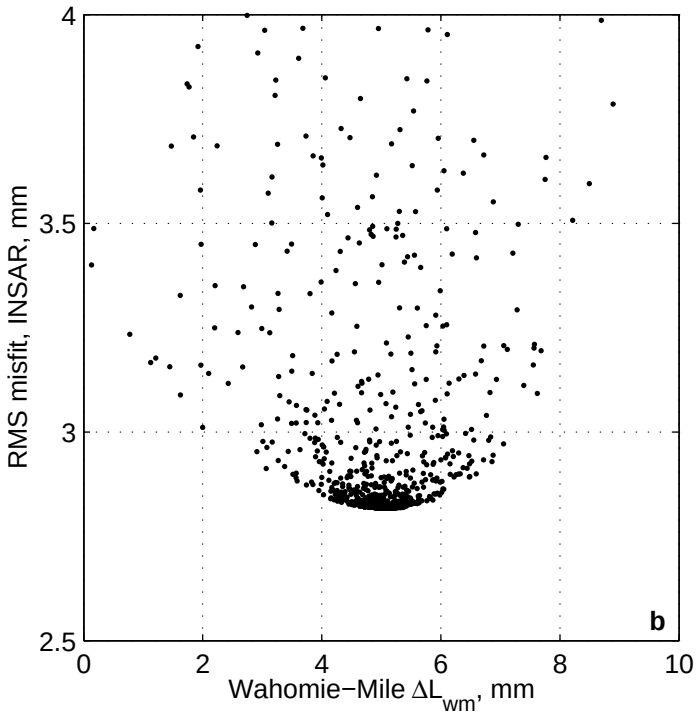

Figure 2.8: RMS model misfit with the InSAR data versus ΔL_{wm} for each model tested during our joint inversion using the Mojave layered elastic model.

not exist, and teleseismic and remote sensing data are the only sources of information about earthquake parameters. In these areas, teleseismic earthquake locations often have errors greater than 50 km. For many of these events, this uncertainty in location can be reduced by two orders of magnitude using joint inversions of InSAR and seismic data. Routine analysis of this sort requires the availability of a sufficiently large set of SAR data, such that there exist interferometrically useful images before and after all earthquakes of interest. Ideally, this SAR data library would include multiple sets of interferograms with ascending and descending pairs bracketing most earthquakes. A substantially more accurate earthquake catalog will provide critical input to tectonic studies in regions with shallow seismicity and poor seismic station coverage.

Chapter 3

Small earthquakes in the Zagros

Abstract

The Zagros mountains of Southern Iran accommodate a significant portion of the 3 cm/yr convergence between Arabia and Eurasia. The Zagros are marked by a zone of high seismicity ($M_w < 6$) that broadens from a narrow band along the collisional front in the NW to a wider belt (>150 km) in the south near the Straits of Hormuz. Due to the lack of dense local seismic or geodetic networks, much of our understanding of how the continental crust currently accommodates this strain is based on catalogs of teleseismically determined earthquake locations. It is not clear which folds are associated with seismicity, or whether earthquakes occur in the basement or in the overlying 10-15 km of sediments, as earthquake hypocenters in the Zagros are poorly determined.

I surveyed all $M_w > 4.5$ earthquakes in the Harvard CMT (HCMT) and International Seismological Centre (ISC) catalogs that were spanned by interferometric pairs with spatial baselines ($B_\perp$) less than 150 m and temporal baselines of less than 3-4 years. I present locations for 4 earthquakes and one deformation event that occurred in the Zagros mountains during the period 1992-2002 by examining ground deformation constrained by Interferometric Synthetic Aperture Radar (InSAR). I invert the observed deformation for the best-fitting fault plane for each earthquake, using the Neighborhood algorithm. I show that we can locate events with precisions of a few km in both map view and depth with InSAR data, allowing us to tie specific events to active structures. I also provide error bounds on the best-fit earthquake parameters, using Monte Carlo sensitivity tests. All of the earthquakes presented in this paper lie within the 10-15 km thick sedimentary section overlying Precambrian basement.

3.1 Introduction

Much of our understanding of how continental crust accommodates strain comes from studies of the spatial distribution of seismicity in actively deforming mountain belts. In places such as the Zagros mountains of Southern Iran (Figure 3.1), which accommodate a significant portion of the 3 cm/yr convergence between Arabia and Eurasia, there are no dense local seismic networks and we must rely on catalogs of teleseismically determined earthquake locations. These catalogs have been used both to describe and interpret the spatial distribution of seismically released strain (e.g., *Hessami et al.*, 2001), and to place bounds on the percentage of convergence which is accommodated seismically (e.g., *Jackson and McKenzie*, 1988). Both of these applications require high-quality earthquake locations and magnitude estimates. Cataloged teleseismic earthquake locations in this region commonly have errors of up to 50 km in map view (e.g., *Maggi et al.*, 2000; *Ambraseys*, 2001; *Talebian and Jackson*, 2004) and earthquake depths in the Zagros are poorly determined to the extent that it is unclear even whether earthquakes occur in the basement or in the overlying 10-15 km of sediments (e.g., *Jackson and Fitch*, 1981). The initial collision between Eurasia and Arabia occurred at ~20 Ma, and up to 70 km of convergence (e.g., *Talebian and Jackson*, 2002; *McQuarrie*, 2004) has subsequently occurred. Whether this is accommodated by continued subduction of the basement and decoupled, in-place shortening of the cover along detachments within the numerous salt and evaporite layers within the sedimentary section, or if the basement is shortening along thrust faults that cut through the salt layers and feed slip up into the surface folds is unknown. Part of our inability to describe the dynamics of shortening in the Zagros is due to our incomplete understanding of the spatial distribution of seismicity.

InSAR and seismology are complementary in that InSAR observations are very sensitive to the 3-D location and magnitude of smaller events, whereas seismology constrains the mechanism. We augment existing seismic catalogs with a set of precise earthquake locations inferred from Interferometric Synthetic Aperture (InSAR) observations. For thrust and normal-faulting events, the near-vertical component of

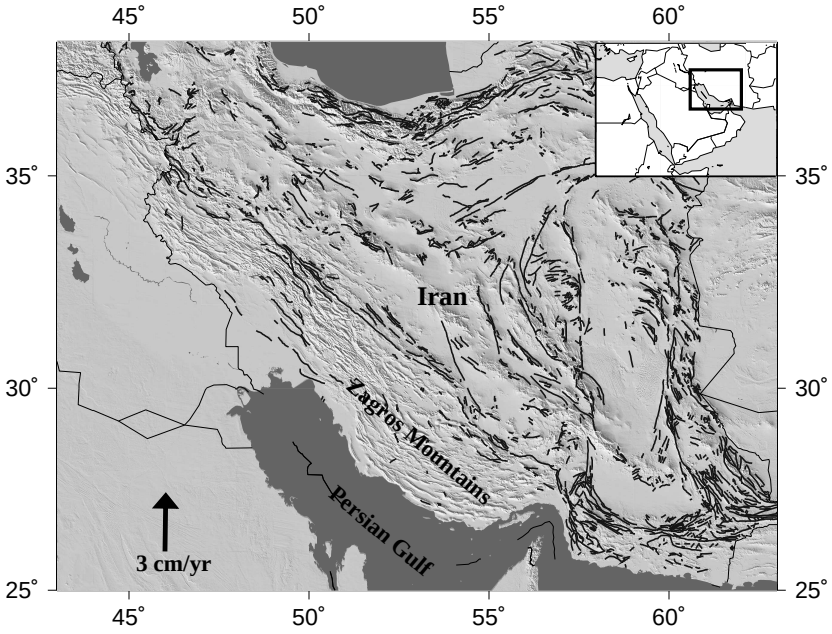

Figure 3.1: Reference map showing shaded relief and Zagros mountains of Southern Iran. Dark gray lines are active faults from *Berberian* (1981). Arrow in lower left shows velocity of Arabian plate with respect to Eurasia, from the Nuvel-1A model (*DeMets et al.*, 1994).

deformation measured by InSAR provides little constraint on the earthquake mechanism (e.g., Chapter 2). In this chapter, I infer locations with mechanisms constrained either by seismology or by inference from the local tectonic framework and surrounding structural trends.

3.2 Catalog search

The existing catalog of InSAR data from the ERS 1 and 2 satellites provides sparse temporal and spatial coverage over the Zagros mountains, with the highest data density in the south near the Straits of Hormuz. Since the number earthquakes with $M_w > 4.5$ in the Zagros that occurred between 1992 and 2002 is very large (greater than 500), I implemented an automated search procedure that extracts only earthquakes spanned by interferometric pairs with reasonable spatial and temporal baselines (less than 150 m and less than 3 years). From this much smaller family of earthquakes, I hand-checked against known problems with agricultural regions, sand dunes and steep topography. My final list included 96 potentially detectable earthquakes, spanned by $\sim$110 interferometric pairs (Figure 3.2).

3.3 Results

I located four earthquakes that I can potentially associate with specific cataloged events (Table 3.1, Figure 3.3). One region of observed deformation is not associated with any event in the seismic catalogs, or any topography that could induce an elevation-dependent atmospheric effect. I observe this deformation feature with the same magnitude in two independent interferograms that span different time frames, so I can potentially rule out that the deformation is due to changes in groundwater. In cases where I did not observe earthquake deformation, the most common cause is widespread decorrelation across the interferogram. If the InSAR data catalog was more complete and there were multiple interferometric pairs with short temporal baselines that spanned these earthquakes, it is likely that more of them would have

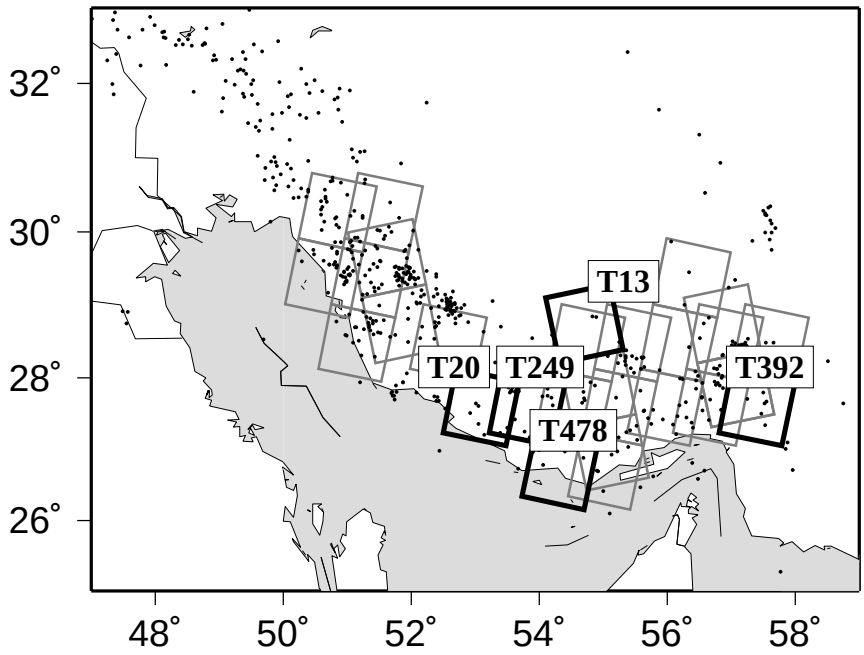

Figure 3.2: Reference map: Small dots indicate seismicity from ISC catalog between 1992-2002. Gray boxes indicate SAR frames that we examined in this study (some with multiple interferometric pairs), heavy outlines correspond to frames with observed deformation.

observable deformation signals. There are at least 13 cases of non-detection where we had a high-quality interferogram. In these cases, I infer that either the cataloged earthquake location is in error by more than $\sim 10 - 20$ km, so that the earthquake actually occurred outside of the InSAR frame, or that the depth is great enough that the earthquake deformation is undetectable within the observed level of noise. For earthquakes of M_w 4.5-5.0 and the use of only a single interferogram, this critical depth varies from approximately 5-15 km.

I infer earthquake properties from the observed deformation using the Neighborhood algorithm (*Sambridge*, 1998a,b; *Lohman et al.*, 2002), a nonlinear inversion technique that employs an intelligently driven global search that focuses on regions with the lowest data misfit. Some of the factors that may contribute systematic errors to our result include atmospheric noise correlated with topography and the inhomogeneous elastic structure of the real Earth. In the case of the 1999/04/30 event (Figure 3.4), there is an obvious negative correlation between the change in

Event	T/F	InSAR M_w/Z	HCMT M_w/Z/Err	ISC m_b/Z/Err	N
1997/05/05	478/3069	5.4/5.6	5.1/15/46	4.8/46/2	1
1997/09/18[a]	478/3069	4.9/3.5	-	4.7/55/4	1
1998/10/18	13/567	4.5/1.1	-	4.2/98/11	2
1999/04/30	20/3051[b]	5.3/3.3	5.2/45/67	4.9/35/7	3
Unknown	392/3051	4.7/2.3	N/A	N/A	2

Table 3.1: Track and frame (T/F), Insar, HCMT and ISC magnitudes, depths (Z, in km) and the location error in km of both the ISC and HCMT locations for each event considered in this chapter. N indicates the number of interferograms that show deformation for this event. [a] Earthquake occurred very near to larger event. [b] Signal also observed in overlapping track, T249

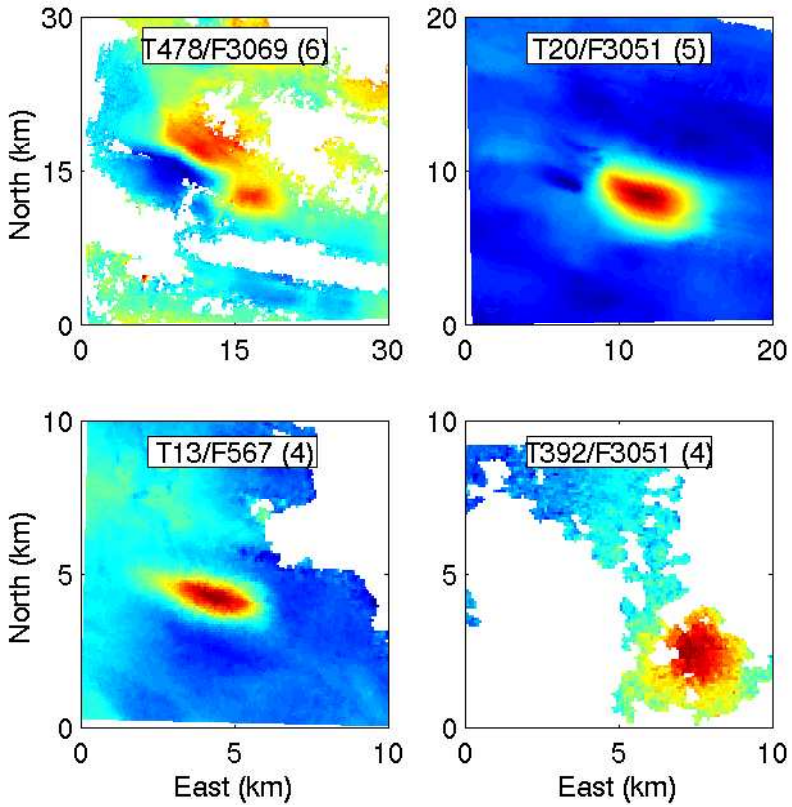

Figure 3.3: Subsets of interferograms for each track and frame with observed deformation. Colorscales vary, so range in cm is indicated in parentheses

LOS and topography along ridges to the north and south of the epicenter, with the effect that the earthquake deformation appears narrower and elongate along N 120°E. We expect that this effect will result in our inferring a shallower depth, and bias us toward a strike parallel with the valley. The T478 interferogram in Figure 3.5 spans two subevents, so I allowed the Neighborhood algorithm to simultaneously search for two separate fault planes.

I inverted for the best-fitting point sources and for the best-fitting finite fault patches for each event, with the results summarized in Tables 3.1-3.2 and Figures 3.4-3.7. For each event, I performed error analyses on the hypocenter locations using the full noise covariance matrix as described in Chapter 1. I created 500 synthetic data sets using the best-fitting slip models for each event and correlated noise using the noise covariance estimated directly from the data. I then inverted each synthetic data set without fixing the fault plane geometry or mechanism. When inverting for a point source, I fixed the size of the fault plane to 1 m$\times$1 m. In most cases the error bounds on location were to within a few 100 m, even with the correlated noise. Map view confidence ellipses are indicated in Figures 3.4-3.7, and 1σ error bounds on depth are tabulated in Table 3.2.

In Figure 3.4, the HCMT location, which is from a catalog often used in global tectonic interpretations, is off by more than 50 kilometers. The InSAR data allows us to precisely locate events that are too small to be well-located by either the HCMT or ISC catalog. With the InSAR data, we have little information about the mechanism of the earthquake, but can determine the location with a precision of 1-2 km in map view and depth. In this region of Iran, where there are very few seismic stations, InSAR is clearly vital for locating small earthquakes.

For each event, the InSAR-derived magnitude is larger than the magnitude from either seismic catalog (Table 3.1). This is due in part to the fact that I am not using a realistic layered rheology, which affects the inferred seismic moment. Also, each earthquake listed in Tables 3.1-3.2 has many associated aftershocks which are included in the time frame of the interferogram. Therefore, each location should be viewed as a centroid for the seismicity that occurred during that time period.

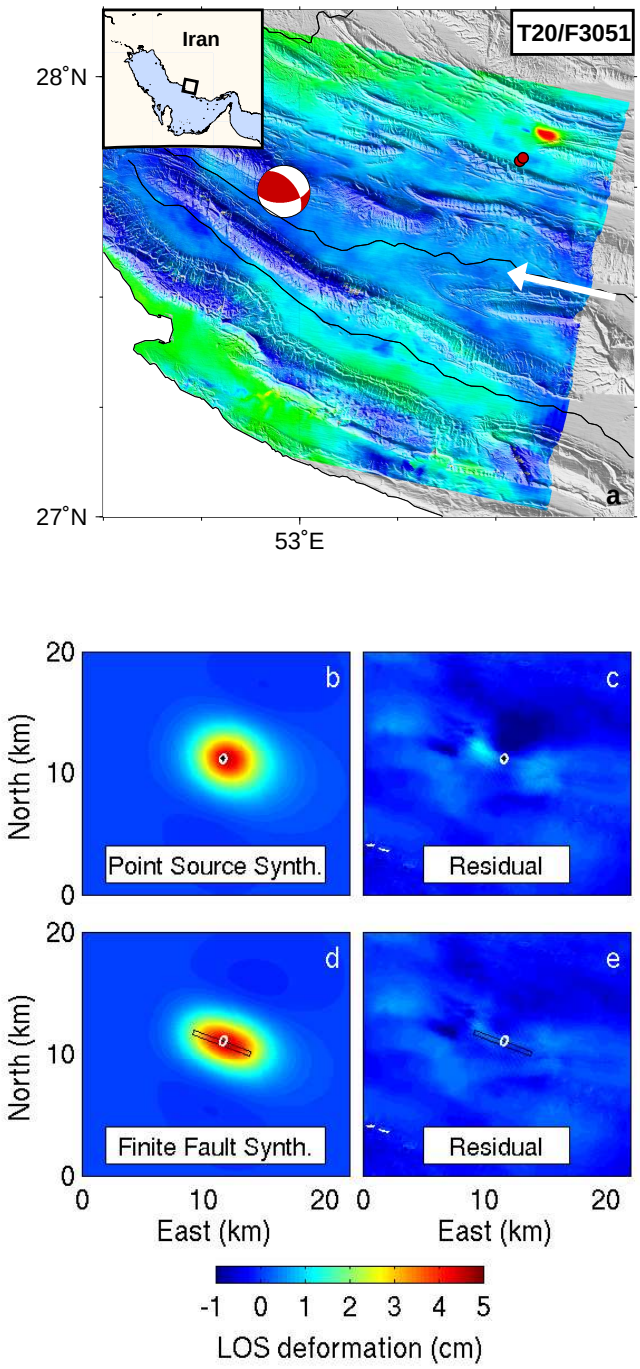

Figure 3.4: Interferogram and inversion results for T20/F3051 (1999/05/26-1999/04/21): Top figure shows an interferogram in the central Zagros mountain of Iran, overlain on topography, with LOS direction (satellite to ground, white arrow). Teleseismically-determined locations are indicated by the black focal mechanism (HCMT) and the red circles (ISC). Synthetics (b,d) and data residuals (c,e) for best finite fault patch and point source, with the best-fitting fault plane (black) and confidence interval on the fault plane center (white). Characteristics of noise: σ^2=0.18 cm, L_c=9.8 km

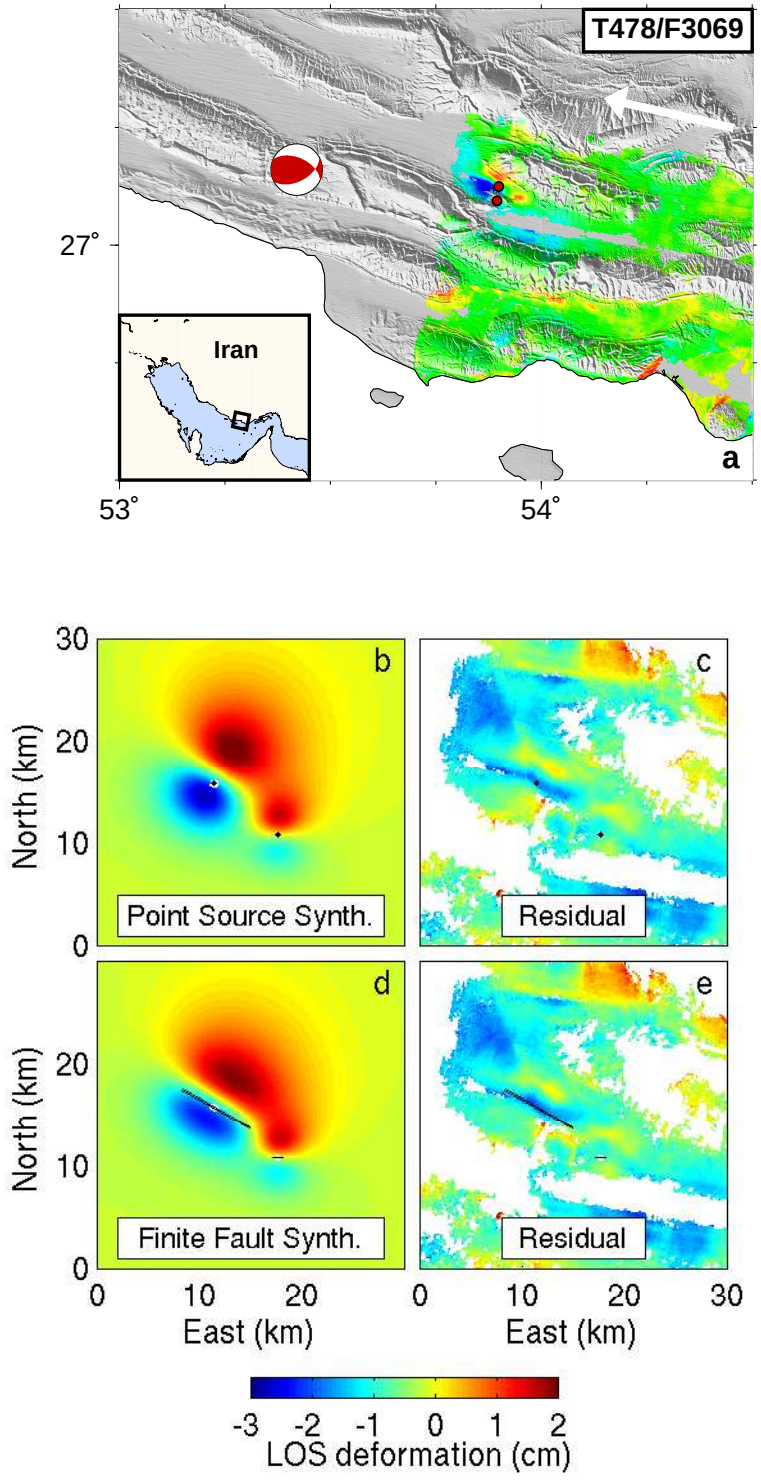

Figure 3.5: Interferogram and inversion results for T478/F3069 (1999/04/18-1996/04/28). Characteristics of noise: σ^2=0.16 cm, L_c=7 km

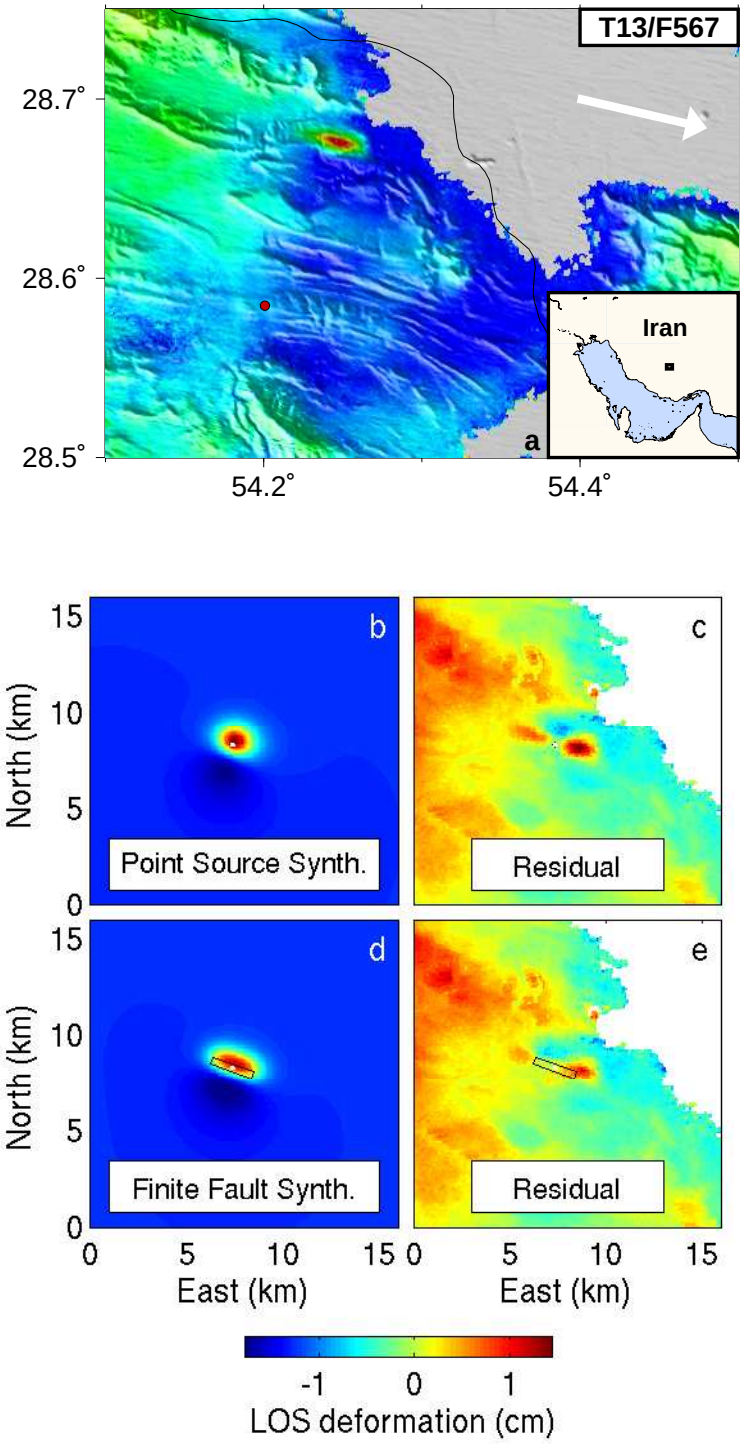

Figure 3.6: Interferogram and inversion results for T13/F567 (1999/09/07-1997/10/06). Red dot indicates ISC location for earthquake on 1998/10/18 (m_b 4.2). Note different LOS direction, since this is an ascending interferogram. Characteristics of noise: σ^2=0.28 cm, L_c=15 km

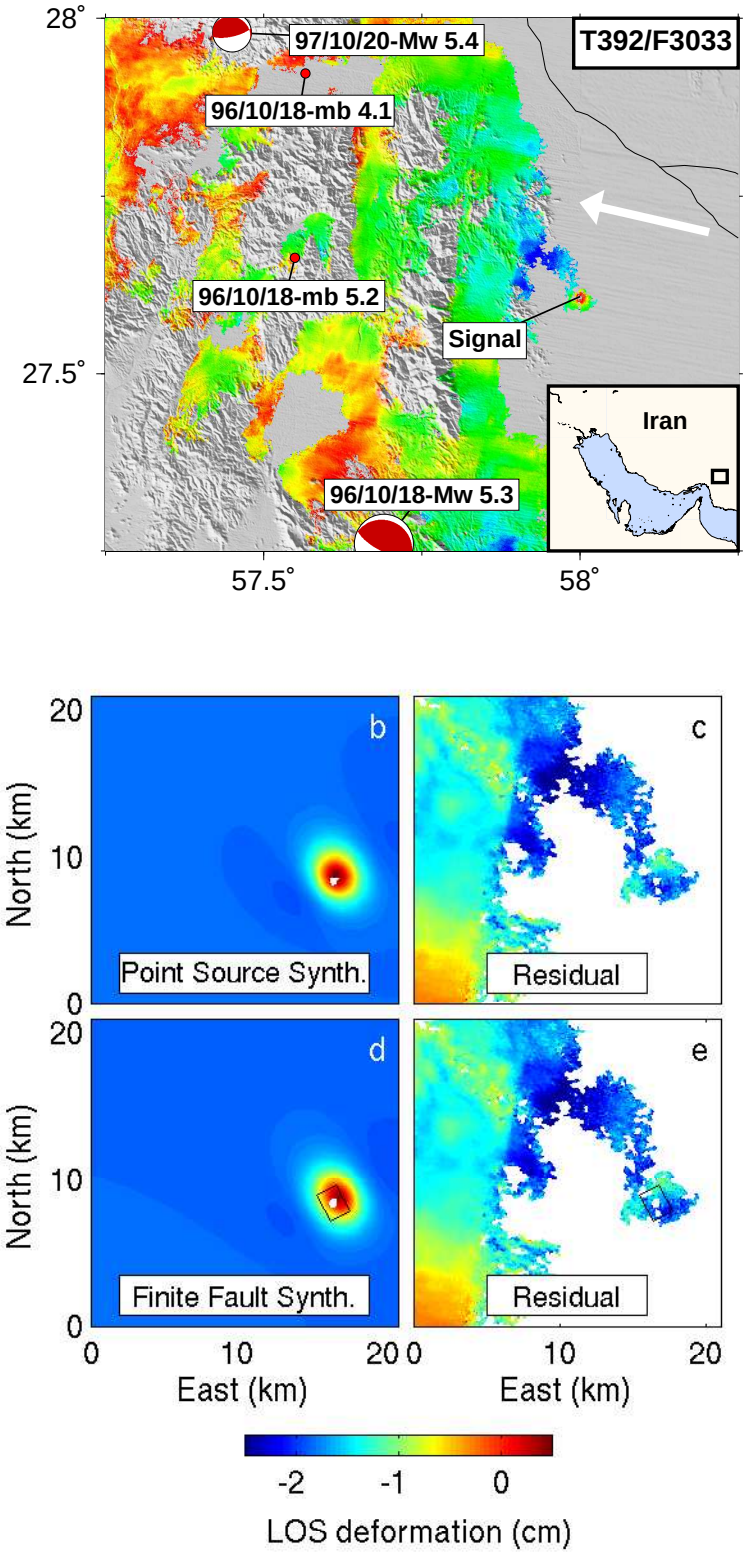

Figure 3.7: Interferogram and inversion results for T392/F3051 (1998/09/14-1996/05/26). Characteristics of noise: σ^2=0.22 cm, L_c=16 km

Point source

Event	M_w	Z(km)	Lon (deg)	Lat (deg)
1997/05/05	5.4	5.6 ±0.4	53.880 ±0.4 km	27.138 ±0.3 km
1997/09/18[a]	4.9	3.4 ±0.2	53.943 ±0.2 km	27.097 ±0.2 km
1998/10/01	4.5	1.3 ±0.1	54.243 ±0.1 km	28.678 ±0.1 km
1999/04/30	5.3	4.0 ±0.4	53.627 ±0.3 km	27.871 ±0.4 km
unknown	4.7	2.4 ±0.2	57.998 ±0.2 km	27.603 ±0.2 km

Finite fault

Event	M_w	Z(km)	Lon (deg)	Lat (deg)
1997/05/05	5.4	5.6 ±0.4	53.880 ±0.4 km	27.137 ±0.3 km
1997/09/18[a]	4.9	3.5 ±0.2	53.943 ±0.2 km	27.097 ±0.2 km
1998/10/01	4.5	1.1 ±0.1	54.243 ±0.1 km	28.678 ±0.1 km
1999/04/30	5.3	3.3 ±0.4	53.625 ±0.3 km	27.870 ±0.4 km
Unknown	4.7	2.3 ±0.2	57.998 ±0.2 km	27.603 ±0.2 km

Table 3.2: Inversion results: Source parameters for best-fit point sources and finite fault patches for each event in Figures 3.4-3.7. Error bounds on map view locations are also indicated in Figures 3.4-3.7. Superscripts as in Figure 3.1. Location is to center of fault plane.

3.4 Conclusions

The work presented in this chapter is a first step toward the creation of a geodetically-derived earthquake catalog that complements the existing seismic studies of the Zagros mountains. Precise earthquake locations such as these can be inputs into tomography models or tectonic studies that have previously been limited by our knowledge of the distribution of seismicity. Southern Iran provides an ideal candidate for an InSAR-derived catalog, as it has a high level of seismicity and a relatively sparse seismic station coverage. However, the work presented here was seriously limited by the SAR data coverage in Southern Iran. In most cases, the interferogram time periods were so long that it was not possible to associate observed deformation with a specific earthquake, or to distinguish earthquakes that occurred in clusters (e.g., Figure 3.5). A dedicated satellite system providing increased data coverage would greatly facilitate this type of study.

The locations and confidence intervals presented here do not account for variations in local elastic structure that may bias the inferred location. From the results

in Chapter 2, I expect that the main effect of rheological differences is to move the apparent depth up or down by $\sim 10\%$. Another consideration is that the interferograms may include some non-coseismic deformation, such as postseismic slip that propagates updip from the epicenter. Also, in most of the cases shown here, the data was not fit completely by a point source or single fault patch. Because these events are so shallow, they may warrant inversions allowing for distributed slip in order to more completely characterize the earthquake. Nevertheless, the earthquake locations presented here are evidence that some of the shortening within the 10-15 km thick sedimentary section in the Zagros mountains is accommodated seismically by shallow earthquakes of magnitudes $M_w > 4.5$. A more complete catalog of accurate seismic locations would help us determine how strain is being accommodated within this zone of continental convergence.

InSAR provides a fast and straightforward method for augmenting the existing earthquake catalogs. We are currently unable to create a complete catalog, due to the limited spatial and temporal coverage of current SAR data, and we will not be able to detect small or deep earthquakes due to the noise level in typical interferograms. Given the noise levels we observe in interferograms for Southern Iran, we can expect to detect M_w 4 and 5 earthquakes that are shallower than around 5 km and 15 km, respectively, whenever the interferograms are otherwise of good quality (i.e., good correlation and limited topographic artifacts). When multiple interferograms are available that span the same event, we can stack the data to reduce the signal to noise ratio. The InSAR locations that we do find can be used to help calibrate seismic models for the region, which will help seismologists determine if earthquakes that are too small and deep to resolve with InSAR truly occur in the basement.

Chapter 4

Distributed slip Inversions, ${}_j\mathcal{R}_i$ method

Submitted to Blackwell Publishing Ltd. in *Geophysical Journal International* by R. B. Lohman and M. Simons

Abstract

We explore two variations on traditional least-squares inversions for the spatial distribution of subsurface fault slip from geodetic observations of surface deformation. This discrete inverse problem is ill-posed with poorly defined numerical rank. First, we introduce a flexible definition of model complexity where we weight the smoothness of the slip model over the fault plane according to an *a priori* measure of model resolution. Our "variable-smoothing" method allows us access to potential slip models that are inaccessible to inversions using traditional roughness penalties. Second, we introduce a parameter-choice technique we call the ${}_j\mathcal{R}_i$-criterion. The ${}_j\mathcal{R}_i$-criterion is similar to cross-validation and bootstrap methods. We examine the theoretical basis of such techniques and present analytical approximations that can be applied to real problems.

4.1 Overview

We invert geodetic data for coseismic slip on a fault plane to understand how earthquakes interact with each other, how seismic moment release is distributed with depth, how spatial irregularities in fault geometry affect coseismic slip, where and over what time scales postseismic deformation occurs, and what the observed postseismic deformation implies about the rheological structure of the earth. Robust answers to any of these questions require both an estimate of the best-fitting coseismic slip distribution and accurate measures of the error and model covariances associated with that estimate. With the advent of GPS and Interferometric Synthetic Aperture Radar (InSAR), we can obtain a nearly complete description of the displacement of the Earth's surface in response to a given earthquake (e.g., *Fialko et al.*, 2001). These developments encourage us to invert for coseismic slip on fault planes with progressively higher degrees of freedom, and to expand the range of questions that we address about the seismic cycle.

The regularization and interpretation of inversions for fault slip from geodetic data have been examined in detail over the last several decades (e.g., *Segall and Harris*, 1987; *Ward and Valensie*, 1989; *Barrientos and Ward*, 1990; *Freymueller et al.*, 1994; *Pritchard et al.*, 2002; *Simons et al.*, 2002). We review the traditional assumptions made in these inversion and introduce a spatially-variable regularization technique involving two refinements on previous methods: 1) We introduce the idea that the roughness of a slip model does not necessarily have to be defined simply as the average roughness over the fault plane. We explore a method where we weight the degree of smoothing imposed on the solution by a "smoothing shape" function that varies across the fault plane. The inversion can choose from a larger suite of slip models than if we restrict ourselves to the standard model roughness approach. Given the infinite set of possible smoothing shape functions, we explore the behavior of a particular family of functions derived from *a priori* measures of model resolution. These smoothing shapes impose more damping in regions of the fault plane that are poorly resolved by the data and less damping in regions that are well-resolved. 2) Out

of this family of smoothing shapes, we select an optimal shape and a weighting value for the regularization using a parameter choice technique we call the ${}_j\mathcal{R}_i$-criterion (pronounced "jury").

We present our technique within a simplified system of an elastic half-space, a known fault plane geometry, and a single deformation event. We illustrate the behavior of the inversion approach using this synthetic system, where we define the input slip distribution and impose noise of a known character. We also explore scenarios where we have imperfect knowledge of the fault plane geometry, or where we impose positivity constraints on the fault slip. We conclude with an illustration of the use of our method in a subduction-zone setting where we have incorrect *a priori* knowledge about the noise covariance matrix.

4.2 Introduction

The relationship between fault slip and surface displacements can generally be described by a Fredholm integral equation of the first kind:

$$\int_{\Omega} G(\Omega, \Phi) m(\Omega)\, d\Omega = d(\Phi) \tag{4.1}$$

where Ω corresponds to the (x, y, z) coordinates of the fault plane, G is the elastic response of the earth, m is coseismic slip, d are displacements that we measure at the Earth's surface at observation points $\Phi(x, y)$, and (x, y, z) are spatial coordinates. When we use k data points and discretize the fault plane in terms of l fault patches, Equation 4.1 becomes (in matrix form):

$$Gm = d \tag{4.2}$$

where G is a $k \times l$ matrix of Green's functions. We normalize the data using C_d, the data covariance matrix, as described in Appendix A.1 (e.g., *Harris and Segall*, 1987). This normalization allows us to combine data with different noise characteristics, such as GPS and InSAR observations. The integration with G in Equation 4.1 damps out

high-frequency components of $m(\Omega)$ in the forward problem, and tends to amplify whatever noise exists in the data in the reverse procedure, that of computing $m(\Omega)$ from $d(\Phi)$ (e.g., *Menke*, 1989; *Hansen*, 1998). As our fault parameterizations become finer and allow for more model complexity, inversions for slip become increasingly poorly determined, with noise in the data mapping into wildly varying, unrealistic oscillations that increase with depth. Therefore, we must penalize models that have unrealistic characteristics by regularizing our inversions.

The inherent instability in these inversions does not merely stem from having fewer data points than unknowns, although this situation will certainly exacerbate the problem. With the advent of InSAR data, we will generally have many more data points than unknowns. In the absence of noise and round-off errors, and where we know the exact model geometry, we could invert perfectly for a continuous model of fault slip on a fault plane that extended to arbitrarily great depth. Unregularized inversions of real data often result in models with alternating patches of positive and negative slip that nearly cancel out at the surface, an effect known as "checkerboarding." The checkerboarding effect stems from the magnification of noise, i.e., from the inability of the inversion to distinguish between slip on two adjacent patches to within the level of noise, or to within the available numerical precision. In general, this effect will increase with distance of the fault patches from the data points, and with decreasing size of the fault patches.

Because of the inherent non-uniqueness of geodetic inversions, we never aim to fit the data exactly, or to model the entire continuous slip distribution on a given fault plane. The manner in which inversion methods attempt to deal with this non-uniqueness generally fall into two main categories that affect the inversion in similar ways. The first approach involves defining the output model as a sum of intelligently chosen basis functions that are well-resolved by the available data set. Parameterizing the inferred slip distribution as a single fault patch that is an average over the continuous slip distribution is the simplest case, but will not generally produce a good fit to the data, nor will we learn much about the earthquake. Another approach is to divide the fault plane into variably-sized fault patches, with the size of the fault patch

varying according to the resolution over the fault plane (*Sagiya and Thatcher*, 1999; *Pritchard et al.*, 2002; *Simons et al.*, 2002). Alternately, one can choose non-boxcar basis functions like splines or wavelets to describe the slip distribution (e.g., *Yabuki and Matsu'ura*, 1992).

The second category of inversion methods also involves a choice of basis functions, in a less explicit manner. These methods involve considering some penalty function that quantifies whether or not a model is physically realistic, and minimizing some combination of this model penalty and its ability to fit the data:

$$\Gamma = ||Gm - d|| + \lambda ||f(\Omega, m)|| \tag{4.3}$$

or

$$\Gamma = E_d + \lambda E_p \tag{4.4}$$

where Γ is the objective function that we minimize, $E_d = ||Gm - d||$ is the norm of the data residual, $f(\Omega, m)$ is the penalty function, $E_p = ||f(\Omega, m)||$ is the penalty function, and λ is a relative weighting constant, also known as a "penalty parameter". These inversions fall into two main families, nonlinear and linear inversions. In nonlinear inversions, a range of possible models is sampled and characterized in terms of data misfit, E_d and penalty error, E_p. Given this broad knowledge of the model space (model hyperparameters), one can compute the covariance between model hyperparameters, best fit slip distribution and errors on quantities like total moment or the profile of slip vs. depth. Nonlinear inversions allow the implementation of any conceivable penalty function or *a priori* information, such as bounds on slip, spatial compactness or roughness, or positivity constraints (e.g., *Barrientos and Ward*, 1990; *Du et al.*, 1992). However, nonlinear methods are generally expensive and interpretation of the covariances from the total ensemble of attempted models can be difficult, especially as the number of fault patches becomes large. As the computational burden becomes tractable and methods for assessing the sampled ensemble of models continue to improve (e.g., *Sambridge*, 1998b), nonlinear methods may become the preferred techniques for slip inversions. If we were to use a Bayesian viewpoint (e.g.,

Tarantola and Valette, 1982a,b), our *a priori* probability distribution on the model would describe the imposed penalty function, and the solution to the inverse problem would be the posterior probability distribution on the set of inferred parameters.

Linear least-squares methods require a linear penalty function such that $f(\Omega, m) = f(\Omega)$. Linear inversions have the convenient property of producing model and data covariance and resolution matrices that we can use to assess the significance of the output slip model. Common linear techniques for slip inversions include damped least-squares (e.g., *Ward and Valensie*, 1989; *Du et al.*, 1992; *Matthews and Segall*, 1993), truncation of the SVD eigenvectors (e.g., *Segall and Harris*, 1987; *Harris and Segall*, 1987; *Menke*, 1989; *Larsen et al.*, 1992), and constraints based on various measures of solution length or roughness, such as a Laplacian approximation of the 2nd order derivative (e.g., *Du et al.*, 1992; *Árnadóttir and Segall*, 1994; *Freymueller et al.*, 1994; *Simons et al.*, 2002). All least-squares linear inversions define a set of solution modes, or model basis functions. The complexity of the basis functions that the inversion allows depends on the choice of λ.

The effect of λ can be seen if we map every possible slip model onto a plot of E_p *vs.* E_d that illustrates the tradeoff between E_p and E_d (Fig. 4.1). The entire ensemble of possible models defines a space that is bounded on the lower left by a subset of models that form a curve commonly referred to as the "L-curve". Each point on the L-curve corresponds to a model extracted by the linear least-squares inversion for this definition of $f(\Omega)$ and a particular choice of λ. When $f(\Omega)$ is a measure of model roughness, then the L-curve corresponds to a trade-off curve between data fit and model complexity. The "best" model is often defined as one that balances model complexity and data fit (e.g., *Menke*, 1989), and is generally chosen at the "corner" of the L-curve (Fig. 4.1). Different definitions of $f(\Omega)$ will result in a different set of models that are accessible to the linear inversion, and potentially a different shape and corner-value of the L-curve (Fig. 4.1). The *a priori* choice of a regularization technique such as minimizing solution roughness or the SVD method fixes $f(\Omega)$ and leaves the choice of λ (or the SVD truncation value, p) as the only degree of freedom in the inversion. Popular techniques for choosing λ include choosing the corner of the

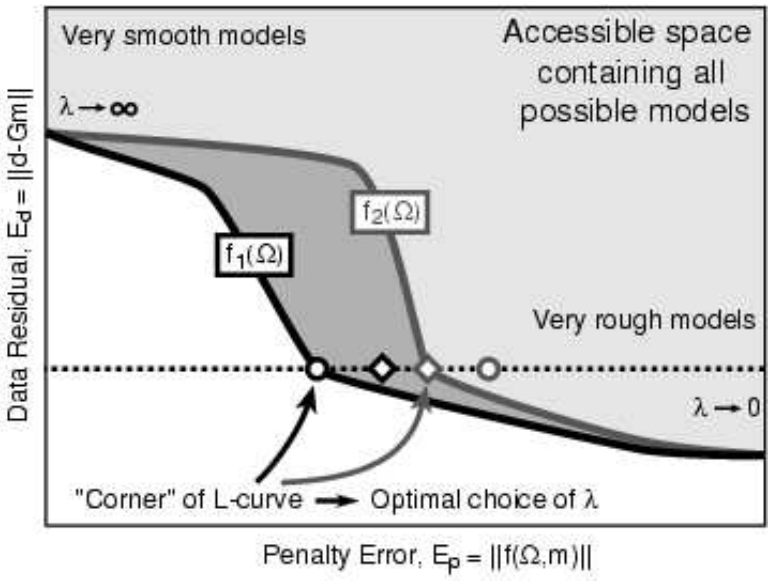

Figure 4.1: Schematic diagram illustrating how all possible models fall somewhere on a graph of their fit to the data vs. potential penalty functions. We show two theoretical penalty functions, with their respective L-curves indicated by the black ($f_1(\Omega)$) and gray ($f_2(\Omega)$) heavy lines. In each case, no possible combinations of fault slip exist that would fall to the lower left of the L-curves. The value of λ fixes the location along the L-curve. Circles and diamonds indicate two different slip distributions that have the same fit to the data, E_d. Black symbols indicate the penalty value of these slip distributions as assessed by $f_1(\Omega)$, and the gray symbols correspond to the penalty associated with $f_2(\Omega)$. When we use $f_1(\Omega)$, the circle model is accessible to a linear inversion but the diamond is not. For $f_2(\Omega)$, the reverse is true.

L-curve (e.g., *Segall and Harris*, 1987), cross-validation (e.g., *Árnadóttir and Segall*, 1994; *Freymueller et al.*, 1994; *Cervelli et al.*, 2001; *Hreinsdottir et al.*, 2003), and the Akaike Bayesian Information Criterion (e.g., *Akaike*, 1980; *Jackson and Matsú'ura*, 1985; *Ide et al.*, 1996). In this paper, we examine a range of $f(\Omega)$ and present a parameter-choice technique that simultaneously chooses from among a suite of $f(\Omega)$ and λ.

We introduce "variable-smoothing" as an alternative to regularizations that fix $f(\Omega)$ to be the average roughness of the inferred model. In variable-smoothing, we explore the behavior of a particular family of penalty functions that are spatially weighted versions of a roughness penalty. We weight the contribution of the spatial roughness of each fault patch to the total penalty, E_p, by an *a priori* measure of resolution at that particular patch. We use the SVD method to derive our measure

of *a priori* resolution with various values of the truncation parameter, p. We could easily use other functions to weight our roughness penalty, such as a linear ramp, step functions, etc., but we find that these smoothing shapes do not extract models that improve on our SVD-based smoothing shape.

We introduce ${}_j\mathcal{R}_i$, a parameter-choice technique based on the idea that models derived from independent datasets should fit that part of the data that all datasets have in common (i.e., the underlying geodetic signal) without introducing model characteristics that are merely fitting the noise. We penalize rough slip models because they do not fit this underlying signal, not because of an explicit consideration of their spatial complexity as one would do with the L-curve method. We describe the theoretical basis for this technique in the special case where we know both the input signal and the character of the noise, and we explore two approximation techniques that can be applied to real scenarios.

4.3 Implementation

To acquaint the reader with the terminology we use, we briefly describe the geometry of the idealized synthetic problems we consider in this paper (Section 4.3.1). Next, we define the family of $f(\Omega)$ that we explore using variable smoothing and comment on how the variation of $f(\Omega)$ can affect properties of the inferred slip distribution (Section 4.3.2). In Section 4.3.3 we describe ${}_j\mathcal{R}_i$, our technique for choosing the best values for $f(\Omega)$, λ, or other inversion tuning parameters in these synthetic systems. We end Section 4.3 with a description of how we adapt this technique to realistic inversion situations.

4.3.1 Configuration of synthetic problem

We consider vertical fault planes with purely left-lateral strike-slip motion in a homogeneous elastic half-space (*Okada*, 1985). For illustration, we examine both 1-D and 2-D systems. The 1-D system involves observations of along-strike deformation along a data profile perpendicular to an infinite fault with a slip distribution varying only

with depth (Fig. 4.2). We use an input slip distribution that varies at several spatial scales and contains peaks in slip at 7 and 13 km. It is simpler to illustrate changes in model error and data fit due to our choice of regularization parameters with this 1-D system than for the 2-D system. However, given that there is only one component of the deformation field, the achievable model resolution is much lower than it would be in a real scenario. For a more realistic 2-D system, we consider a fault plane with an input slip distribution that varies both along-strike and down-dip (Fig. 4.3a). We use observations covering only the northern half of the deformation field (Fig. 4.3b), in order to simulate a realistic scenario where we have incomplete data coverage. The data noise is normally distributed with variance σ^2 and zero mean. For the 2-D system, we examine inversions using observations of one, two or three components of the 3-D deformation field.

4.3.2 Variable smoothing and $f(\Omega)$

In variable-smoothing, we seek to apply more smoothing where the model is poorly resolved and little to no smoothing where the model is well-resolved. To this end, we search a family of $f(\Omega)$ that are all weighted model roughness penalties. For the "constant smoothing" case, $f(\Omega) = D$, where D is the finite difference approximation to the 2nd order Laplacian smoothing matrix. For "variable smoothing", we define a diagonal smoothing shape matrix, S, that weights each row of D, such that $E_p = ||SDm||$ (Fig. 4.4). We find the model that satisfies Equation 4.3 using a generalized inverse, $G^{-g} = (G_a^T G_a)^{-1} G^T$ and $m_{est} = G^{-g} d_a$, where the augmented Green's function, $G_a = [G \;\; \lambda SD]^T$ and $d_a = [d \;\; 0]^T$, and m_{est} is the output model inferred by the inversion. We construct S from the resolution matrix, R^0, derived from SVD truncation with truncation value, p (Appendix A.2). The value of S_{ii} for the i^{th} fault patch is $\sqrt{1 - R^0_{ii}}$. Thus, when a fault patch is perfectly resolved, $R^0_{ii} = 1$, and S_{ii} will be 0. When a fault patch is poorly resolved, R^0_{ii} will be a small number and S will be close to 1. We define p=0 as the "constant smoothing" case, where D=I, the identity matrix.

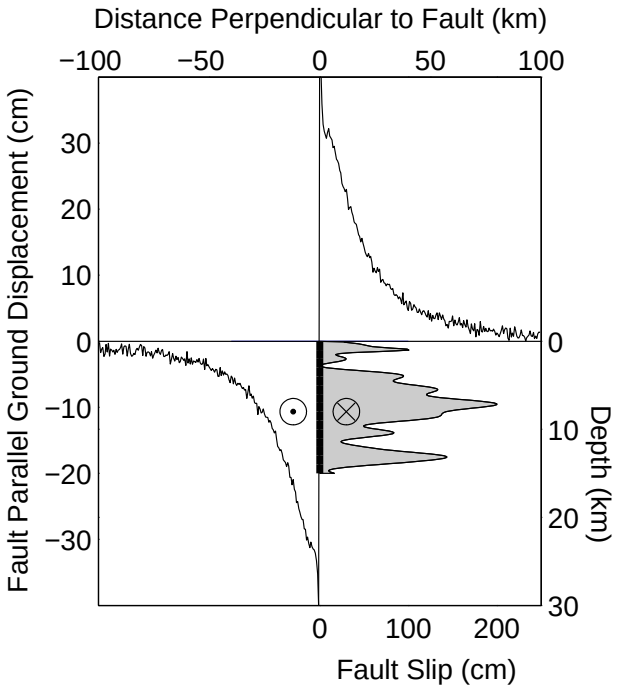

Figure 4.2: The fault plane we use in the 1-D system (heavy line) extends infinitely along strike and to 15 km depth. We subdivide the fault plane into equally sized patches, and impose a purely left-lateral input slip distribution (shaded region). We calculate synthetic data along a line of points running perpendicular to the fault, adding Gaussian noise with zero mean and variance σ^2 (thin line). In this example, σ=0.5 cm and downdip patch width=0.1 km. Since the fault has infinite length, fault-perpendicular and vertical components of deformation are zero.

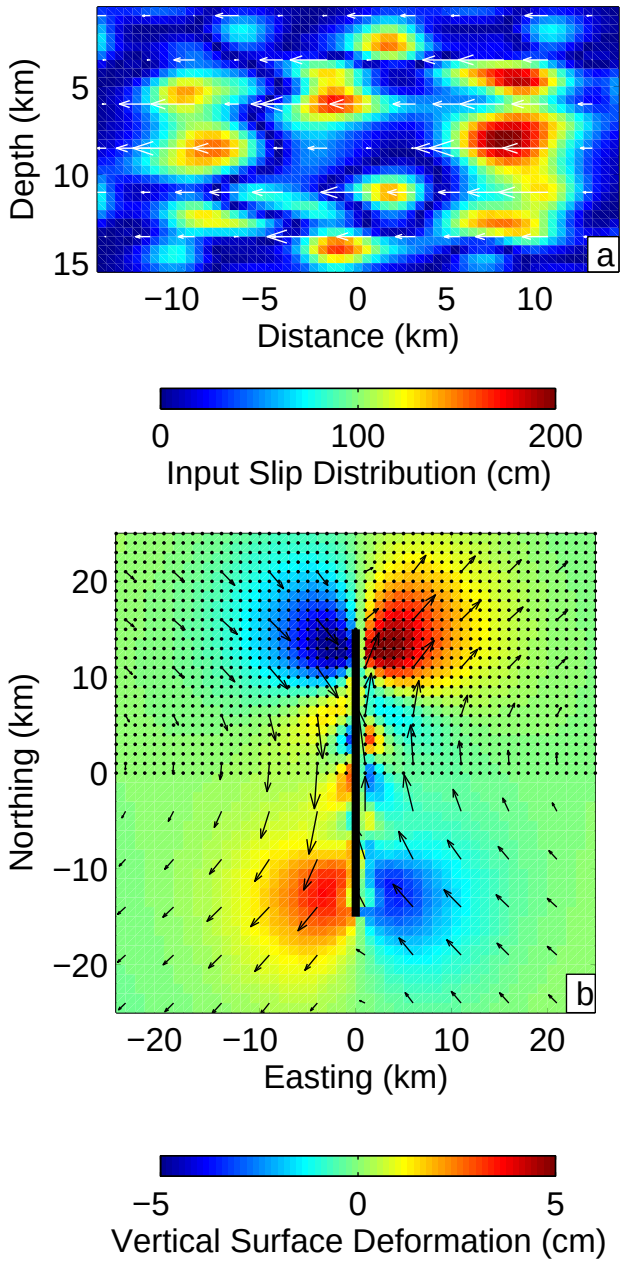

Figure 4.3: Our vertical 2-D fault plane extends to 15 km depth and 25 km along strike. a: Input left-lateral slip distribution has multiple peaks with magnitudes around 200 cm, varying at several length scales. b: Map view with fault trace (heavy line), vertical deformation field (color) and horizontal deformation field (arrows) due to the slip distribution in panel (a). Maximum horizontal deformation is 20 cm. We examine the effects of having a data distribution that only covers half of the region (small dots)

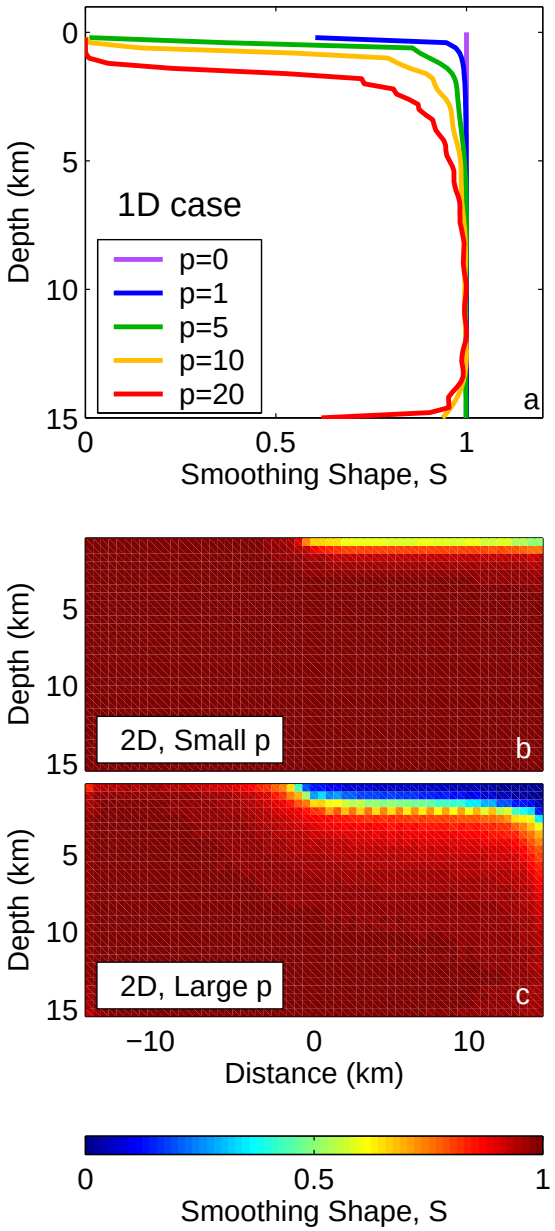

Figure 4.4: Examples of smoothing shape, S, for the 1-D and 2-D systems, a: S calculated for 1-D case for several values of the SVD truncation value, p. Note that p=0 corresponds to the constant-smoothing case and that S does not always go to zero at the surface. 2-D system: S calculated for small (b) and large (c) values of p, with solution constrained to purely strike-slip. The left half of the slip distribution, where there is no data, is smoothed more than the right half. If we used a uniform data distribution, S would be approximately constant along strike. For p=0, S=I over the entire fault plane. When we allow dip-slip motion, S will be different for the strike-slip and dip-slip components.

When we vary $f(\Omega)$, we allow our models to have different distributions of complexity and resolution over the fault plane than are accessible with constant smoothing (p=0) inversions. In the constant smoothing case, the fit to the data trades off with the spatial roughness averaged over the entire fault plane. In order to fit the data near the fault, the inversion must choose a slip distribution that is somewhat similar to the input slip distribution, m_0, near the surface, where the slip distribution has the largest effect on the synthetic data. However, the choice of λ that allows this fit may result in large oscillations in the model at depth, increasing the average spatial roughness and forcing the inversion toward larger values of λ. An optimal choice of $f(\Omega)$ may be slightly undamped at shallow depths and allow the model to fit data close to the fault without introducing large model error at depth.

Any choice of inversion parameters defines the resolution and model covariance of our inferred model. Whenever we apply non-zero smoothing to a linear least-squares inversion, our model estimate becomes a spatial average over the true continuous slip distribution, with the spatial averaging scale increasing as λ becomes large. The extent to which the inferred slip at any given patch is an average over the surrounding patches can be assessed by inspecting the rows of the final model resolution matrix, R (e.g., *Menke*, 1989). For practical purposes, we construct a measure of spatial averaging scale, W, which we define as the width of the row of R associated with each fault patch. Details of how we compute the width of each row are in Appendix A.2. For a 2-D fault plane, we define W as the root mean square (RMS) of the smoothing scales in the along-strike and down-dip directions. W is an *a posteriori* quantity that we use to compactly illustrate the effects of data noise, system geometries, etc. on our synthetic inversions. Model resolution generally does not take the form of a compact peak centered on each fault patch, but tends to include contributions from regions all over the fault plane (Fig. 4.5). Therefore, our W is only an approximate measure of the averaging scale for each fault patch in the inversion. Any rigorous assessment of the significance of features in the final model should always involve examining R directly.

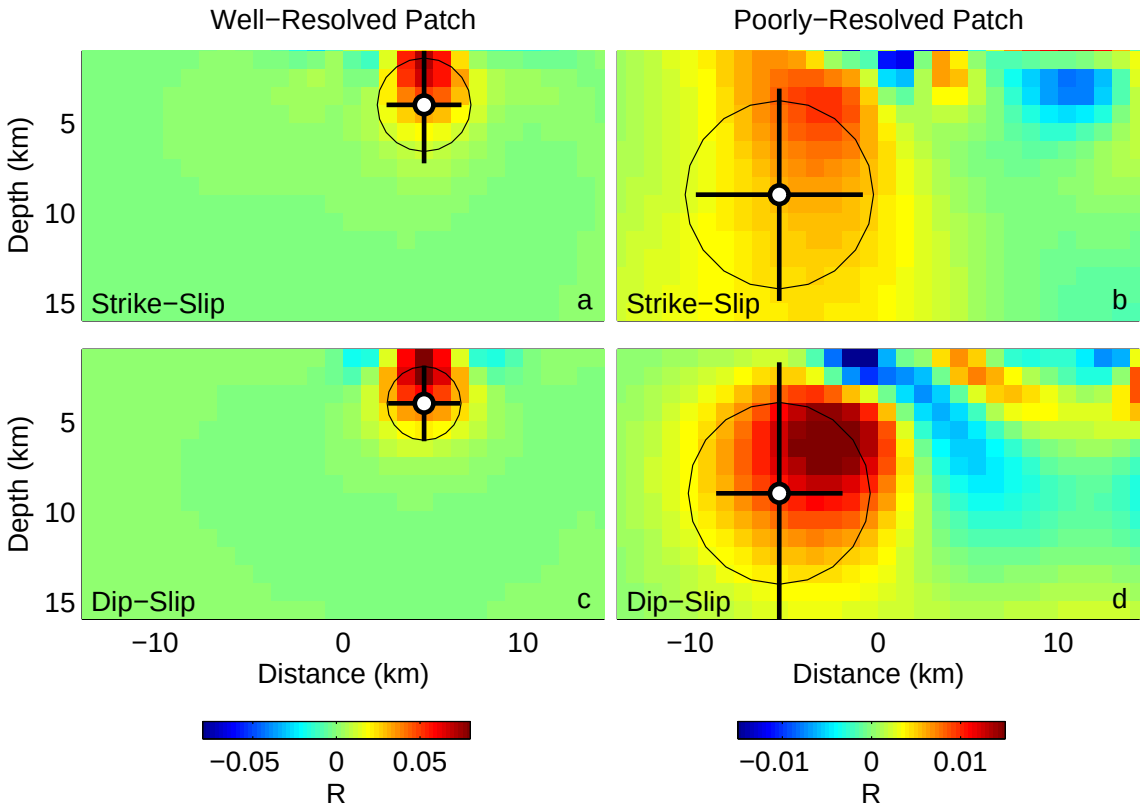

Figure 4.5: Rows of R associated with two fault patches with different degrees of resolution. Upper panels correspond to the mapping of strike-slip offset across the entire fault plane onto strike-slip offset on the patch indicated by the open circle. Low panels correspond to dip-slip offset. There are corresponding maps between strike-slip and dip-slip offsets, but these tend to be lower amplitude and are not considered here. Bars indicate the variance in the horizontal and vertical directions (W_h, W_v), with a circle of width W, where W is the RMS of W_h and W_v. All fault parameters are the same as in Figure 4.11.

4.3.3 Choice of (p, λ)

In our synthetic cases, we investigate the interaction between the inversion procedure, input slip model, m_0, and the observed data. We define a "good" regularization as one that fits the underlying signal (d_0) as well as possible without introducing model characteristics that are merely fitting the noise. Increasing λ decreases our ability to fit the underlying signal, as the inferred model is forced to be increasingly smooth. We call the error due to over-smoothing the regularization error, since it is a function of our regularization method and the input slip distribution, not of the noise (e.g., *Hansen*, 1998). As we decrease λ, the inferred model fits more and more of the noise, resulting in an increase in what we will we call the perturbation error. The total error for a given λ is the sum of the perturbation and regularization errors. Note that these quantities are not the same as the E_d and E_p from Equation 4.4. We are not penalizing a model for its roughness directly (E_p), but for the roughness of the synthetic data it predicts.

To quantify and separate the regularization and perturbation errors, we rely on the fact that we can treat our observed data, d_i, as a sum of two parts:

$$d_i(\Phi) \equiv d_0(\Phi) + n_i(\Phi) \tag{4.5}$$

where d_0 is the elastic response of the earth to an input slip distribution (m_0) in the absence of noise, and the n_i are multiple realizations of independent, identically distributed Gaussian noise with variance σ^2 and zero mean. We drop the explicit use of the spatial coordinate Φ for the remainder of this paper. In this section we find the optimal regularization assuming that we know d_0. In Section 4.3.4 we describe ways to separate d_0 from d_i. Since the forward and inverse problems are linear, we can separate each inversion into the parts controlled by the exact data and by the noise.

4.3.3.1 Exact data

We quantify the regularization error by the amount that the predicted synthetics are smoothed by a particular inversion. Given $d_0 = Gm_0$, we infer slip distributions from d_0:

$$m_0^* = G^{g*} d_0 \tag{4.6}$$

$$d_0^* = G m_0^* \tag{4.7}$$

where G^{g*} is the generalized inverse for a regularized inversion with a given (p, λ), m_0^* is the smoothed version of m_0 that we would infer with a particular regularization, and d_0^* is the smoothed surface deformation predicted by m_0^*. In general we use the asterisk to signify inversion quantities where we have applied smoothing. If our forward model is exact (e.g. correct fault geometry, elastic parameters, no round-off errors, etc.), then when $\lambda = 0$, $m_0^* = m_0$ and $d_0^* = d_0$. We define the regularization error as the difference between our noise-free data (d_0) and the deformation predicted by the smoothed model (d_0^*):

$$_0r_0 \equiv d_0 - d_0^* \tag{4.8}$$

where $_0r_0$ is the regularization error. We can also write Equations 4.6-4.8 as:

$$m_0^* = R m_0 \tag{4.9}$$

$$d_0^* = N d_0 \tag{4.10}$$

$$_0r_0 = [I - N]\, d_0 \tag{4.11}$$

where $R = G^{g*}G$ and $N = GG^{g*}$ are the model and data resolution matrices, respectively (e.g., *Menke*, 1989).

4.3.3.2 Noise

The perturbation error is the degree to which a given realization of the noise in the data, n_i, is mapped by the inversion into the inferred slip, $m_{est} = m_i^*$, and back into

our predicted synthetic data, d_i^*.

$$m_i^* = G^{g*} d_i \tag{4.12}$$

$$d_i^* = G m_i^* \tag{4.13}$$

We separate the operation of G^{g*} on the noisy data into a sum of its parts:

$$m_i^* = G^{g*} d_0 + G^{g*} n_i \tag{4.14}$$

$$d_i^* = d_0^* + n_i^* \tag{4.15}$$

where

$$n_i^* = N n_i \tag{4.16}$$

is the noise filtered by our regularization. We define:

$${}_i r_i^n \equiv n_i - n_i^* \tag{4.17}$$

${}_i r_i^n$ represents the smoothing of the noise by the inversion which decreases with decreasing λ. We can also compare a smoothed set of noise with a completely independent realization of the noise:

$${}_j r_i^n \equiv n_j - n_i^* \tag{4.18}$$

This quantity, which we define as the perturbation error, increases as λ decreases. The total error when we compute a residual between one data set and a smoothed, independent data set is

$${}_j r_i \equiv d_j - d_i^* \tag{4.19}$$

Combining Equations 4.8 and 4.19, we get

$${}_j r_i = {}_0 r_0 + {}_j r_i^n \tag{4.20}$$

indicating that the total error is equivalent to the sum of the perturbation and regularization errors (Fig. 4.6a). We define measures of the size of these residuals as

$$ {}_0\mathcal{R}_0 \equiv \frac{1}{k} \sum_{\Phi} {}_0 r_0^2(\Phi) \tag{4.21} $$

$$ {}_j\mathcal{R}_i \equiv \frac{1}{k} \sum_{\Phi} {}_j r_i^2(\Phi) \tag{4.22} $$

where k is the number of observation points used in the inversion. As λ approaches 0, the perturbation error approaches 2σ and the regularization error approaches 0. We use a script $\mathcal{R}$ to avoid confusion with R, the resolution matrix. As λ becomes large and smoothing increases, the perturbation error decreases and the regularization error increases. Note that the total error quantifies the regularization error and perturbation error as they express themselves at the surface observation points, and that the spatial discretization of the fault plane will introduce an additional error in a real scenario.

4.3.3.3 Parameter choice

If our goal is to maximize the fit to the underlying signal, we must choose the values of λ and p that minimize the total error. The ideal regularization would predict a model d_i^* from each dataset d_i that had the lowest residual when compared to all other datasets d_j. This is equivalent to minimizing ${}_j\mathcal{R}_i$, and is the point where we stop introducing model features that are merely fitting the noise. Note that our minimization of ${}_j\mathcal{R}_i$ is different from the minimization of the objective function, Γ, in Equations 4.3 and 4.4. Our choice of (p, λ) fixes the form of the Γ that we minimize in the inversion for m_i^*.

One way to calculate the theoretically best value of λ for a synthetic system would be to create a large number of synthetic datasets with different realizations of the noise, and to calculate ${}_j\mathcal{R}_i$ numerically by computing all the permutations of $d_j - d_i^*$. However, we can be more efficient in these synthetic cases and capitalize on the fact that we know the input model, m_0, and the covariance structure of the noise.

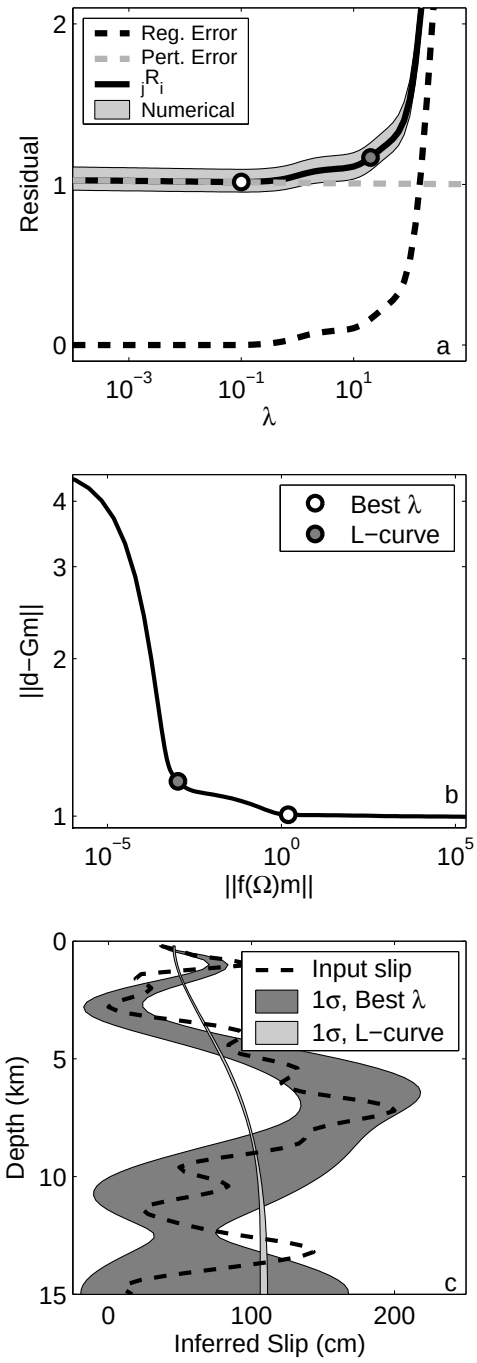

Figure 4.6: a: Regularization and perturbation errors, and their relation to ${}_j\mathcal{R}_i$ as a function of λ. Shaded region indicates 1σ numerical bounds on ${}_j\mathcal{R}_i$. b: Sample L-curve showing the value of λ chosen by the ${}_j\mathcal{R}_i$-criterion (open circle) and the value chosen by visual inspection of the L-curve (shaded circle), on a plot of model roughness *vs.* data fit. c: Input slip distribution, m_0, and upper and lower 1σ confidence intervals for the two slip distributions from (a,b). In this case there was a misleading corner on the L-curve that would lead to an oversmoothed inferred model with small error bounds but a large averaging scale.

We can use these two quantities to find the value of ${}_j\mathcal{R}_i$ analytically for any (p, λ).

Earlier, we noted that we can express Equation 4.8 as ${}_0r_0 = [I \quad -N]\, d_0$. If we define a matrix M as $[I \quad -N]$, then we can express the residual quantities as:

$$ {}_0r_0 = M[d_0 \quad d_0]^T \tag{4.23} $$

$$ {}_jr_i = M[d_j \quad d_i]^T \tag{4.24} $$

$$ {}_jr_i^n = M[n_j \quad n_i]^T \tag{4.25} $$

if C_d is the data covariance matrix, then by the law of covariance propagation:

$$ C_r = MC_dM^T \tag{4.26} $$

where C_r is the covariance matrix of ${}_jr_i^n$. We can derive (Appendix A.3):

$$ {}_j\mathcal{R}_i = {}_0\mathcal{R}_0 + \frac{1}{k}\sum diag(C_r) \tag{4.27} $$

This quantity depends only on the input model and on the noise covariance, and quantifies the total error. We can perform a grid search through values of (p, λ) and choose the optimal parameter combination for any synthetic system that interests us. This optimal regularization will be the closest that d_i^* can get to d_0 for a given noise level.

The superiority of the ${}_j\mathcal{R}_i$-criterion over the L-curve method is illustrated in Figs 4.6b and c. L-curves often have multiple "corners", and the value of λ that we choose for the p=0 case using our method often differs than the λ that we would choose by visual inspection of the L-curve. The ${}_j\mathcal{R}_i$-criterion bears some similarity to the cross-validation technique used by *Árnadóttir and Segall* (1994) (see next section), who also find that the corner of the L-curve does not always indicate the optimal value of λ. The approach described here has the additional advantage, via the choice of p, that it can explore a family of $f(\Omega)$.

We note that our "optimal" (p, λ), which satisfies the ${}_j\mathcal{R}_i$ criteria, is not necessarily

the best choice for every problem. Each choice of (p, λ) corresponds to a different model covariance matrix and averaging scale for the solution. Scenarios may exist where we require an increased level of confidence relative to that we would choose with ${}_j\mathcal{R}_i$. In these cases, one must be able to tolerate a higher degree of spatial averaging.

4.3.4 Real Data

${}_j\mathcal{R}_i$ as defined in Equation 4.27 is our "theoretical" derivation, or ${}_j\mathcal{R}_i^t$. In a real application, we have one set of data and usually only limited information about the real slip distribution or the character of the noise. In other words, we will be unable to compute ${}_0\mathcal{R}_0$ or C_d exactly, and cannot directly choose the best (p, λ) pair. In this case, we have two ways of approximating ${}_j\mathcal{R}_i$. The first method involves assuming C_d and forming an approximation of ${}_0\mathcal{R}_0$ using the existing dataset, d (Derivation in Appendix A.4). We refer to this "approximate" value as ${}_j\mathcal{R}_i^a$.

The second technique relies on Equations 4.19 and 4.22, from which we can approximate ${}_j\mathcal{R}_i$ without knowledge of m_0 or C_d if we have multiple datasets. We attempt to simulate the existence of multiple datasets by resampling our single dataset. Data resampling techniques are all based on the premise that if an inversion is stable with respect to the noise, a model predicted from a subset of the data should fit the remaining data reasonably well (Fig. 4.7). Implementations of data resampling include cross-validation, jackknifing, and the bootstrap (e.g., *Efron and Gong*, 1983). Resampling techniques all share the problem that it is not obvious how to choose the size of the resampled subsets, and require an assumption of uncorrelated noise. Cross-validation has already been used to choose smoothing parameters for slip inversions (e.g., *Árnadóttir and Segall*, 1994; *Freymueller et al.*, 1994; *Cervelli et al.*, 2001; *Hreinsdottir et al.*, 2003). In this study, we create a resampled data set by randomly choosing 50% of the original set. We infer a model from the resampled dataset, then use this model to predict the deformation at points that were not used in the inversion. We refer to the resampled approximation as ${}_j\mathcal{R}_i^r$. We use ${}_j\mathcal{R}_i^r$ in

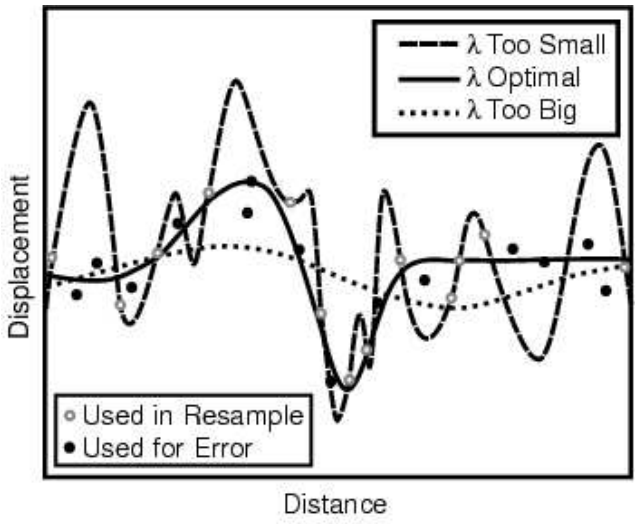

Figure 4.7: Schematic illustration of resampling methods (e.g., bootstrap, cross-validation): Circles indicate data observations of some general process, with open circles indicating data points that were used in a single resample of the total data set. Solid circles indicate data points that were not included in the inversion, but that were used in calculating data error. The three curves correspond to models inverted using the resampled data points for different values of λ. For a very small λ (dashed curve), the inversion matches each resampled data point closely, at the expense of producing a high variance slip model with unrealistic oscillations. The high variance model will have a large misfit with the unused data points (closed circles). This corresponds to the case where regularization error, ${}_0\mathcal{R}_0$, is very small and perturbation error, ${}_j\mathcal{R}_i^n$, is high. For a large value of λ (dotted curve), the inferred model is so smooth that it does not fit any of the data points. The ideal value of λ (solid curve) balances the regularization and perturbation errors and provides the best fit to the underlying signal, d_0.

cases where we have nonlinear constraints and cannot calculate ${}_j\mathcal{R}_i^a$. Where possible, we compare the two approximation techniques as a check on the robustness of our parameter choice.

We examine the behavior of both approximation techniques in a 2-D system by producing a large number of datasets with independent n_i and calculating ${}_j\mathcal{R}_i^a$ and ${}_j\mathcal{R}_i^r$ for each data set (Fig. 4.8a). We fix p=0 here for simplicity, but Fig. 4.8 applies for variable p as well. We find that both methods are sensitive to the specific character of each n_i (i.e., whether it has particularly large values of noise near the fault) and do not always select λ_t, the value we would choose if we knew ${}_j\mathcal{R}_i^t$. The values of λ that the approximation methods select cluster near λ_t, although there is a non-zero chance

of choosing a very large or small λ for a given dataset (Fig. 4.8). The ${}_j\mathcal{R}_i^a$ technique relies on an assumption of C_d, but that assumption can be checked at the end of the inversion. The ${}_j\mathcal{R}_i^r$ technique is independent from assumptions about the noise or input slip distribution, but it is not obvious how to choose subsets of the data. Different percentages of data points in the resamples result in different inferred λ. In addition, we find that the ${}_j\mathcal{R}_i^r$ method requires inversions of hundreds of resamples to converge, and therefore takes hundreds of times as long as the ${}_j\mathcal{R}_i^a$ method. The ${}_j\mathcal{R}_i^a$ method only works for linear penalty functions, so we must use ${}_j\mathcal{R}_i^r$ when we have bounds on fault slip or other nonlinear constraints.

We conclude that for a real application when we have one dataset, we will generally choose a (p, λ) similar to the one we would choose if we knew ${}_j\mathcal{R}_i^t$. Our method will occasionally result in small values of λ (Figure 4.8), but these cases will be obvious due to the extremely high model covariances. We expand on our technique for dealing with real datasets in Section 4.5.

4.4 Behavior of Synthetic Systems

In this section, we use the ${}_j\mathcal{R}_i^t$ technique to examine the behavior of synthetic systems as we vary quantities including noise and fault patch size.

4.4.1 1-D

Although the 1-D system is somewhat unrealistic, we use it to demonstrate the behavior of our inversion recipe. To begin, we create a 1-D fault plane and data geometry as in Figure 4.2, and search through a range of p and λ to find the combination that minimizes ${}_j\mathcal{R}_i$ (Figure 4.9a). We also examine the model we would choose for constant smoothing (p=0, S=I). For each of the two cases, we find the resolution matrix R, the averaging scale W, and the 1σ bounds on best-fitting slip models. The oscillations in W and the model error bounds (Figs 4.9d and e) are consequences of applying smoothing on a finite fault plane and thereby restricting the modes that the solution can take. SVD truncation produces the same effect. We note that W

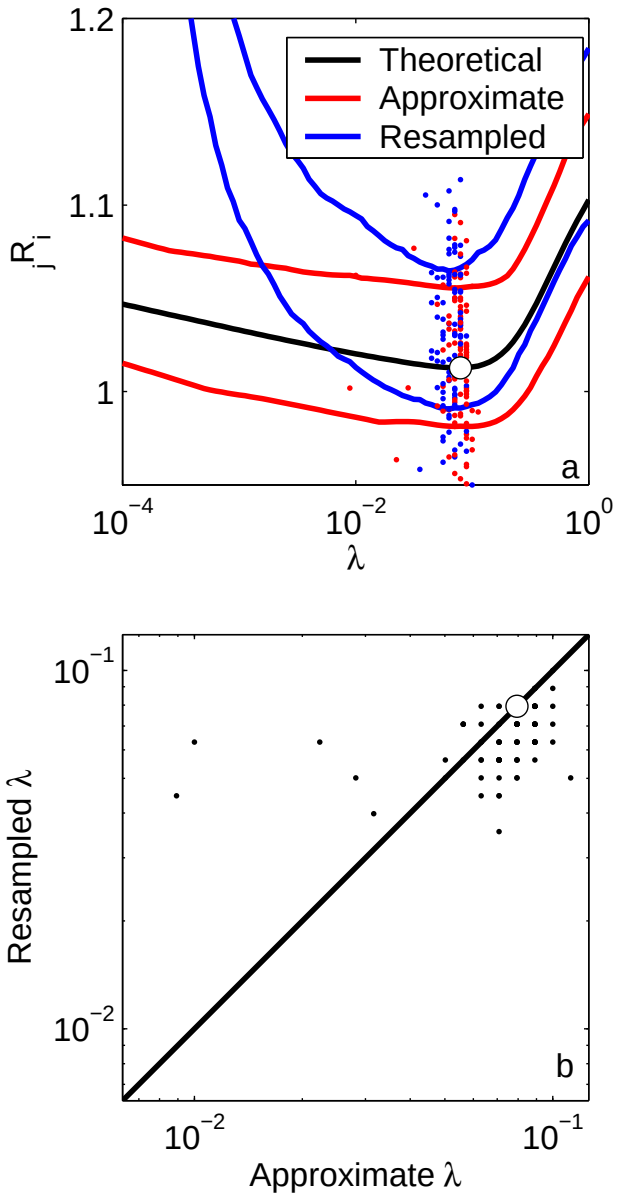

Figure 4.8: Performance of approximations of ${}_j\mathcal{R}_i$ in the 2-D system, for p=0. a: ${}_j\mathcal{R}_i^t$ and 1σ confidence intervals on the approximate (${}_j\mathcal{R}_i^a$) and resampled(${}_j\mathcal{R}_i^r$) estimates. Small dots indicate the values of λ chosen by the two algorithms for 100 independent d_i. The large open circle indicates λ_t, the value chosen by ${}_j\mathcal{R}_i^t$. b: Comparison of λ's chosen by both algorithms for each of the 100 d_i. The ${}_j\mathcal{R}_i^a$ method chooses slightly larger smoothing on average, with a rare occurrence of very low values. Our resampling algorithm used 200 resamples of each d_i, each with 50% of the total number of points.

is larger for the p=8 case over all but the shallowest portion of the fault, but that the model error is significantly lower for p=8 over most of the fault plane. In this case, a better fit to the data is found with a smoother model at depth and slightly more complicated model near the surface. We emphasize here the dramatic decrease in model error (Figure 4.9e) for a moderate increase in W (Figure 4.9d).

As described above and in Appendix A.2, our derivation of W is based on the width of the resolution matrix R around each fault patch. However, as is evident in Figure 4.9c, the rows of R are often non-Gaussian and may have peaks off of the main diagonal. Therefore, we should be cautious about use of W for all but the most qualitative judgments about the model. In Figure 4.9f, we show the result of running a Gaussian curve of width W_i for each fault patch i over the input model m_0 (dashed line), and compare this averaged model with the inferred model. The misfit at around 8 km depth results from a second peak in R at shallow depths (Figure 4.9c) that is not accounted for by our definition of W. Essentially, the slip at great depths covaries with slip at shallow depths, so that the estimate of slip at a given depth can include "leakage" from remote areas of the fault plane. We assess the degree of leakage by direct inspection of R.

We explore the sensitivity of the 1-D system to variations in fault patch size, data noise and the size of a data gap near the fault (Figure 4.10). We choose the best value of (p, λ) theoretically, with ${}_j\mathcal{R}_i$. In each case, the inferred slip in the left column is m_0^*, the smoothed version of m_0. The inferred model for a specific realization of the noise, m_i^*, should fall near m_0^*, within the models 1σ error bounds (right column). For the patch size test, we created input data using 0.1 km fault patches, and inverted this data using progressively larger fault patches. Note that our inferred models, W, and the model error are independent of fault patch size until the fault patches get much larger than the inherent resolution of the problem (Figure 4.10b). If we ensure that our fault patches are smaller than the averaging scale, we avoid the implicit regularization that occurs when we use an excessively coarse parameterization. As expected, the inversion responds to noisy data by inferring models that are progressively smoother as noise increases (Figs 4.10d-f). The main effect of introducing a data gap near the

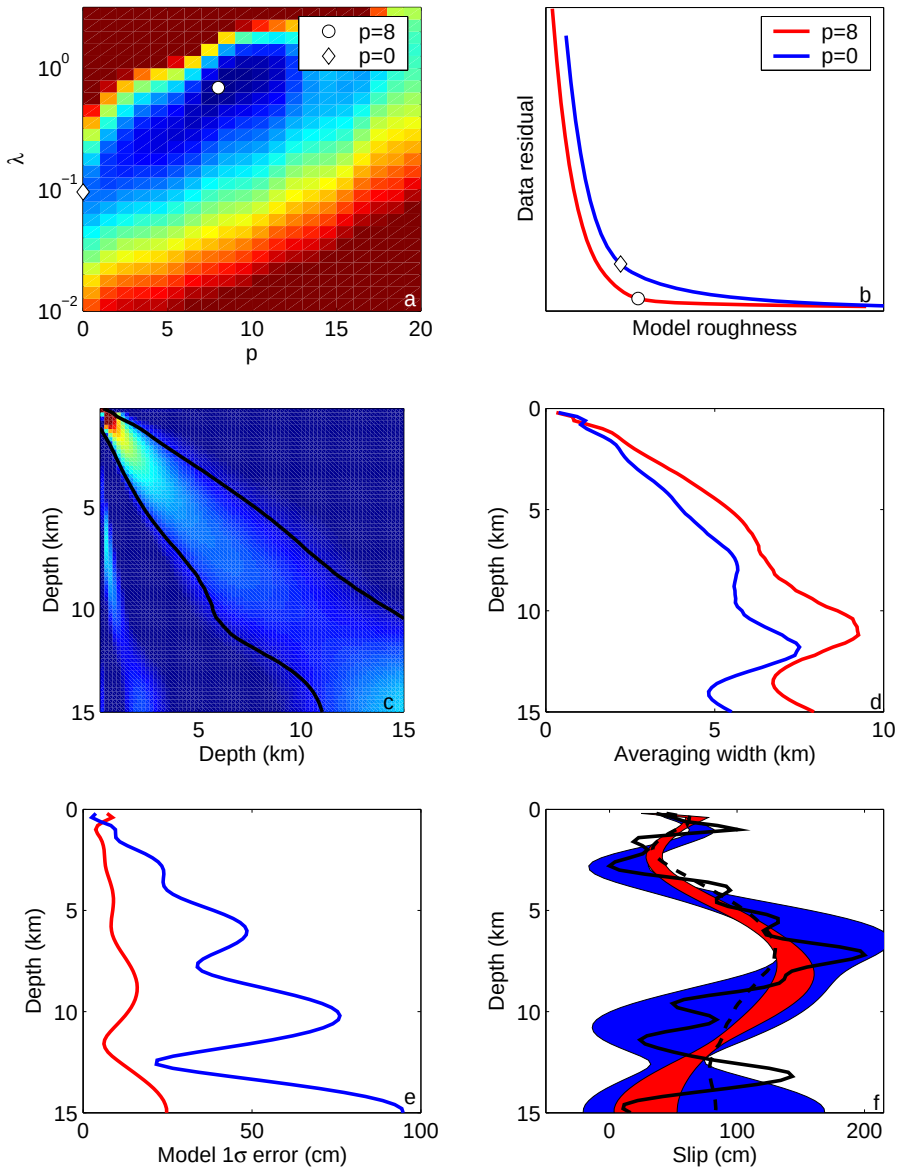

Figure 4.9: Effect of $f(\Omega)$ on properties of inferred slip distribution. All panels refer to the 1-D geometry with 0.2 km fault patches and σ=1 mm noise. a: ${}_j\mathcal{R}_i$ surface *vs.* λ and p. The white circle indicates the value of (p, λ) that minimizes ${}_j\mathcal{R}_i$, and the white triangle indicates the optimal value of λ for p=0 (constant smoothing). b: Traditional "L-curve" representation of model misfit *vs.* data residual, illustrating how our ${}_j\mathcal{R}_i$-criterion extracts values of λ that are near the corner of the L-curve. c: Resolution matrix, R, for the optimal (p, λ). Black lines indicate the width of the best-fitting Gaussian for each row, which we define as W (Appendix A.2). d: W for the p=8 and p=0 cases. e: 1σ error bounds on the inferred slip models. f: Input slip distribution (heavy line) and 1σ confidence limits on both inferred slip distributions (shaded). Note the difference in 1σ error bounds between the two models. Dashed line demonstrates the result of running a Gaussian window of width W (for optimal p, λ) over the input slip model (Appendix A.2).

Table 4.1: Model parameters from Figure 4.10

Patchsize (km)	Gap (km)	σ (cm)	p	$\log_{10}\lambda$
0.5	0.5	1	0	-0.80
1	0.5	1	0	-1.26
2	0.5	1	0	-1.76
0.2	0.2	0.1	3	-0.63
0.2	0.2	1	12	-0.20
0.2	0.2	3	0	-0.02
0.2	2	1	0	-0.16
0.2	5	1	8	0.01

fault is that the averaging scale becomes larger at shallow depths (Figure 4.10h).

4.4.2 2-D

For the 2-D case, we again begin by demonstrating the importance of allowing for variable $f(\Omega)$. We use the geometry described in Figure 4.3, beginning with observations of only the along-strike, or Y-component, of deformation over half of the coseismic deformation field. We invert for the best (p, λ) pair, and examine the difference with p=0 (Figure 4.11). The inferred model in Figure 4.11a corresponds to m_0^*, and only represents smoothing of the input model by the corresponding model resolution matrix, R. A model, m_i^*, that would be inferred from any given noisy dataset is likely to fall within the bounds indicated by the model 1σ error in Figure 4.11b. For the remainder of this paper, when we refer to "inferred model", we mean m_0^*. We find that the inferred model with p=7 (Figure 4.11a) differs from that for p=0 by only 5-10% in this case (Figure 4.11d). However, we find that the model error bounds (Figure 4.11b) varies a great deal from the p=0 case (Figure 4.11e). In Panels 4.11d-f, the dashed curve indicates zero change, so that negative regions indicate decreases in model error. As we saw in the 1-D case (Figure 4.9e), we can improve model error over most of the fault plane, at the expense of a slightly larger error at shallow depths. Inversions with p=0 attempt to model the surface region too well, at the expense of model error at depth.

Next, we vary data noise, fault patch size and observation geometry (Figs 4.12

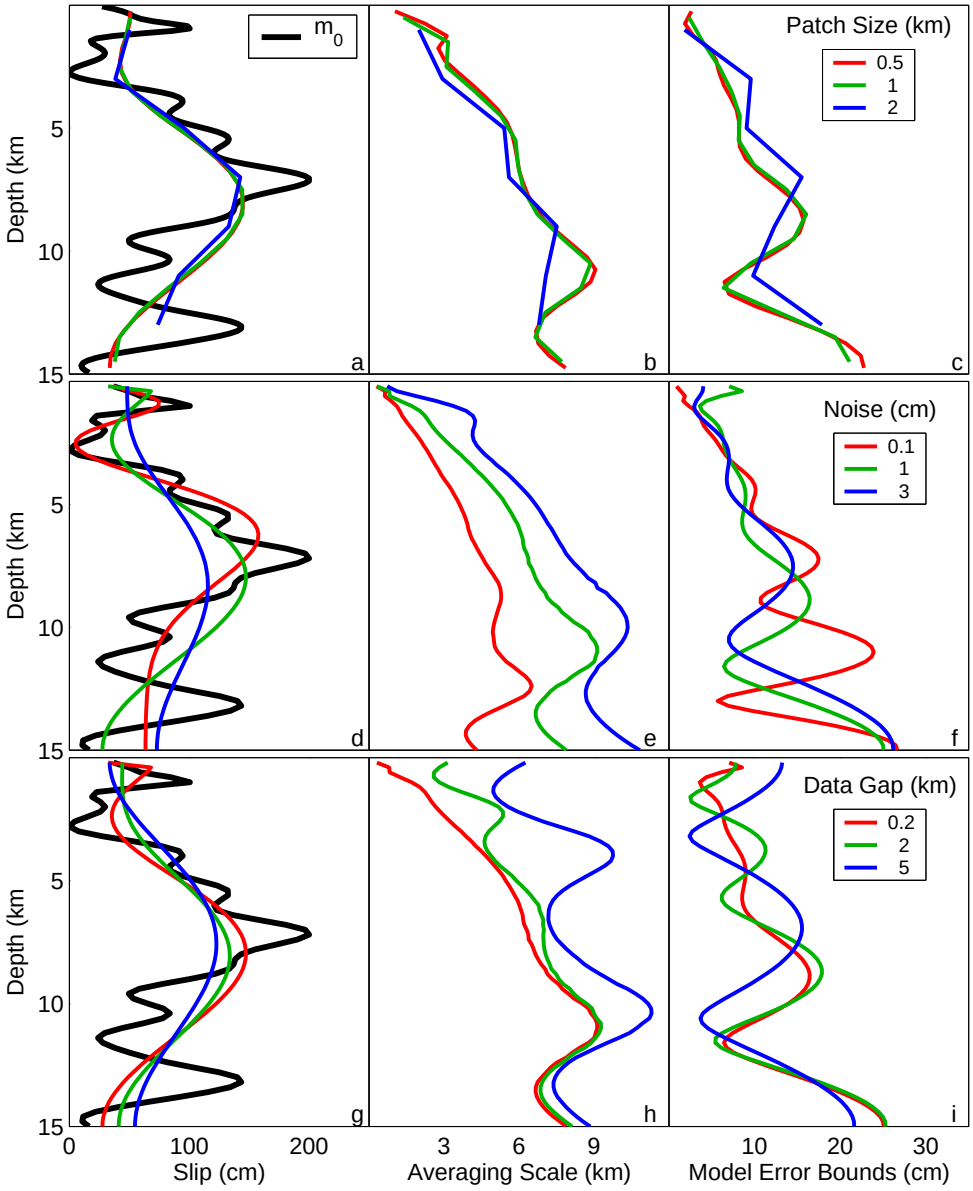

Figure 4.10: Sensitivities of inferred slip model, averaging scale and 1σ error bounds in the 1-D case. The left column contains the input slip model (m_0) and inferred slip models for each case. The center and right columns shows the averaging scale, W, and the 1σ error bounds on the inferred slip, respectively. Rows correspond to tests where we varied the fault patch size (a-c), noise level (d-f) and size of a data gap near the fault (g-i). Each inversion for the fault patch size test (a-c) used the same data set created with a 0.1 km fault patch size, although the fault patches used in the inversion ranged from 0.1-2 km in width. (p, λ) for each model are in Table 4.1. Oscillations in W and model error are a consequence of smoothing on a finite fault plane.

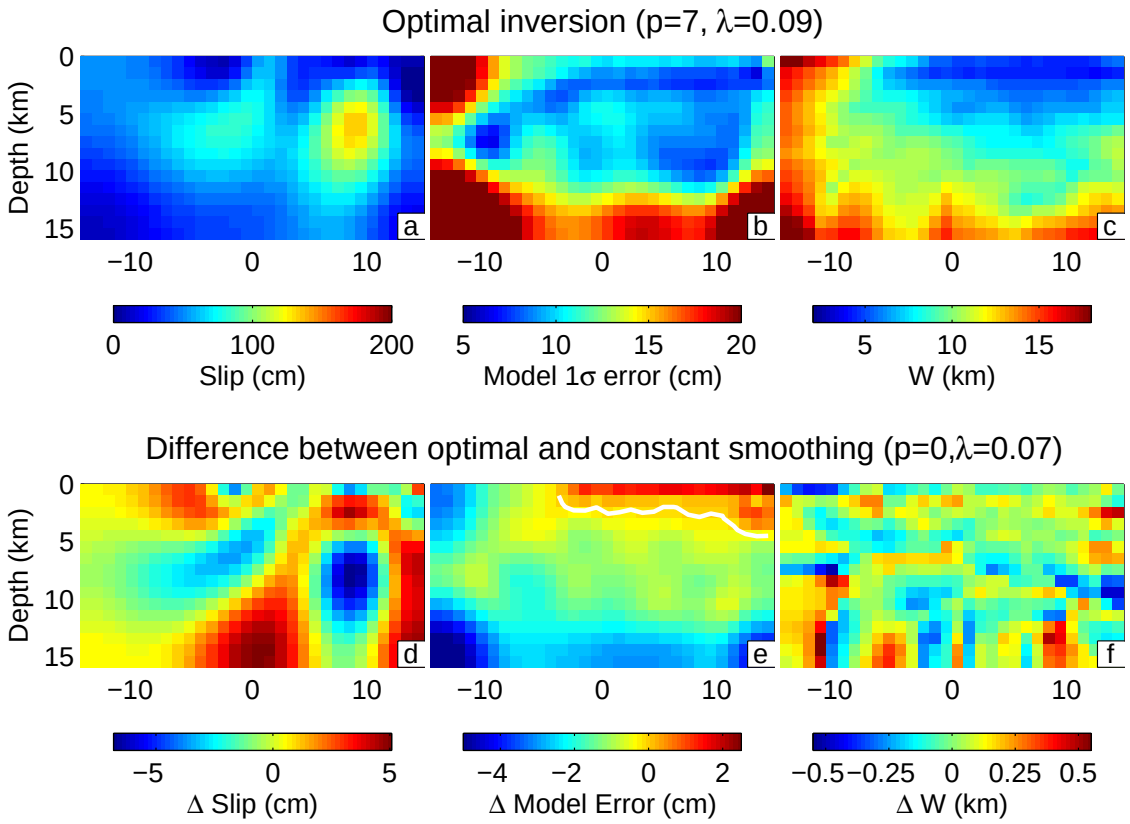

Figure 4.11: Effect of p in the 2-D case: (a,b,c) Inferred slip, model 1σ error bounds, and W, for optimal (p, λ). (d,e,f) Difference between optimal model and model chosen under constant smoothing (p=0) condition. Dashed line in (d-f) is a zero contour. Negative values in (e) and (f) correspond to improvements in model error and W for the p=7 model. This inversion used only the Y-component of deformation, with σ=1 cm noise, and constrained the rake to purely strike-slip motion.

and 4.13). As in the 1-D case, we find that our inversions are relatively invariant with respect to fault patch size (Figs 4.12a and b), as long as our fault patches are smaller than the theoretical resolution of the fault plane. We examine the dependence on observation geometry by adding the vertical and the second horizontal components of displacement to our inversions, while keeping the total number of data points fixed (Figure 4.13). The 1σ error bounds and averaging scale on the inferred model improve significantly when we add the vertical component, even though we use the same number of data points (Figs 4.13e and f). Adding the second horizontal component has minimal effect. Tradeoffs between strike-slip and dip-slip displacements decrease as we add components, as evidenced by the fact that the rake in panels (b) and (c) is nearly purely strike-slip.

4.5 Recipe and example

In a real application where we cannot compute ${}_j\mathcal{R}_i^t$, we would perform the following operations:

1. Begin with data set, fault geometry, and initial guess at noise covariance matrix.
2. Calculate ${}_j\mathcal{R}_i^a$ (See Appendix A.4).
3. Re-estimate noise variance from data residual (See Appendix A.1).
4. Repeat steps (ii) and (iii) if noise variance differs significantly from initial guess.
5. Run resampling algorithm for error bounds on model (See Appendix A.1).
6. Assess output model, error bounds and averaging scale. If smaller error bounds are needed and a larger averaging scale is acceptable, rerun inversion with larger value of λ. If averaging scale is not around 2-3 times the size of the fault patches, consider re-parameterizing problem with variably-sized patches (*Sagiya and Thatcher*, 1999; *Pritchard et al.*, 2002; *Simons et al.*, 2002).

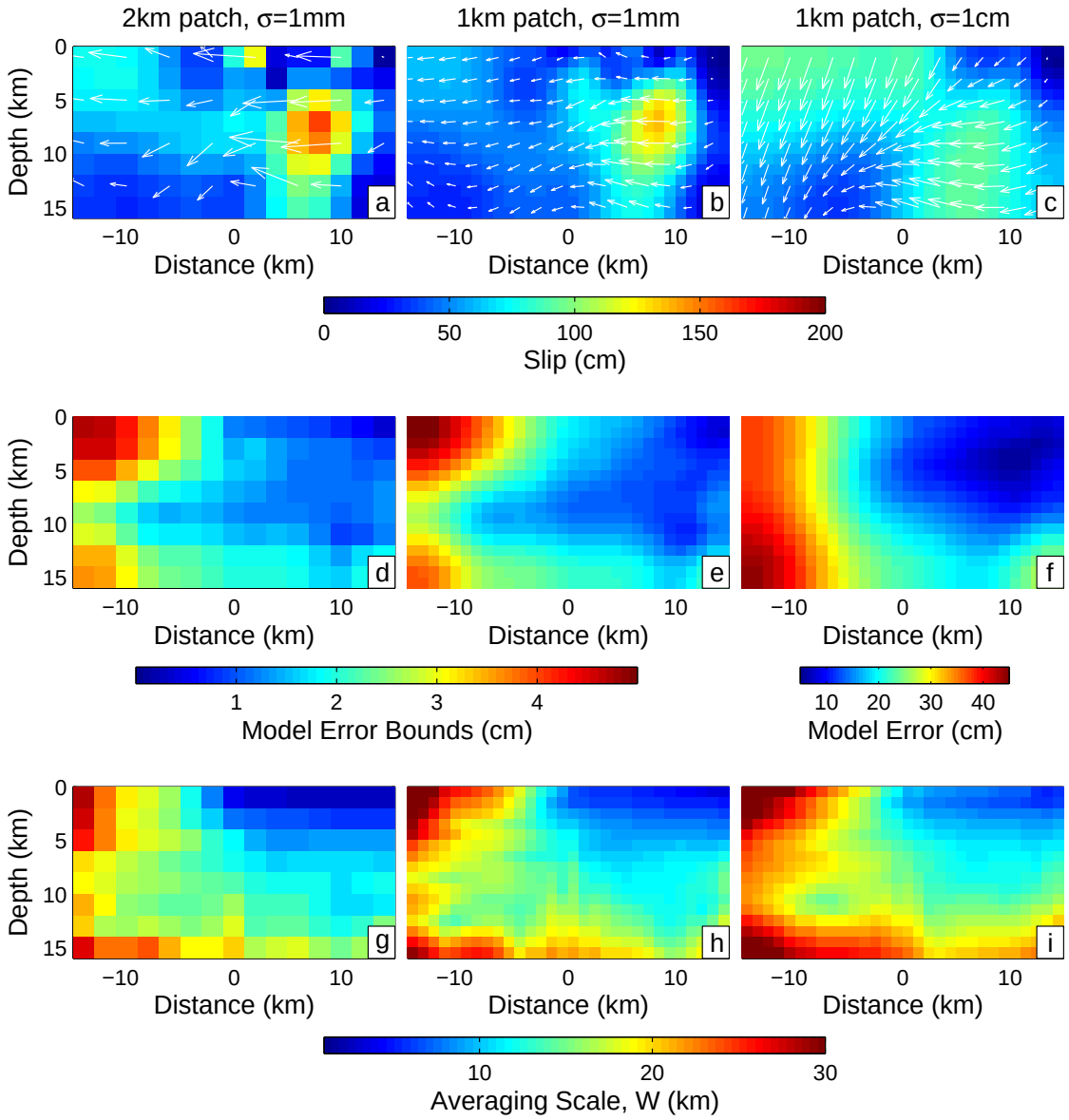

Figure 4.12: Behavior of the inversion for a 2-D system using different patch sizes and levels of noise: Patch=2 km, σ=1 mm (left column), patch=1 km, σ=1 mm (middle column), and patch=1 km, σ=1 cm (right column). We use the Y-component of deformation with a 1 km data gap near the fault. a,b,c: Inferred slip. Arrows indicate the rake of the slip vector at each fault patch. d,e,f: Model 1σ error bounds. Note the difference in scale between (d,e) and (f). g,h,i: W for each case.

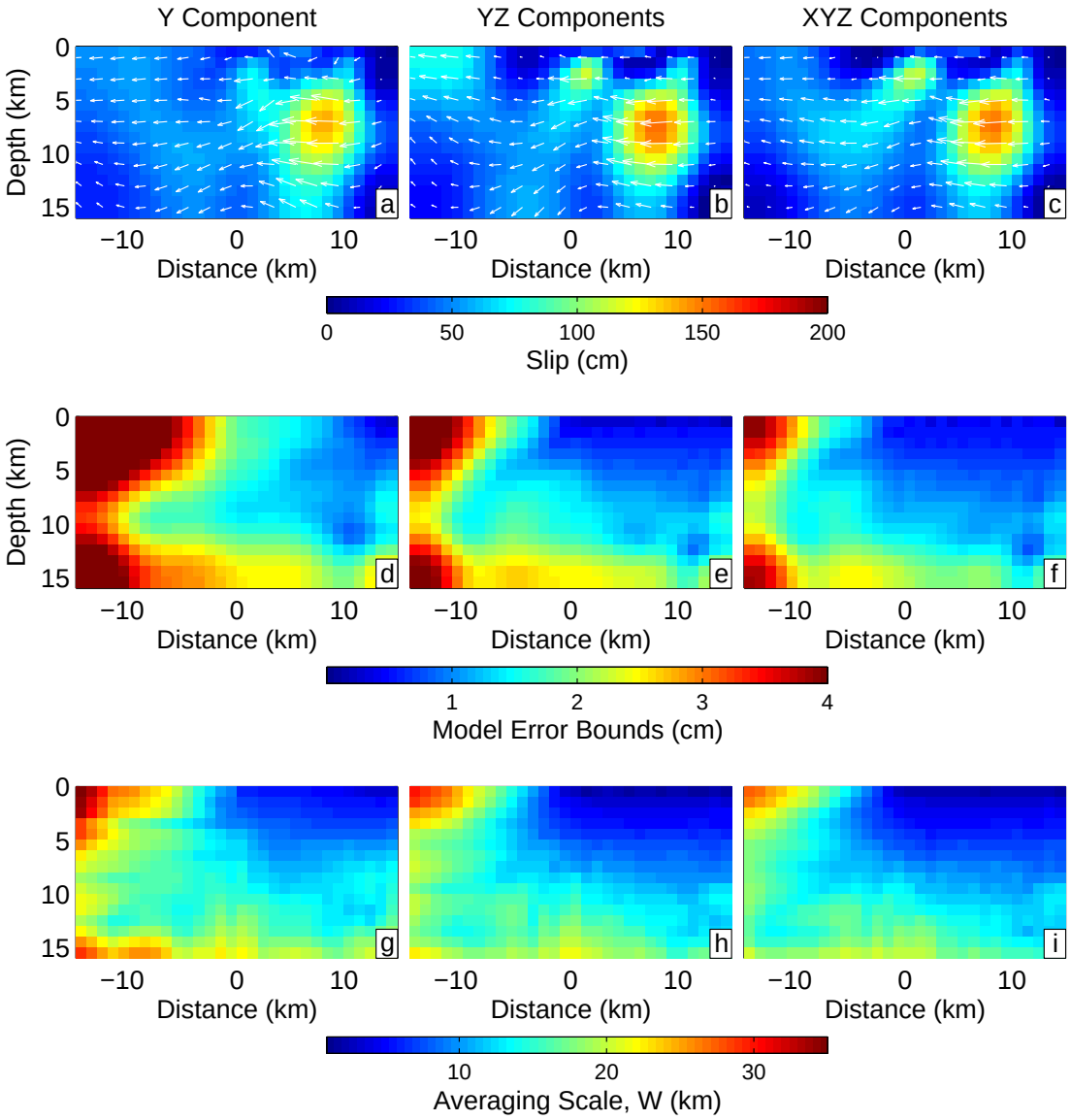

Figure 4.13: Dependence on observation geometry: Y component (left), Y and Z components (center), and all 3 components of deformation (right). Fault patches are 1 km, there is a 1 km data gap near the fault, and σ is 1 mm. The surface data density changes in each column so that the number of points in each inversion is constant. Rows and symbols are as for Figure 4.12.

We explore this method with a synthetic example involving a subduction zone earthquake with pure dip-slip motion (Figure 4.14a). Our fault plane dips 20° to the east and has 10 km fault patches. We simulate a realistic scenario where we have sets of data observations that combine different components of the deformation and different noise levels. We use a broad grid of observations of the vertical component of deformation (U_V) over the "on-shore" region (σ=1 cm), and three more precise measurements (σ=1 mm) of both the horizontal components (U_H). Initially, we examine this data-fault geometry with ${}_j\mathcal{R}_i^t$. The choice of p is driven by the U_H points, since they have much smaller model error and are located in regions where the deformation signal is large. The signal in the southwest corner of the fault plane is allowed to be more rough than if we had forced p=0. When we examine the inferred slip, model error and W (Figure 4.14), we see that the inversion is able to resolve most of the major peaks in the input model with an averaging scale that increases downdip. We note that over the entire fault plane, W is larger than 10 km, indicating that we would get no further information about fault slip if we decreased our fault patch size. In fact, we could double or triple the size of the patches half-way down the fault plane if we needed to decrease the computational burden of this inversion.

Next, we follow a dataset through our inversion process as if we had no knowledge of m_0 and an incorrect first guess at the U_V noise, σ=3 cm. We assume that we correctly know the variance of the U_H noise. The main effect of this incorrect guess is that we will over-weight the U_H data points in the inversion and infer a much higher model covariance for our inferred slip model. For each dataset, we run steps (ii)-(iii) three times. After the first iteration, we find that the U_V data residual has $\sigma\sim$1 cm (Figure 4.15). Further iterations do not improve greatly on this result, and the inferred values of (p, λ) remain approximately the same.

We note that this iteration on the estimation of C_d does not violate any laws about *a priori* assumptions, because we are merely using it to choose (p, λ). Any choice of (p, λ) is "correct" if we accompany our inferred slip model (Figure 4.16a) with appropriate measure of model error and resolution. We could calculate the error on our model estimate analytically using our new estimate of C_d, but it is safer to infer

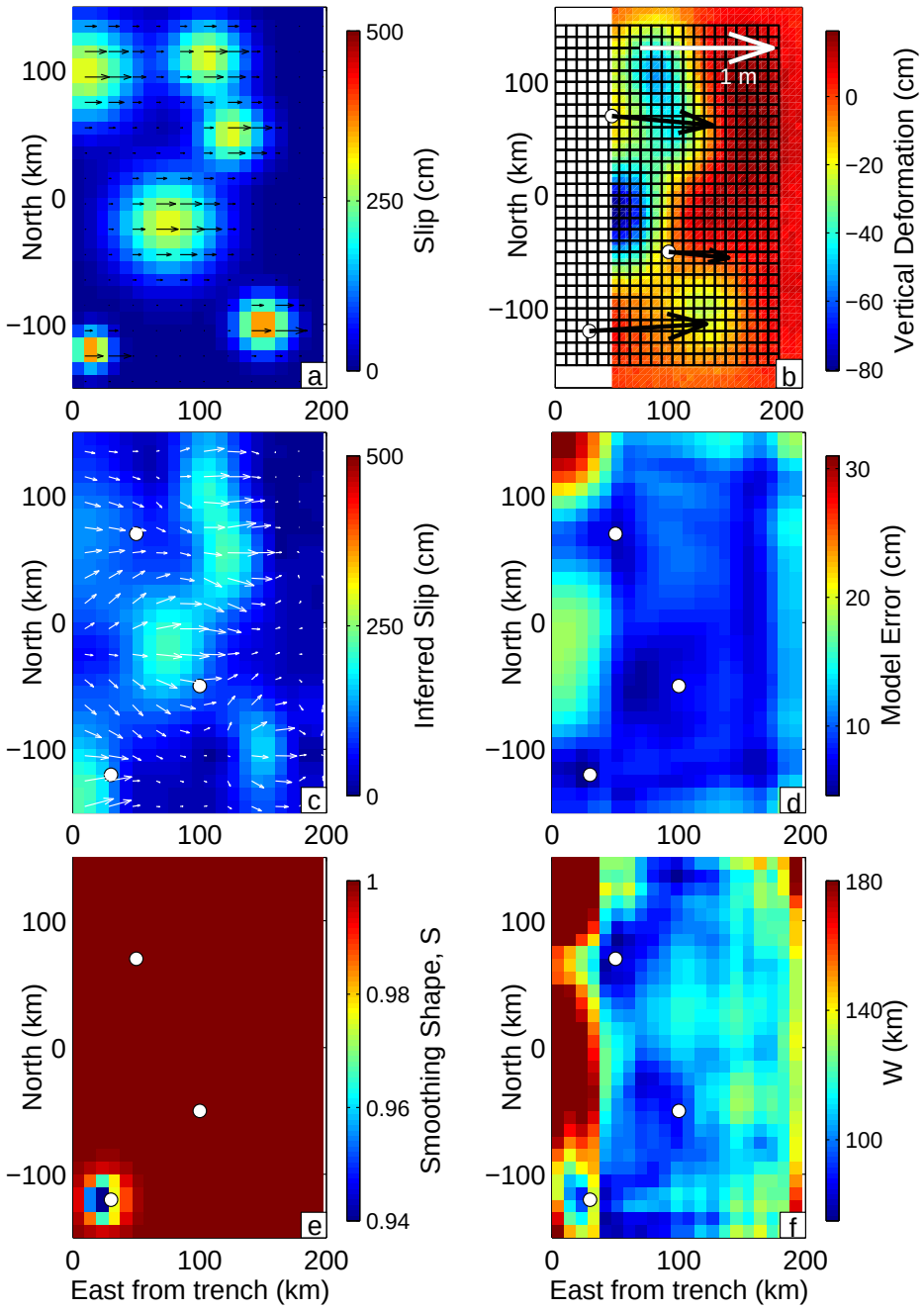

Figure 4.14: Subduction zone setup, a: Input slip distribution on fault plane dipping 20° to the east, with pure dip-slip motion. Arrows indicate slip direction on downgoing plate. b: Data produced by m_0, with noise. We use observations of the vertical component of deformation (U_V) over a region east of the subduction zone, with σ=1 cm noise, and observations of both horizontal components of deformation (U_H) with σ=1 mm (circles and arrows). Grid indicates the fault plane. c: Inferred model, m_0^*, for (p=1, λ=0.089). d: Model 1σ error bounds. e: Smoothing shape, S, which is dominated by the shallowest U_H point. f: Averaging scale, W. Note how U_H points (circles) affect resolution in (c)-(f)

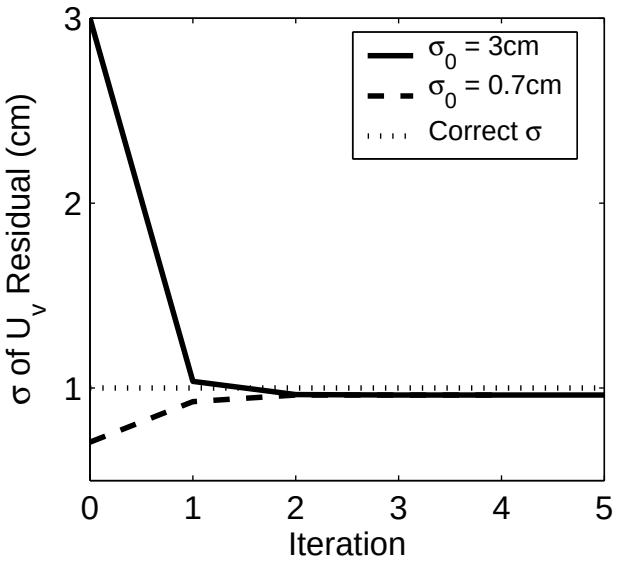

Figure 4.15: Subduction zone inversion results: Standard deviation of U_V data residual for inferred model at each iteration where we started with incorrect guesses of σ=3 cm (solid line) and σ=0.7 cm (dashed line), compared with correct σ=1 cm (dotted line).

the error on our model using resampling (Appendix A.1), since we would violate laws about *a priori* assumptions by using an *a posteriori* estimate of C_d. In Figs 4.16c and d we show both estimates of error, which are very similar, indicating that we have ended with a reasonable approximation of C_d. We calculate the residual between m_i^* and m_0^* (Figure 4.16e) and find that over most of the fault plane we match the smoothed input model to within our inferred 1σ error bounds (Figure 4.16f).

4.6 Other $f(\Omega)$

The ${}_j\mathcal{R}_i$-criterion can also be used to distinguish between various fault plane geometries or other nonlinear measures of misfit such as positivity or spatial compactness. To demonstrate this flexibility, we created a synthetic dataset from a fault plane dipping 75°, and inverted using fault planes that dipped between 70° and 80° (Figure 4.17). The fault plane dip is effectively a third dimension in our (p, λ) parameter space. In Figure 4.17a, we show the minimum ${}_j\mathcal{R}_i^t$ for each dip, demonstrating that there is a distinct minimum near the correct dip value.

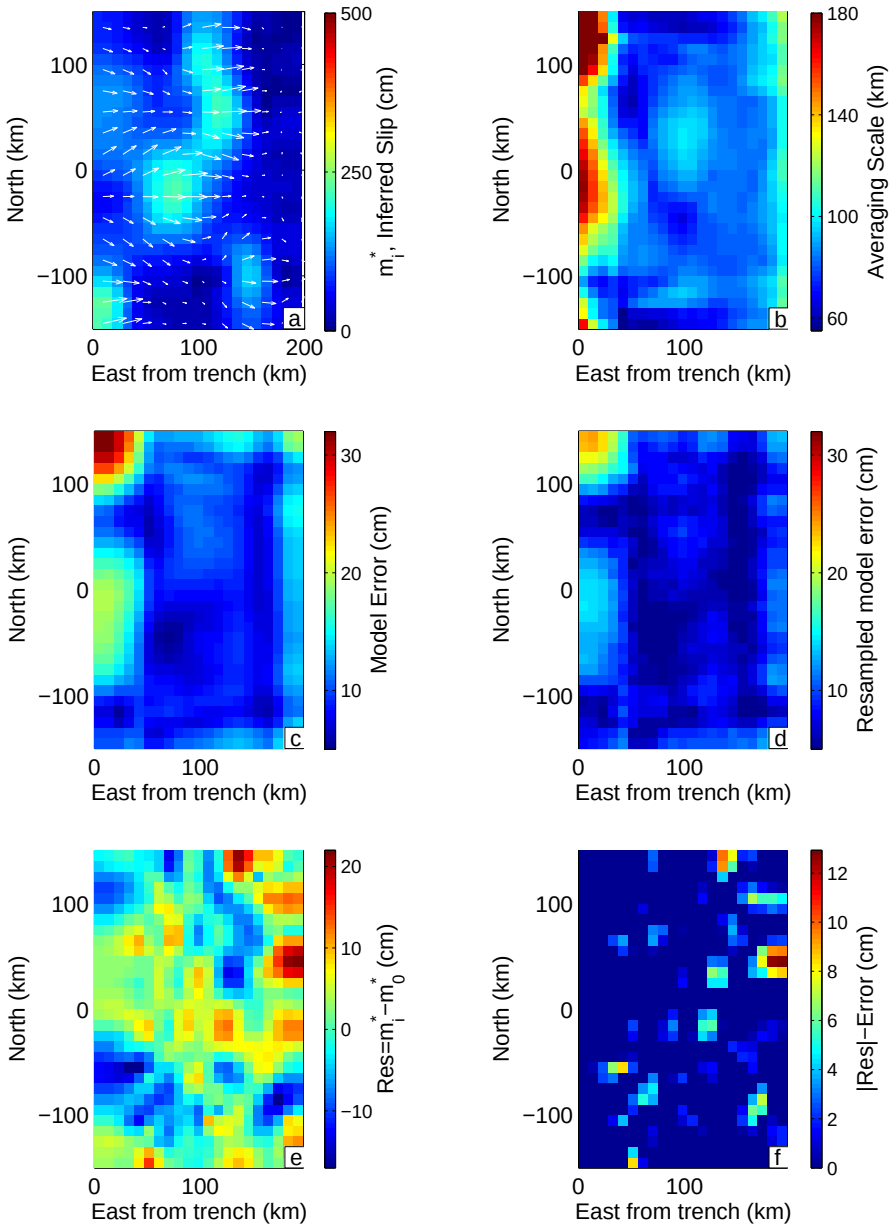

Figure 4.16: Subduction zone inversion results (p=2, λ=0.083) a: Inferred slip model, m_i^*, with slip vectors (white arrows). b: Averaging scale, W, for this inversion. c: 1σ error on inferred model, calculated using final C_d. d: 1σ error bounds on inferred model, calculated from 200 resamples of the dataset (Appendix A.1), with same colorscale as (c). e: Residual between m_i^* and m_0^* for this regularization, or the contribution of noise to the inferred model. f: Difference between absolute value of residual in (e) and the inferred error level from (d). We have set the colorscale to only show positive regions, corresponding to areas where we have not fit the smoothed input model to within 1σ error.

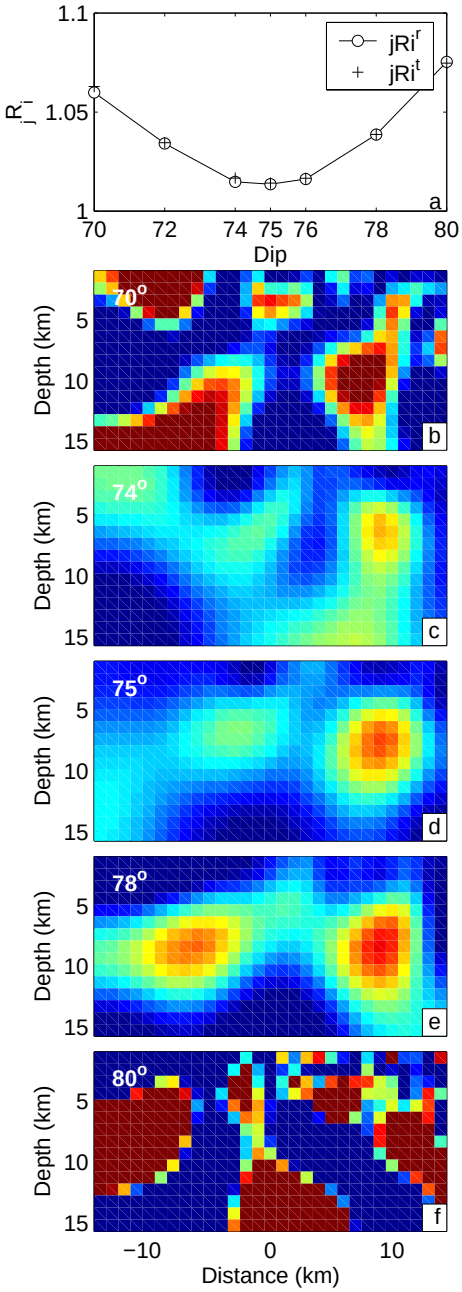

Figure 4.17: Sensitivity of the inversion approach to fault dip: ${}_j\mathcal{R}_i$ (a) for inversions with fault planes dipping from $70° - 80°$ (b-f). Input data is from fault plane with $75°$ dip. The data are the Y-component of deformation and we fix the rake to purely strike-slip motion.

When we include nonlinear penalty functions, such as positivity constraints, we cannot form a generalized inverse (G^{-g}), and our only tool is the ${}_j\mathcal{R}_i^r$ method. As a test example, we performed an inversion for fault slip using a fault plane with 25 2×2 km fault patches, with an input slip function of 2 m on one of the shallower patches (Figure 4.18a). The data in this example form a relatively coarse grid, and includes noise with σ=1 cm. An inversion without positivity constraints extracts only a very smoothed version of the input slip distribution (Figure 4.18b), whereas an inversion with positivity constraints on the strike-slip component allows us to infer a very close approximation of the slip with minimal contribution from the noise (Figure 4.18c). Both inferred slip distributions are m_i^*, not m_0^*, so they include one realization of the noise. Positivity constraints keep the inversion from fitting the data by inferring wildly oscillation slip variations at depth. Therefore, inversions with positivity constraints require a smaller degree of smoothing (e.g., *Du et al.*, 1992; *Pritchard et al.*, 2002).

We note that if we wish to simultaneously use positivity and variable smoothing, we run into the problem that it is difficult to compute the SVD with positivity constraints. However, we can still view the $f(\Omega)$ that we derive from the normal SVD as a family of potential smoothing shapes, and use the ${}_j\mathcal{R}_i^r$ method to choose from among them.

4.7 Conclusions

We have demonstrated that the ${}_j\mathcal{R}_i$-criterion extracts the slip distribution that best balances model error introduced by noise and the error associated with smoothing. The ${}_j\mathcal{R}_i$-criterion can be applied somewhat automatically to a wide range of data-model scenarios, and produces straightforward error bounds and averaging scales for the model. Explicit presentation of error bounds and spatial averaging scales allows one to focus in on features of the model that are constrained by the data.

In most of the scenarios examined here, we did not find more than a $\sim$10% change in the inferred models when we allowed SVD-based variable-smoothing. We expect

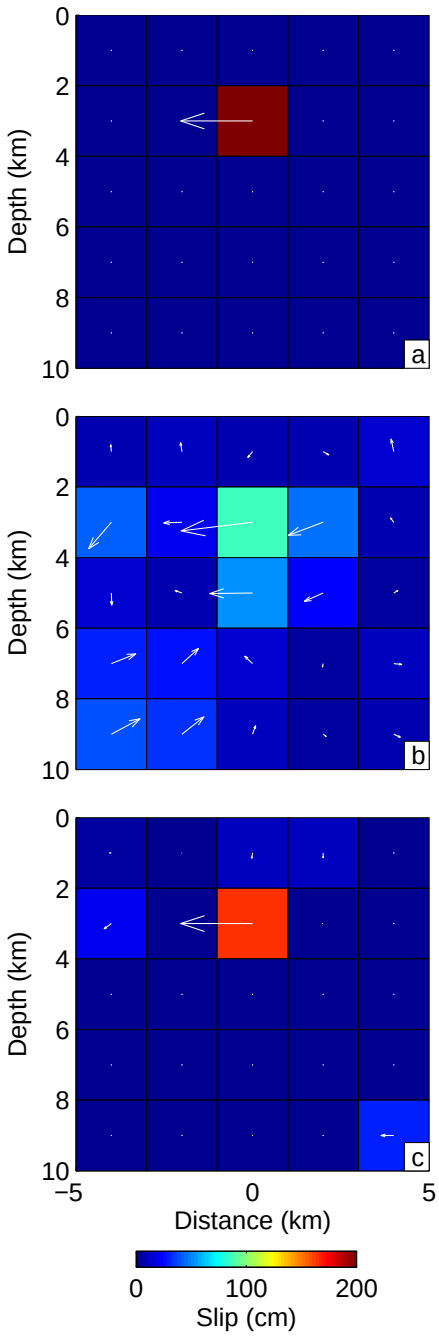

Figure 4.18: Effect of positivity constraints, a: Input slip distribution. b: Inferred model without positivity (p=1, λ=0.025). c: Inferred model with positivity (p=3, λ=0.001). Both inferred models correspond to m_i^*, not m_0^*, so they only include the effect of one realization of the noise.

that scenarios exist where variable-smoothing will have a much greater effect, especially in regions with very heterogeneous data coverage or where there is a large difference in magnitude between basis functions. Other families of $f(\Omega)$ may exist that provide further optimization of ${}_j\mathcal{R}_i$.

A.1 Errors

We propagate known data covariance structure C_d into errors on our model estimates by premultiplying G and d by C_d^{-1} (e.g., *Harris and Segall*, 1987; *Segall and Harris*, 1987). This rescales Equation 4.2 so that we can include observations with different signal to noise ratios (SNR) in our inversions. If C_d is non-diagonal, as is generally the case with InSAR observations (*Emardson et al.*, 2003), we transform our system of equations by premultiplying with $P = Q^{-1}$, where Q is the Cholesky factorization of C_d such that $QQ^T = C_d$. This operations results in reweighted data with unit variance. The covariance matrix of the model, C_m, is (e.g., *Menke*, 1989):

$$C_m = G^{-g} G^{-gT} \tag{4.28}$$

In the case where we do not have a good approximation of C_d, we can also compute model errors using resampling techniques (e.g., *Árnadóttir and Segall*, 1994; *Freymueller et al.*, 1994). We form a large number of resamples of the data set ($\sim$200-500 are necessary for most of the problems in this paper), and infer slip models from each resample. For each fault patch, we then take the upper and lower 1σ bounds on the family of inferred values. We define the standard deviation of our model as half of the difference between the upper and lower bounds on each fault patch.

We re-estimate the variance of our noise from the data residual, $d_i - d_i^*$. The estimated variance is $[d_i - d_i^*][d_i - d_i^*]^T$.

A.2 Calculation of R and W

We compute the resolution matrix, R, in two ways (e.g., *Menke*, 1989):

$$R = V_p V_p^T \tag{4.29}$$

where p is the SVD truncation value and V_p are the first p columns of the SVD matrix of eigenvectors.

$$R = G^{-g} G \tag{4.30}$$

where G is the matrix of Green's functions and G^{-g} is the generalized inverse.

In the 1-D case, we derive W from R by finding the width of the best-fitting Gaussian curve to each row of R. This width is a good approximation of the "local" averaging scale, and does not include effects from secondary peaks in R (Figure 4.9). We find that this definition of W gives us an intuitive feel for the spatial scale of averaging in the 1-D case. It is not a perfect measure, however, since filtering m_0 by a Gaussian window of width W on each patch does not give us the same result as the product Rm_0, or m_0^* (Figure 4.9f).

In the 2-D case, we define measures of W as the standard deviation of R in either the along-strike (W_h) or down-dip (W_v) directions (Figure 4.5). When we allow both strike-slip and dip-slip motion, R has four quadrants that relate strike-slip and dip-slip motion to each other. In general, the strike-slip and dip-slip components of R behave differently, so we compute W_h and W_v for dip-slip and strike-slip deformation, for a total of 8 separate measures of W. In the body of this paper, we refer to W as the RMS of the 4 components relating to the purely strike-slip and dip-slip quadrants of R (Figure 4.5). Note that for the poorly resolved fault patch (right column), the inferred slip for either the dip-slip or strike-slip components is dominated by slip on the fault plane in regions far from the fault patch. This poor resolution is a result of the lack of data points on the left side of the fault plane (Figure 4.3).

A.3 Derivation of ${}_j\mathcal{R}_i^t$

We seek an efficient way to calculate ${}_j\mathcal{R}_i$. We expand Equation 4.22 using Equation 4.20:

$$ {}_j\mathcal{R}_i = 1/k \sum_x [({}_0r_0)^2 + 2({}_0r_0)({}_jr_i^n) + ({}_jr_i^n)^2] \tag{4.31} $$

Since ${}_jr_i^n$ is a random variable with mean 0, the middle term disappears and we are left with:

$$ {}_j\mathcal{R}_i = 1/k \sum_x ({}_0r_0)^2 + 1/k \sum_x ({}_jr_i^n)^2 \tag{4.32} $$

The first term is equivalent to the definition of ${}_0\mathcal{R}_0$. Since the mean of ${}_jr_i^n$ is 0, the expectation of the second term in Equation 4.32 is a sum over the variances of ${}_jr_i^n$ at each data point (Equation 4.26).

A.4 Derivation of ${}_j\mathcal{R}_i^a$

In order to form an approximation of ${}_j\mathcal{R}_i$ in the case where we only have one dataset, we use the relations:

$$ {}_ir_i = {}_0r_0 + {}_ir_i^n \tag{4.33} $$

$$ {}_jr_i = {}_0r_0 + {}_jr_i^n \tag{4.34} $$

We can compute one realization of ${}_ir_i = d_i - d_i^*$ using our existing dataset, and we can calculate ${}_ir_i^n$ and ${}_jr_i^n$ if we assume C_d (Equation 4.24). Therefore, our approximation of ${}_j\mathcal{R}_i$ is:

$$ {}_j\mathcal{R}_i^a = \frac{1}{k} \sum_x [{}_ir_i - {}_ir_i^n + {}_jr_i^n] \tag{4.35} $$

where k is the number of data observations and the sum is over all data. We show how the use of only one realization of ${}_ir_i$ introduces a scatter in our approximation of ${}_j\mathcal{R}_i$ in Figure 4.8.

Chapter 5

Applications of ${}_j\mathcal{R}_i$ method

Abstract

I use the ${}_j\mathcal{R}_i$ method from Chapter 4 to invert geodetic data for the distribution of coseismic slip for two large earthquakes, the 1998 M_w 7.1 Hector Mine, California, earthquake and the 1995 M_w 8.1 Antofagasta, Chile, earthquake. In cases where the deformation source is very near the data points, the sensitivity to model geometry is high and the data may be dominated by anelastic processes are not accounted for in the forward model used in the inversion. I present the results of an attempt to use the ${}_j\mathcal{R}_i$ method on a large strike-slip earthquake, where imprecise knowledge of the model geometry causes the ${}_j\mathcal{R}_i$ technique to break down while choosing the appropriate magnitude of regularization. I use synthetic examples to illustrate how model geometry errors propagate through the inversion, and I use the data covariance constructed as in Chapter 1 to place confidence intervals on the depth-averaged coseismic slip distribution. I show that, for an example where the deformation source far from the observations, the ${}_j\mathcal{R}_i$ method can semi-automatically choose inversion regularization parameters and fault plane geometry.

5.1 Introduction

The ${}_j\mathcal{R}_i$ (or "Jury") method outlined in Chapter 4 promises to be a semi-automatic technique for choosing the most appropriate regularization and/or model parameterizations. To demonstrate the utility of the ${}_j\mathcal{R}_i$ method, I present two examples of inversions of geodetic data for distributed coseismic slip. I begin with the 1999 M_w 7.1 Hector Mine, California earthquake. The Hector Mine event was a large strike-slip earthquake that caused several meters of mapped surface slip. There are voluminous InSAR and GPS observations associated with the Hector Mine earthquake and several publications review the available data and present slip inversion results of seismic and geodetic data (e.g., *Jónsson et al.*, 2002; *Chen et al.*, 2002a,b; *Simons et al.*, 2002).

My second example is the July 30, 1995, M_w 8.1 Antofagasta, Chile, subduction zone earthquake. For the sake of brevity and because the purpose of this chapter is merely to demonstrate the use of the ${}_j\mathcal{R}_i$ method, I invert data from only one of the interferograms spanning the deformation zone for this earthquake (Track 96, 1992/05/08-1995/10/09, $B_\perp$=50 m). Reviews of the tectonic setting for this event and slip inversions using the full set of InSAR and GPS data can be found elsewhere (e.g., *Monfret et al.*, 1995; *Ruegg et al.*, 1996; *Delouis et al.*, 1997; *Ihmlé and Ruegg*, 1997; *Reigber et al.*, 1997; *Carlo et al.*, 1999; *Klotz et al.*, 1999; *Pritchard et al.*, 2002; *Chlieh*, 2003).

5.2 Example: Hector Mine earthquake

The Hector Mine earthquake has a complicated, Y-shaped surface trace (Figure 5.1), with InSAR and GPS data (*Agnew et al.*, 2002) that come very close to the fault. I used both the ${}_j\mathcal{R}_i{}^a$ and ${}_j\mathcal{R}_i{}^r$ approximation techniques (Table 5.1), with a fault plane geometry derived from *Simons et al.* (2002) and the noise covariance derived as in Chapter 1. For this particular parameterization, neither ${}_j\mathcal{R}_i$ approximation method produced satisfactory results (Figure 5.2). The ${}_j\mathcal{R}_i{}^a$ method breaks down whenever the remaining data residual due to inadequacies in fault geometry is larger

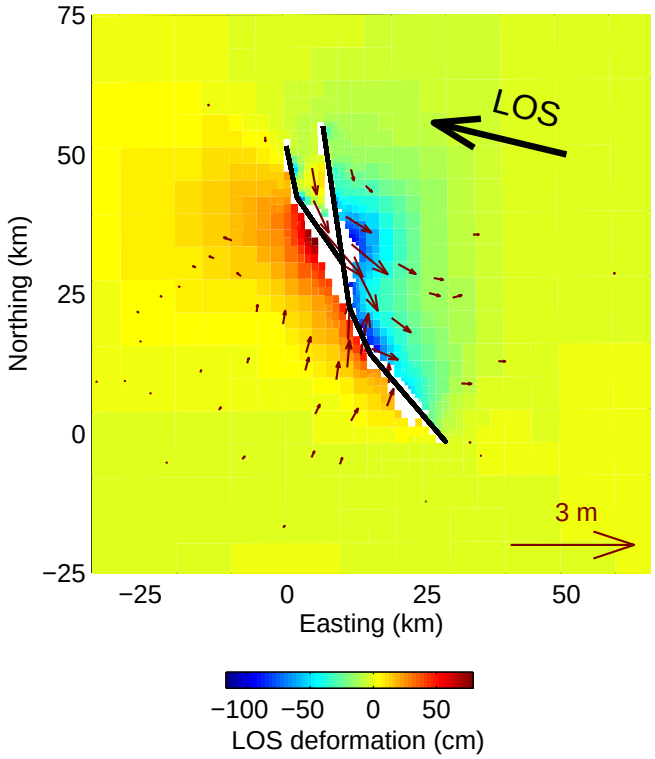

Figure 5.1: InSAR data (color) and GPS points (red arrows, from *Agnew et al.* (2002)) used in inversion for distributed slip on fault plane geometry indicated by heavy black line. Heavy black arrow corresponds to the LOS direction.

Type	Input model	C_d	Linear	Nonlinear	Speed	Utility
${}_j\mathcal{R}_i{}^t$ (Theoretical)	√	√	√		Fast	Problem design, Monte Carlo tests
${}_j\mathcal{R}_i{}^a$ (Approximate)		√	√		Fast	Comparison with ${}_j\mathcal{R}_i{}^r$
${}_j\mathcal{R}_i{}^r$ (Resampled)			√	√	Slow	All applications

Table 5.1: ${}_j\mathcal{R}_i$ review: Comparison of ${}_j\mathcal{R}_i$ methods, including whether or not they require knowledge of the input model and/or noise covariance matrix (C_d), and whether they can be applied to linear and/or nonlinear problems.

than the predicted residual due to noise, and picks an unrealistically small value of λ (Figure 5.2c). ${}_j\mathcal{R}_i{}^a$ can still be useful in cases where the character of the noise and the magnitude of model errors is well understood, and the difference between ${}_j\mathcal{R}_i{}^a$ and ${}_j\mathcal{R}_i{}^r$ provides a qualitative measure of the magnitude of model errors. ${}_j\mathcal{R}_i{}^a$ also does not suffer from the ambiguity as to how one should choose the type of resampled subset for the ${}_j\mathcal{R}_i{}^r$ approximation (i.e., cross-validation, jack-knifing, or bootstrap (e.g., *Efron and Gong*, 1983)).

The ${}_j\mathcal{R}_i{}^r$ method accounts for model geometry errors by choosing a much smoother slip distribution (Figure 5.2d), with peak slip $\sim$ 4 m. The ${}_j\mathcal{R}_i{}^r$ slip distribution for this fault geometry is inconsistent with mapped surface offsets (e.g., *Treiman et al.*, 2002) and previous seismic and coseismic slip inversions that predict peak slips of 6-7 m. Examination of the L-curve for this inversion (Figure 5.2b) suggests that a value of $\lambda = 10^{-2}$ (green dot) is closest to the "corner" of the L-curve and may best balance the fit to the data vs. the slip model complexity. For the rest of this section I will be considering only the $p = 0$ case (Chapter 4, "constant smoothing"). Once I tune the fault plane geometry appropriately and can use ${}_j\mathcal{R}_i{}^r$ to choose regularization parameters, I will be able to search the full range of (p, λ).

To examine the sensitivity of this inversion to our knowledge of the fault plane geometry, I create synthetic data using the same fault plane parameterization as in Figure 5.1, same noise covariance as the Hector Mine data, and with an input slip model using the L-curve corner value of $\lambda = 10^{-2}$ (Figure 5.2b). I then calculate

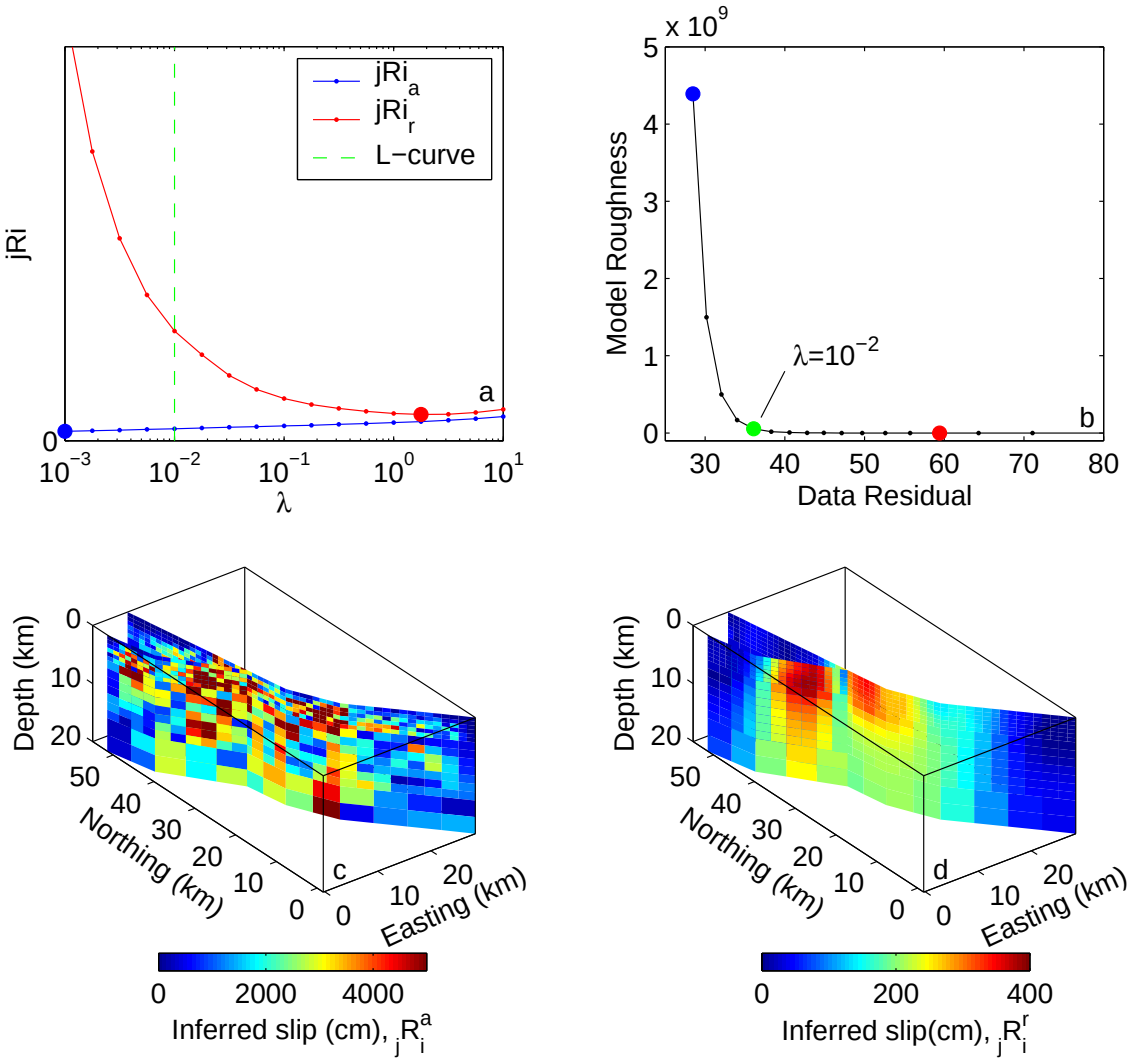

Figure 5.2: a) ${}_j\mathcal{R}_i{}^r$ (red) and ${}_j\mathcal{R}_i{}^a$ (blue). b) Data residual vs. model complexity, with the minima from (a) and the best L-curve "corner" (green circle). c) Inferred coseismic slip distribution from data in Figure 5.1, using the ${}_j\mathcal{R}_i{}^r$ value of λ. Note that fault patch size increases with depth. d) Inferred slip for ${}_j\mathcal{R}_i{}^a$ value of λ.

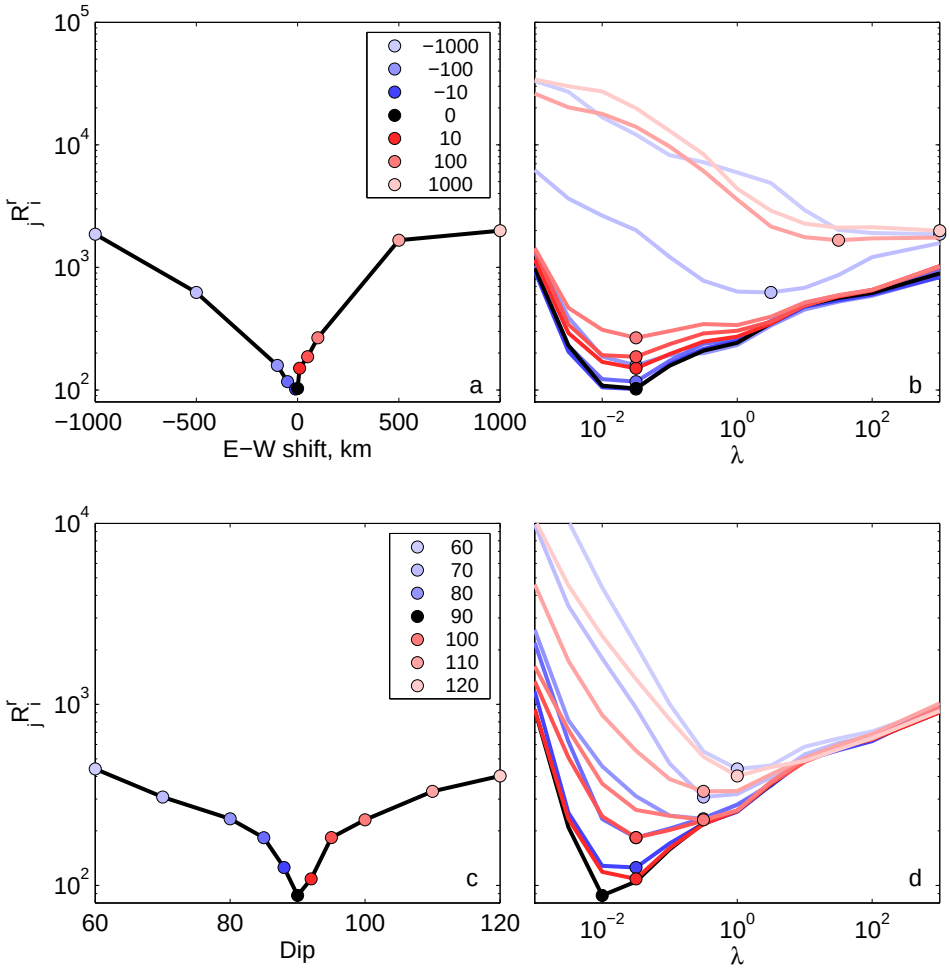

Figure 5.3: Variation of ${}_j\mathcal{R}_i{}^r$ for inversions using synthetic data and incorrect fault planes with various E-W shifts (a,b) and dips (c,d). (a,c) are the minimum values of ${}_j\mathcal{R}_i{}^r$ for each shift, and (b,d) are the values of ${}_j\mathcal{R}_i{}^r$ vs. λ, color-coded by each shift or dip. Color-coding is the same within each row, with black corresponding to the optimal fault plane geometry.

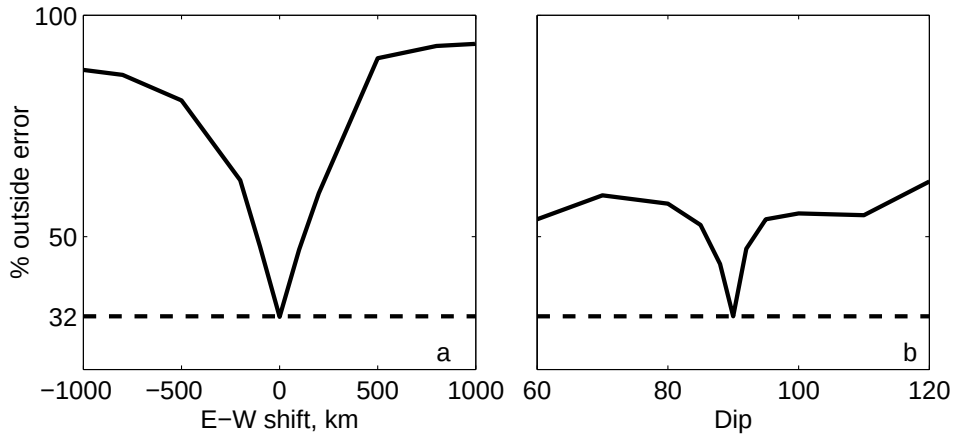

Figure 5.4: Percentage of fault patches where the inferred slip is outside the theoretical 1σ error bounds for various fault plane shifts (a) and dips (b). If the error bounds are correct, only $\sim 32\%$ of the inferred slip should fall outside the error bounds.

the resampled value of ${}_j\mathcal{R}_i$, ${}_j\mathcal{R}_i{}^r$, for inversions using various incorrect fault plane geometries, where I either shift the fault plane in an E-W direction by ± 1 km, or vary the dip of the fault plane between 60 and 120 degrees (Figure 5.3). ${}_j\mathcal{R}_i{}^r$ is minimized at the correct geometry in both of these cases. Note that as the geometry error increases, ${}_j\mathcal{R}_i{}^r$ chooses progressively larger values of λ (Figure 5.3b,d). I also show the percentage of inferred fault slip that falls within the theoretical error bounds in each case (Figure 5.4). If the geometry is incorrect, the theoretical 1σ confidence intervals will be too small, even if the slip distribution has a large amount of smoothing. This disparity between the actual and theoretical error bounds in this synthetic scenario motivates the use of bootstrapped confidence intervals that presumably account for some of the model parameterization errors.

The fact that the ${}_j\mathcal{R}_i{}^r$ criterion is sensitive to model errors implies that ${}_j\mathcal{R}_i{}^r$ may be useful for choosing a fault plane geometry. I tested nonlinear inversions for fault plane geometry, using the ${}_j\mathcal{R}_i{}^r$ value to choose the optimal fault parameterization. In synthetic tests, where I began with a perturbed geometry and used simulated annealing, the nonlinear inversion found the correct minimum only for very small perturbations of fault plane dip and locations. Future work will include optimizing the nonlinear inversion methods and determining whether the inclusion of data close to the fault (i.e., to within distances on the scale of the fault patch size) biases the

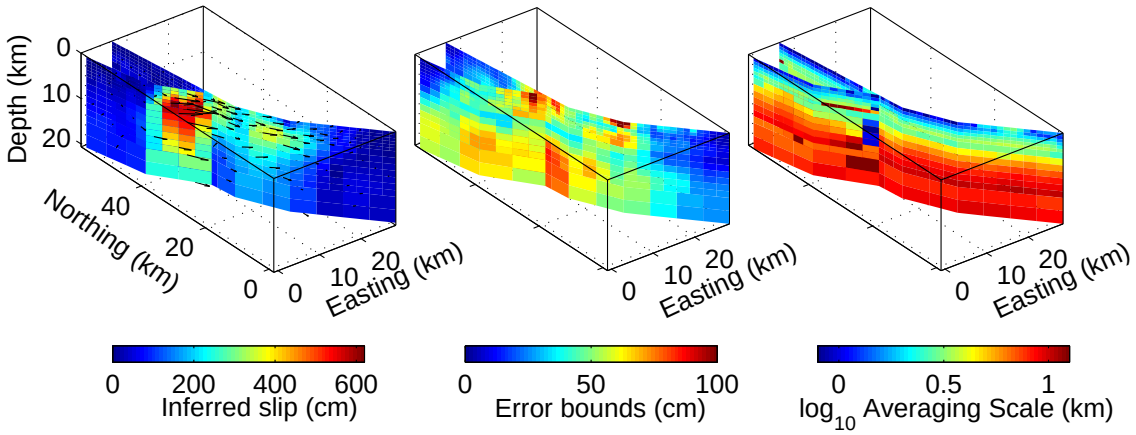

Figure 5.5: Slip distribution, bootstrapped 1σ error bounds and averaging scale, W, for the value of $\lambda = 10^{-2}$ chosen in Figure 5.2. Arrows indicate slip direction of eastern side of fault (i.e., mainly right-lateral. Gray patches on W panel indicate patches that can not be fit by a Gaussian curve of resolution vs. distance.

search technique. Currently, I have not tuned these inversion to be efficient enough that I can use the ${}_j\mathcal{R}_i$ method, so I will proceed with an inversion using the value $\lambda = 10^{-2}$ that I chose off the L-curve.

Figure 5.5 shows the inferred slip distribution, 1σ error bounds on the model and an approximate averaging scale for this choice of fault plane and λ The features in this slip model are broadly consistent with the results of *Jónsson et al.* (2002) and *Simons et al.* (2002), who used similar data sets and fault plane geometries. Note that the largest bootstrapped model errors occur near the Y-junction in the middle of the fault plane, which may indicate either that the solution is very sensitive to the exact choice of fault plane geometry at that point, or that anelastic processes such as block rotation or crushing occurred and are being mapped into slip errors during the inversion.

I end my treatment of the Hector Mine earthquake with a profile of potency (slip×area) summed along strike vs. depth (Figure 5.6), with confidence intervals derived from the bootstrapped error bounds in Figure 5.5. The inferred potency at depths greater than 15 km is in part an artifact of the fact that slip on deeper fault patches is averaged over length scales $\sim$ 10 km (Figure 5.5), so that the estimate at those depths includes contributions from shallower regions with higher slip. However,

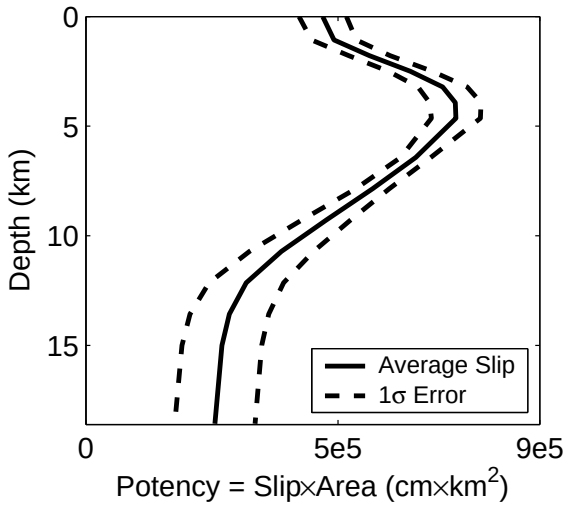

Figure 5.6: Slip×fault patch area (potency) from Figure 5.5a, summed along strike, with bootstrapped 1σ confidence bounds. Note that the potency at 4-5 km depth is greater than that near the surface at the 1σ confidence level.

the much shorter averaging scales at depths less than 5 km and the small error bounds indicate that the difference in slip between the surface and at depths of 4-5 km is significant. This result, and others like it, can be used to interpret later inversions of postseismic data, and as input to fault zone friction law studies (*Dieterich*, 1979, 1992; *Rice*, 1983; *Ruina*, 1993; *Tse and Rice*, 1986).

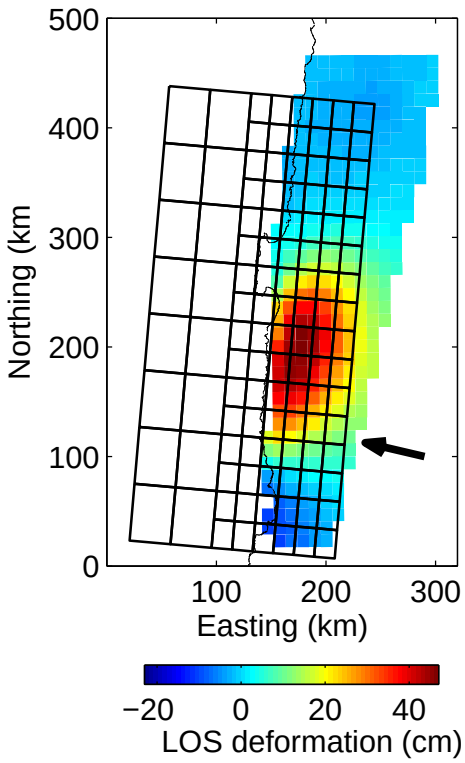

Figure 5.7: Resampled InSAR data (color) used in inversion for distributed slip on fault plane geometry indicated by black rectangles. Coastline and LOS direction are also indicated (thin line and black arrow, respectively).

5.3 Example: Antofagasta earthquake

The shortest distance between the geodetic observations and the presumed location of the subduction interface for the Antofagasta earthquake is greater than 30 km for all fault patches, leading to much less sensitivity to fault plane geometry than exists for earthquakes with data proximal to the surface trace of the fault. Therefore, it is much more likely that errors due to inadequacies in the geometry will be negligible, even for a fairly simple fault plane parameterization. I parameterize a fault plane with large (52 km×39 km) patches offshore and smaller (26 km×20 km) patches onshore, along a plane that is constrained by the location of the trench and the aftershock distribution from *Husen et al.* (1999) (Figure 5.7). All fault patches are smaller than those *Pritchard et al.* (2002) determined to be at the resolution threshold for the available data set.

The bullseye of coseismic subsidence in Figure 5.7 can be fit either by thrust-faulting near the trench and just onshore, or by physically unrealistic normal-faulting on land and downdip of the subsidence feature. I impose slip constraints requiring thrust faulting and allowing for some right-lateral slip, consistent with the observed direction of relative plate convergence. The use of model constraints turns the inversion into a nonlinear problem and rules out use of the ${}_j\mathcal{R}_i{}^a$ approximation, so I use the ${}_j\mathcal{R}_i{}^r$ method here to determine the appropriate values of p and λ (Figure 5.8a). I also provide an "L-curve"-like representation of the data residual vs. model roughness for all of the different values of p (Figure 5.8b), with the minima from (Figure 5.8a) marked as open circles. Here, the model roughness is $||S^T Dm||$, where S and D are the smoothing shape and Laplacian smoothing matrices (Section 4.3.2), and m is the slip model. It is not obvious how one would compare the curves corresponding to different values of p if the L-curve was the only tool at hand, or even how to define the best point on each individual curve. In the $p = 0$ case, the value of λ that minimizes ${}_j\mathcal{R}_i$ is slightly lower (higher model roughness) than the value closest to the corner. The ${}_j\mathcal{R}_i$ method allows me to compare all of the different regularization styles in a consistent manner, leading to the choice of $p = 215, \lambda = 5$ (Figure 5.9).

The slip distributions inferred for $p = 0$ and $p = 215$ (Figure 5.10) differ mainly in the amount of offshore slip and the magnitude of peak slip near the coast. Both are broadly consistent with the inferred slip distribution from *Pritchard et al.* (2002) (Figure 5.11), which includes all of the available geodetic data and uses a different fault plane parameterization. I form an empirical resolution matrix, R_e, by creating synthetic data using unit slip on each fault patch and invert for the rows of R_e. This value has less significance than the resolution matrix in a linear problem, as R_e is no longer an operator that acts on the input slip model. R_e still has some significance, as we can form a measure of averaging scale, W, that provides a qualitative measure of the size of feature resolved by this data set (e.g., Figure 4.5). I show W here merely to demonstrate that the offshore fault patches are smoothed over large areas (several 100 km^2), whereas the onshore fault patches are only smoothed across 1-2 neighboring fault patches.

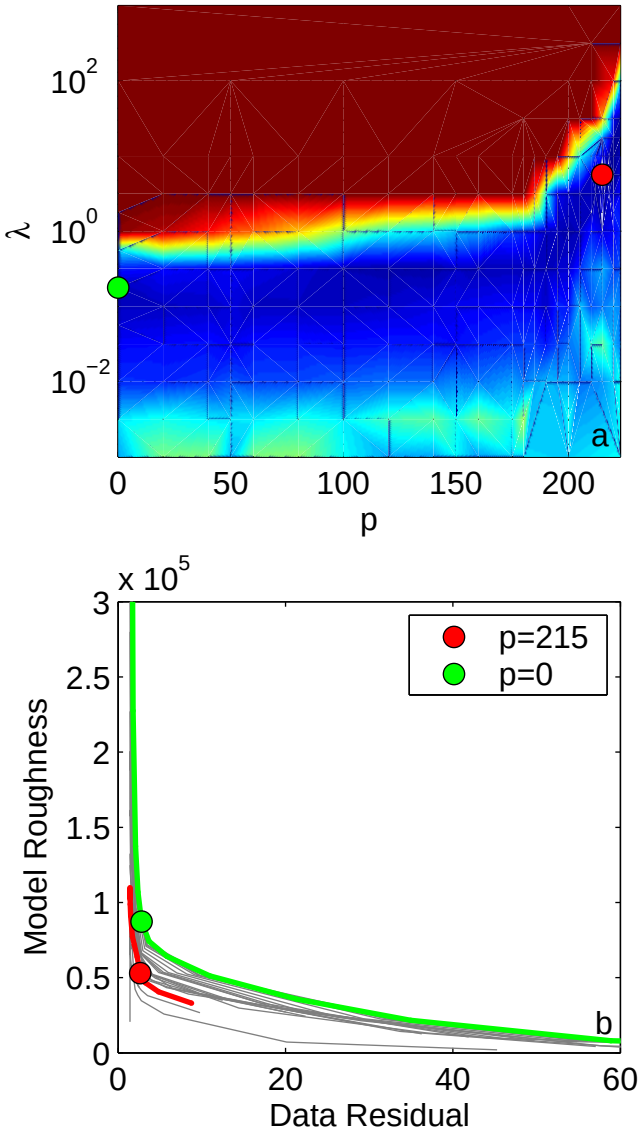

Figure 5.8: a) ${}_j\mathcal{R}_i{}^r$ for the Antofagasta earthquake. b) Data residual vs. model roughness (L-curve) for each of value of p (gray curves). Here, model roughness is $||S^T Dm||$ (see text). Colored circles indicate the minima from (a) for $p = 0$ (green) and the global minimum at p=215 (red).

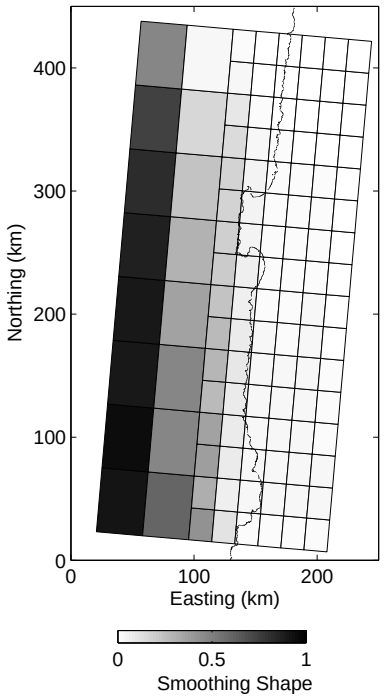

Figure 5.9: Smoothing shape for $p = 215$.

The data residual for $p = 215$ is smaller than for $p = 0$, but the characteristics of the two residuals are very similar (Figure 5.12a, b). I also show the data residual predicted for the full resolution interferogram (Figure 5.12b,d), using the slip models from Figure 5.10. As in the other inversions in this thesis, I simultaneously invert for a quadratic ramp across the image in order to account for imprecise satellite orbital estimates. Since the signal in Figure 5.7 is dominated by long wavelengths, the inferred fault slip trades off with the potential baseline error. The use of multiple interferograms will ameliorate this problem.

I end with a brief example of the use of ${}_j\mathcal{R}_i$ to distinguish between potential model parameterizations. In this case, I note that I generated the fault plane used for the Antofagasta earthquake study based on the best fit in a least squares sense to the trench and to the aftershock distribution (red curve in Figure 5.13). However, the aftershocks form a fairly diffuse cloud and, therefore, do not tightly constrain the location of the subduction zone interface. I test the sensitivity of the inferred fault slip in Figure 5.10 by scaling the depth of the fault plane by factors of 0.5 to 1.5

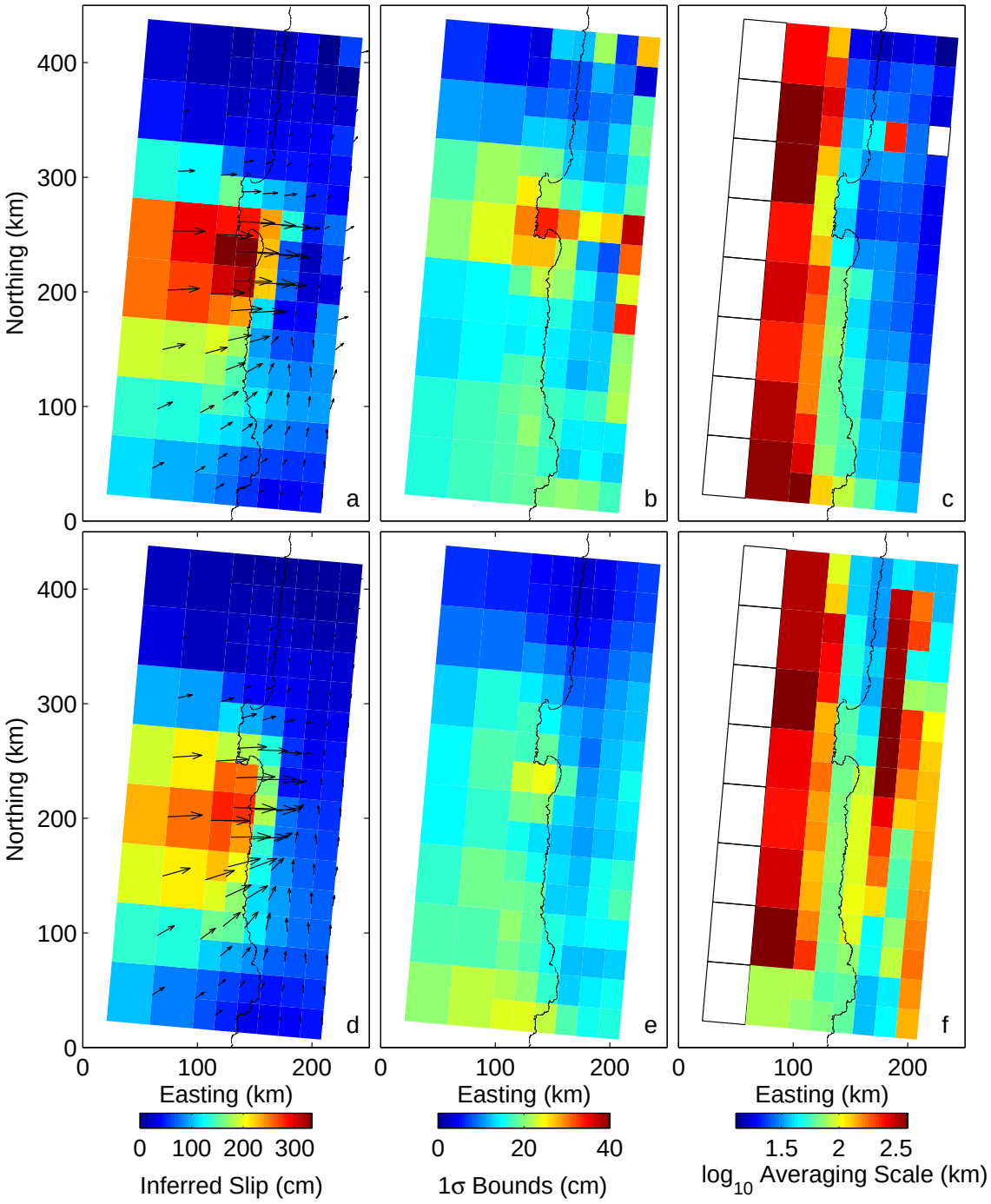

Figure 5.10: Constrained-slip inversion results for $p = 215$ (a-c) and $p = 0$ (d-f). Slip distributions (left) with arrows indicating coseismic motion of the subducting plate. 1σ error bounds (middle) constructed from bootstrap resampling of the dataset in Figure 5.7. Averaging scale, W (right), derived from best-fit Gaussian to each row of the empirical resolution matrix, R_e (See text). Empty patches indicate regions where the rows of R could not be fit by a Gaussian and does not represent a simple average of the area surrounding each patch.

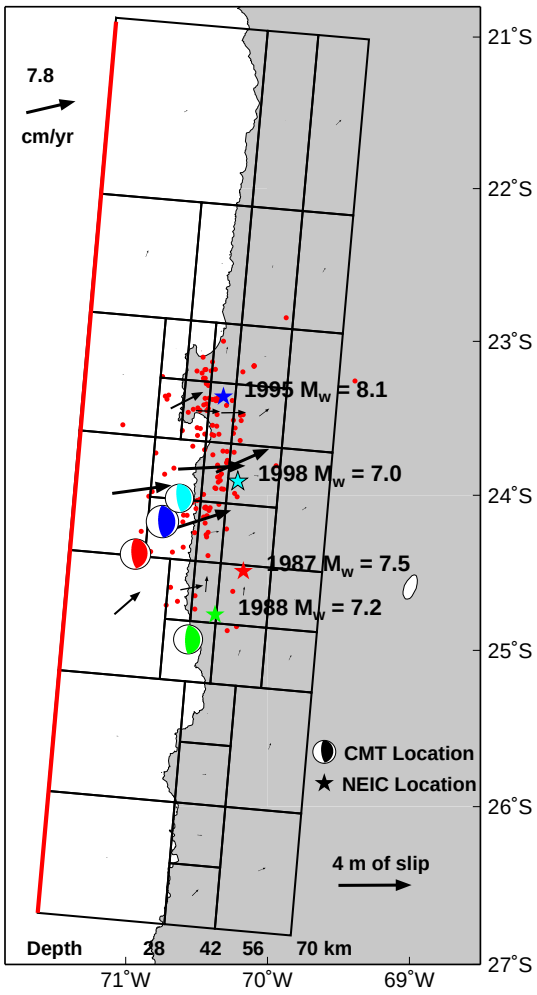

Figure 5.11: Slip distribution from *Pritchard et al.* (2002), Figure 6. Stars and moment tensors indicate the NEIC and Harvard CMT locations for M_w7-8 earthquakes between 1987 and 1998. Arrow in the upper left indicates the magnitude and direction of fault plane convergence (*DeMets et al.*, 1994).

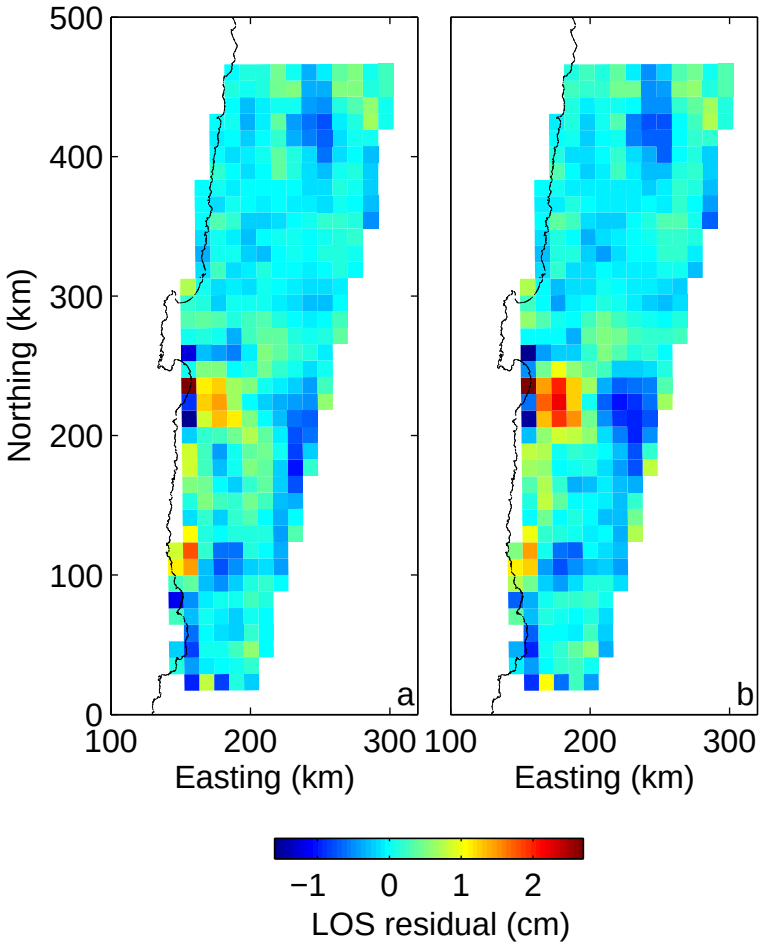

Figure 5.12: Residuals between data used in inversion for $p = 215$ (a) and $p = 0$ (b).

(colored curves in Figure 5.13) and computing ${}_j\mathcal{R}_i{}^r$, the data residual and the inferred slip in each case. In this case I find that ${}_j\mathcal{R}_i{}^r$ is actually minimized at slightly greater depths (Figure 5.13), although this may be explained by the fact that we could be using the correct fault plane location but are definitely not using the correct elastic structure for the subduction zone. The sensitivity of this inversion problem to 3-D variations in rheology needs to be explored further. I also note that the data residual decreases monotonically as the fault plane nears the surface, while the ${}_j\mathcal{R}_i{}^r$ increases. This implies that the shallower fault plane is able to better fit the noise in the data, but not the underlying signal. Also note that for the range of "low" ${}_j\mathcal{R}_i$, the inferred slip models are very similar (Figure 5.13e, f).

5.4 Conclusions

As the spatial and temporal coverage of geodetic datasets available continue to expand, the following developments are required if we are to rapidly and efficiently characterize a given earthquake soon after it occurs.

1. Methods for appropriately combining different types of geodetic data (i.e., InSAR, GPS, leveling)

2. A robust algorithm for choosing the appropriate fault plane parameterization and inversion regularization

3. Techniques for assessing the contribution of modeling errors such as uncertainties in rheology

This combination of tools will facilitate the development of joint seismic-geodetic inversions and the enable us to assess characteristics of the inferred coseismic slip distributions such as the spatial complexity or depth-distribution of slip. Potential techniques for addressing modelling errors include simulating realistically complex rheologies with finite element methods in order to characterize the magnitude of errors introduced by inadequate knowledge of the crustal rheology. In this chapter I

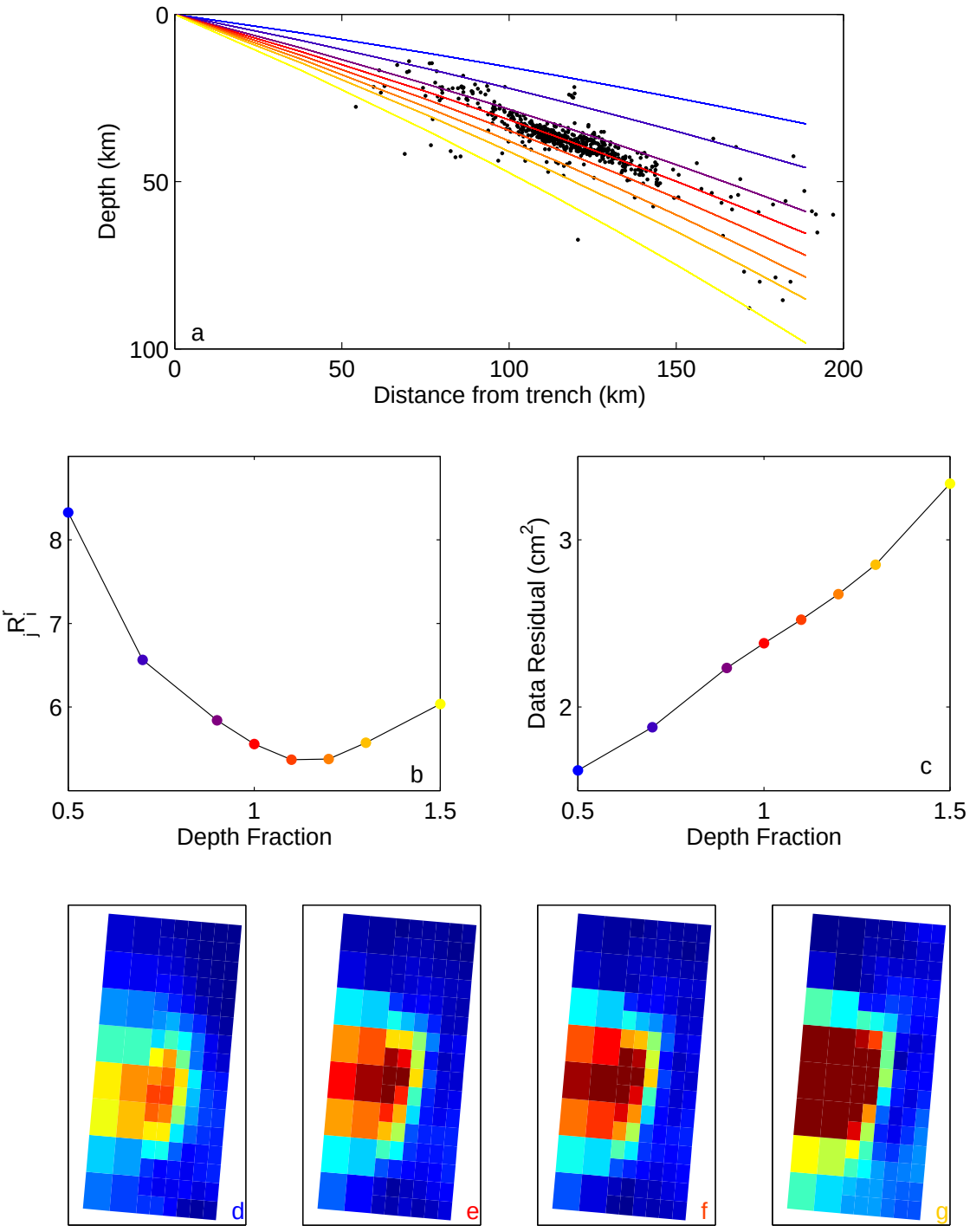

Figure 5.13: a) Potential fault plane parameterizations (colored lines) and aftershocks from *Husen et al.* (1999) (black dots). b) ${}_j\mathcal{R}_i{}^r$ and c) data residual associated with inferred slip distributions for each geometry in (a). d-g) Inferred slip distributions for fault geometries with dip fractions 0.5, 1, 1.1 and 1.5. Color scale and axes are same as in Figure 5.10a.

demonstrated that for some cases (i.e., subduction zone earthquakes) the ${}_j\mathcal{R}_i$ method can aid in the process of developing the correct inversion scheme, including the choice of fault plane geometry. In other cases (i.e., the Hector Mine earthquake), further work on optimizing fault plane choice is required. The fact that the ${}_j\mathcal{R}_i$ method can find the "correct" fault plane in synthetic scenarios for small perturbations of the fault plane geometry is encouraging. In realistic settings, where we may have significant uncertainty on the fault plane parameters, we must continue to quantify the robustness of inversions for coseismic slip.

Chapter 6

Concluding thoughts

During the course of my thesis work, I have attempted to optimize our use of geodetic data types (e.g., InSAR, GPS, pixel tracking) in applications ranging from earthquake location to the characterization of coseismic slip distributions. One of the unifying themes within this thesis is the quantification of the full range of model parameters (e.g., slip distributions, deformation source locations) that are consistent with a particular set of data and the associated errors. One facet of this theme is the need to present inversion results in a manner that illuminates an often very multi-dimensional solution space. The presentation of error bounds and averaging or smoothing scale associated with a given coseismic slip model within this thesis is one attempt to put inversion results in a format that the reader can independently assess without being fully acquainted with every aspect of the inverse problem.

I also address how inadequacies in the parameterization of inversions for earthquake parameters can bias the inferred results or produce unrealistically small error bounds on the solution. I explore the effects of errors such as wrong fault plane geometries, spatially coarse fault plane parameterizations and incorrect knowledge of the noise covariance matrix. Other important potential sources of error that need to be assessed in the future include variations in 3-D elastic structure and the inclusion of extraneous deformation sources such as ground water extraction, poroelastic deformation and viscoelastic relaxation in response to an earthquake.

I explore how the inversion tools themselves restrict the range of model parameters that we explore, and how significant these restrictions are to the final conclusions

about the inferred model. In Chapter 4, I explore definitions of model smoothness beyond the traditional definition of a roughness criterion, making a new family of slip models available to the inversion. As we push the limits of what the data can resolve and seek to progressively refine our conclusions, we must examine how the mechanics of inversion regularization affect what we can infer from the data. *Song and Simons* (2003) and *Wells et al.* (2003) observe that most of the slip in large subduction earthquakes is correlated with negative trench-parallel gravity anomalies and with topographic basins. It also appears that most subduction zones exhibit some degree of aseismic slip (i.e., slow or silent earthquakes) downdip of the zone that ruptures coseismically (e.g., *Beroza and Jordan*, 1990; *Kanamori and Kikuchi*, 1993; *Hirose et al.*, 1999; *Freymueller et al.*, 2001; *Lowry et al.*, 2001; *McGuire and Segall*, 2003). Inversion constraints that do not rely on the smoothness of the model may be better able to resolve the spatial extent of slip (coseismic or aseismic) in deep subduction zone environments. Future work will consist of examining different types of end member models such as the most spatially compact slip model that fits the data. Comparisons between the smoothest and most spatially compact slip models will provide a more complete sense of the full family of solutions that are consistent with the observations.

Appendix: Introduction to radar interferometry

In this thesis I use a combination of datatypes including interferometric synthetic aperture radar (InSAR), Global Positioning System (GPS) observations and seismic data. InSAR provides spatially dense (pixel sizes of order $10^1 - 10^2$ meters) observations with accuracies of less than 1 cm over swaths greater than 100 km in width ("across track") and over arbitrarily large distances in the direction of satellite travel ("along track"). InSAR observations are sensitive to a combination of atmospheric characteristics, topography, changes in reflective properties of the surface and ground deformation. Full treatments of the techniques, sensitivities and sources of error involved in InSAR are plentiful (e.g., *Griffiths*, 1995; *Gens and van Genderen*, 1996; *Massonnet and Feigl*, 1998; *Rosen et al.*, 2000; *Hanssen*, 2001).

To form a synthetic aperture radar (SAR) image, radar signals are transmitted from a moving platform (satellite, aircraft or space shuttle) and the phase and amplitude of the return is recorded (Figure A.1). The processing of SAR imagery is treated at length by various authors (e.g., *Curlander and McDonough*, 1991; *Price*, 1999). The phase in an individual SAR image appears to be white noise (Figure A.2), because the phase return from an individual pixel (length scale of order 10 m) is the result of the combination of the interaction of all scatterers within a pixel at the scale of the radar wavelengths (typically a few cm). However, as long as the scatterers within each pixel remain coherent in time, the phase difference between two separate SAR images will vary from pixel to pixel in a coherent manner (Figure A.2c). Interferograms with non-zero baseline distance between the two images (**B**, Figure A.1) are sensitive to topography and can be used to generate digital elevation models (DEM). Some care

must be taken in interpreting these DEM's, since any variations in atmospheric water content or ionospheric character can introduce elevation artifacts. The best results are achieved when several independent interferograms are averaged together to reduce the effects of atmospheric noise, or when the two images are acquired simultaneously (i.e., Shuttle Radar Topography Mission (SRTM) or Topographic Synthetic Aperture Radar (TOPSAR)) . When our goal is to measure surface deformation, we must either use interferograms with very short baselines, or remove the effect of topography using a pre-existing DEM (Figure A.2d, e) or by using an interferogram that spans no deformation (the 4- or N-pass method).

In cases where the reflective properties of the surface change dramatically between acquisitions of the two SAR images, the interferogram may become decorrelated (blue and purple regions in Figure A.2f). For most practical applications, decorrelation occur wherever the change in phase between neighboring pixels becomes greater than $\sim$1/2 wavelength (e.g., *Zebker and Villasenor*, 1992; *Rosen et al.*, 2000; *Hanssen*, 2001). Very high rates of deformation, even if varying smoothly across the image, can induce decorrelation, as can steep topography, landslides, sand dunes, agriculture, snow, or vegetation changes.

Because InSAR measures changes in range between the satellite and the ground, interferograms are only sensitive to the component of surface deformation that is in the line-of-sight (LOS) direction of the satellite. For some deformation sources, having data for only one component of the full 3-D deformation field (as is the case for most studies using geodetic data) can lead to ambiguities in the source location, fault plane orientation, or slip distribution (Chapter 2). Knowledge of additional components of the deformation field can help resolve these ambiguities. With InSAR data, we can obtain multiple components if we use observations from different satellite orbital geometries (e.g., overlapping satellite tracks or ascending vs. descending satellite passes) and by combining interferograms with pixel tracking of SAR images (e.g., *Fialko et al.*, 2001; *Michel and Avouac*, 2002; *Simons et al.*, 2002). Pixel tracking, or azimuth offsets, provides a horizontal component of deformation perpendicular to the LOS direction, albeit with precisions on the order of a fraction of a pixel (10's

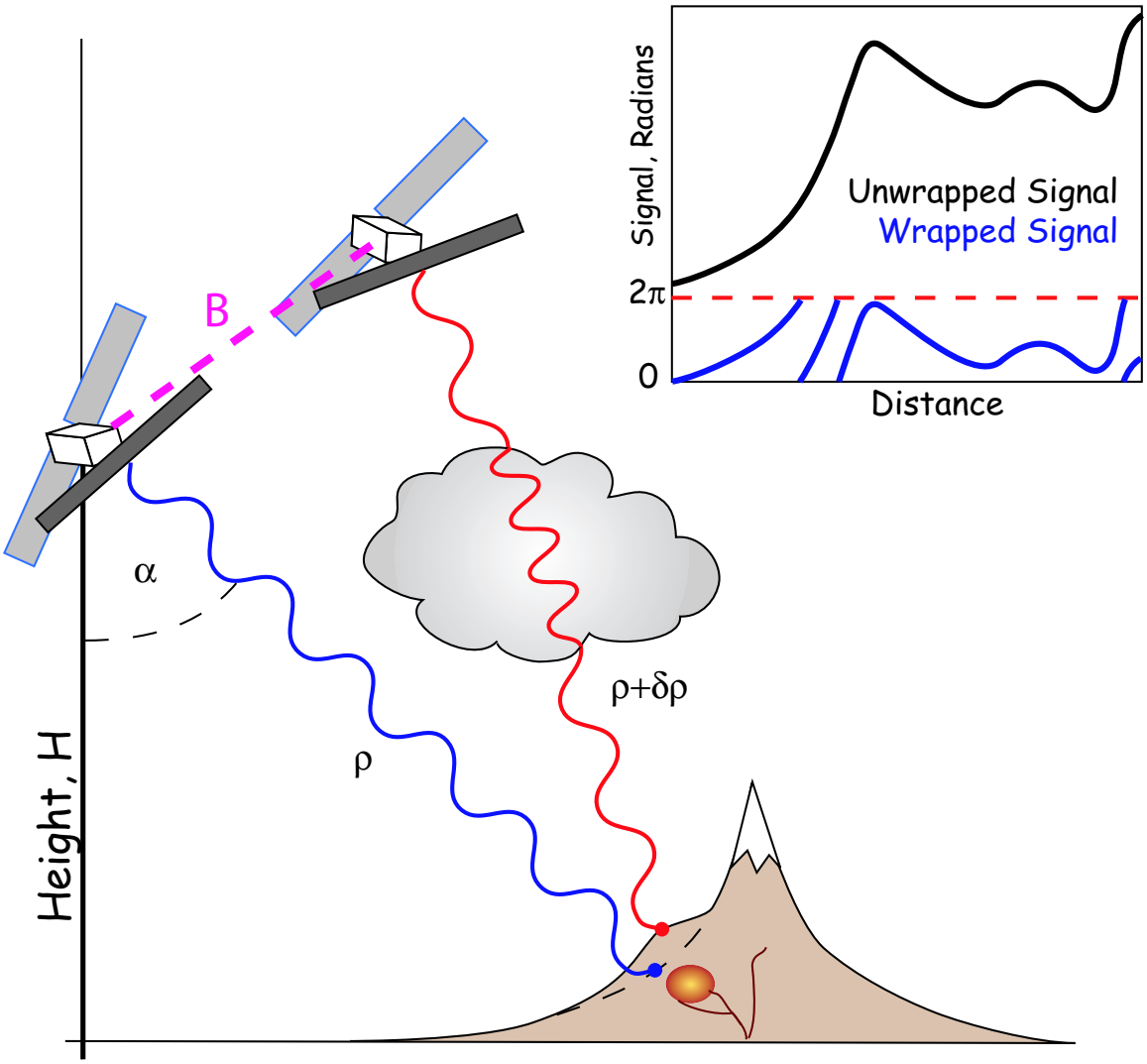

Figure A.1: Repeat-pass InSAR geometry: One or more radar satellites observe the Earth's surface at two discrete times at locations (red and blue radar signals) separated in space by a baseline **B**. The range, ρ, between the satellite and the ground is a function of topography, satellite look angle α, satellite height H and any atmospheric delays that may introduce additional phase cycles along the radar path. Precise knowledge of the orientation and length of **B** is necessary to convert $\delta\rho$ into elevation changes across the image. Since the interferogram only measures $\delta\rho$ to within $\pm 2\pi$ ("wrapped phase"), we must unwrap all of the different 0-2π segments across the image to form a continuous map of line-of-sight (LOS) displacement(Shown schematically in inset).

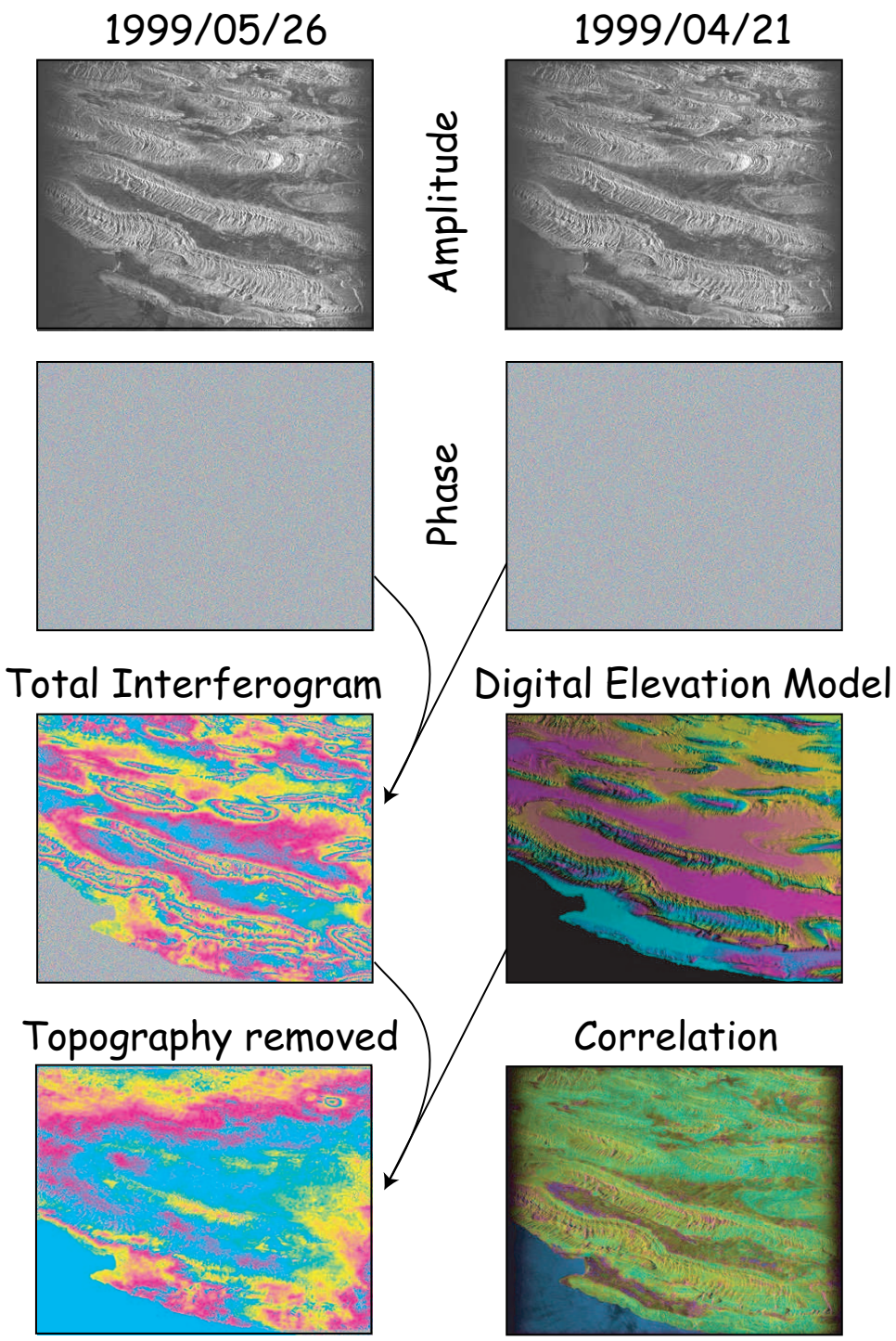

Figure A.2: Interferogram formation: Amplitude and phase for two SAR images of the Zagros mountains of southern Iran, separated in time by a month. Note the elliptical signal in the upper-right of the topography-free interferogram (see Chapter 3). Other features correspond to variations in atmospheric water vapor and other noise. Decorrelated regions in lower left of correlation map (yellow=high correlation, purple=low) correspond to the Persian Gulf.

of cm) rather than a fraction of a radar wavelength. In the future, InSAR data from both left- and right-looking geometries may become available, providing additional observation directions.

Any errors in knowledge of the length and orientation of the baseline between the two satellite acquisition locations (**B**, Figure A.1) result in errors in the inferred range change. In a typical interferogram, the baseline between the satellites changes smoothly across the image so that the result of baseline errors has a functional form similar to a quadratic function across the image. The uncertainty in baseline requires that we simultaneously account for this ramp in our interpretation of the inteferogram.

All interferograms discussed in this thesis were derived using the InSAR processing suite ROI_PAC (Repeat Orbit Interferometry Package), developed at the Jet Propulsion Laboratory (JPL) and Caltech (*Rosen et al.*, 2004).

Bibliography

Agnew, D. C., S. Owen, Z. K. Shen, G. Anderson, J. Svarc, H. Johnson, K. E. Austin, and R. Reilinger, Coseismic displacements from the Hector Mine, California, earthquake: Results from survey-mode global positioning system measurements, *Bull. Seism. Soc. Amer*, *92*, 1355–1364, 2002.

Akaike, H., *Bayesian Statistics*, chap. Likelihood and the Bayes procedure, pp. 143–166, University Press, Valencia, Spain, 1980.

Ambraseys, N. N., Reassessment of earthquakes, 1900-1999, in the Eastern Mediterranean and the Middle East, *Geophys. J. Int.*, *145*, 471–486, 2001.

Árnadóttir, T., and P. Segall, The 1989 Loma Prieta earthquake imaged from inversion of geodetic data, *J. Geophys Res.*, *99*, 21,835–21,855, 1994.

Barrientos, S. E., and S. N. Ward, The 1960 Chile earthquake: Inversion for slip distribution from surface deformation, *Geophys. J. Int.*, *103*, 589–598, 1990.

Berberian, M., Active faulting and tectonics of Iran, in *Zagros-Hindu Kush-Himalaya Geodynamic Evolution*, edited by H. K. Gupta and F. M. Delany, vol. 3 of *Geodynamics Series*, pp. 33–69, Amer. Geophys. Union, 1981.

Beroza, G. C., and T. H. Jordan, Searching for slow and silent earthquakes using free oscillations, *J. Geophys. Res.*, *95*, 2485–2510, 1990.

Carlo, D. L., T. Lay, C. J. Ammon, and J. Zhang, Rupture process of the 1995 Antofagasta subduction earthquake (M_w=8.1), *Pure Appl. Geophys.*, *154*, 677–709, 1999.

Cervelli, P., M. H. Murray, P. Segall, Y. Aoki, and T. Kato, Estimating source parameters from deformation data, with an application to the March 1997 earthquake swarm off the Izu Peninsula, Japan, *J. Geophys. Res.*, *106*, 11,217–11,237, 2001.

Chen, J., D. J. Wald, and D. V. Helmberger, Source description of the 1999 Hector Mine, California, earthquake, part I: Wavelet domain inversion theory and resolution analysis, *Bull. Seism. Soc. Amer.*, *92*, 1192–1207, 2002a.

Chen, J., D. J. Wald, and D. V. Helmberger, Source description of the 1999 Hector Mine, California, earthquake, part II: Complexity of slip history, *Bull. Seism. Soc. Amer.*, *92*, 1208–1226, 2002b.

Chlieh, M., Le cycle sismique dcrit avec les donnes de la godsie spatiale (interfromtrie sar et gps diffrentiel) : Variations spatio-temporelles des glissements stables et instables sur l interface de subduction du nord chili, Ph.D. thesis, Institut de Physique du Globe de Paris, 2003.

Curlander, J., and R. N. McDonough, *Synthetic aperture radar: Systems and signal processing*, Wiley, New York, 1991.

Delouis, B., T. Monfret, L. Dorbath, M. Pardo, L. Rivera, D. Comte, H. Haessler, J. P. Caminade, L. Ponce, E. Kausel, and A. Cisternas, The M_w=8.0 Antofagasta (Northern Chile) earthquake of 30 July 1995: A precursor to the end of the large 1877 gap, *Bull. Seism. Soc. Am.*, *87*, 427–445, 1997.

DeMets, C., R. G. Gordon, D. F. Argus, and S. Stein, Effect of recent revisions to the geomagnetic reversal time scale on estimates of current plate motions, *Geophys. Res. Lett.*, *21*, 2191–2194, 1994.

Dieterich, J. H., Modeling of rock friction, 1. experimental results and constitutive equations, *J. Geophys. Res.*, *84*, 2161–2168, 1979.

Dieterich, J. H., Earthquake nucleation on faults with rate- and state- dependent strength, *Tectonophysics*, *211*, 115–134, 1992.

Du, Y., A. Aydin, and P. Segall, Comparison of various inversion techniques as applied to the determination of a geophysical deformation model for the 1983 Borah Peak earthquake, *Bull. Seism. Soc. Amer.*, *82*, 1840–1866, 1992.

Efron, B., and G. Gong, A leisurely look at the bootstrap, the jackknife, and cross-validation, *Amer. Stat.*, *37*, 36–48, 1983.

Emardson, T. R., M. Simons, and F. H. Webb, Neutral atmospheric delay in interferometric synthetic aperture radar applications: Statistical description and mitigation, *J. Geophys. Res.*, *108*, doi:10.1029/2002JB001,781, 2003.

Ferrill, D. A., S. M. J. J. A. Stamatakos, H. L. M. B. Rahe, R. H. Martin, and A. P. Morris, Quaternary slip history of the Bare Mountain fault (Nevada) from the morphology and distribution of alluvial fan deposits, *Geology*, *24*, 559–562, 1996.

Fialko, Y., M. Simons, and D. Agnew, The complete (3-D) surface displacement field in the epicentral area of the 1999 M_w 7.1 Hector Mine earthquake, California, from space geodetic observations, *Geophys. Res. Lett.*, *28*, 3063–3066, 2001.

Freymueller, J., N. E. King, and P. Segall, The co-seismic slip distribution of the Landers earthquake, *Bull. Seism. Soc. Amer.*, *84*, 646–659, 1994.

Freymueller, J., C. Zweck, J. Fletcher, S. Hreinsdottir, S. C. Cohen, and M. Wyss, The great Alaska "earthquake" of 1998-2001, *EOS*, *82*, 1, 2001.

Fridrich, C. J., Tectonic evolution of the Crater Flat basin, Yucca Mountain region, Nevada, *Spec. Paper - Geol. Soc. Amer.*, *333*, 169–195, 1999.

Fridrich, C. J., J. W. Whitney, M. R. Hudson, , and B. M. Crowe, Space-time patterns of late Cenozoic extension, vertical axis rotation, and volcanism in the Crater Flat basin, Southwest Nevada, *Spec. Paper - Geol. Soc. Amer.*, *333*, 197–212, 1999.

Frizzell, V. A., and J. C. Shulters, Geologic map of the Nevada Test Site, southern Nevada, scale 1:100,000, U.S. Geol. Surv. Rep., I-2046, 1990.

Gens, R., and J. L. van Genderen, SAR interferometry – Issues, techniques, applications, *Int. J. Remote Sensing*, *17*, 1803–1835, 1996.

Goldstein, R., Atmospheric limitations to repeat-track radar interferometry, *Geophys. Res. Lett.*, *22*, 2517–2520, 1995.

Griffiths, H., Interferometric synthetic aperture radar, *Electron. Commun. Eng. J.*, *7*, 247–256, 1995.

Hadley, D., and H. Kanamori, Seismic structure of the Transverse Ranges, California, *Geol. Soc. Amer. Bull.*, *88*, 1469–1478, 1977.

Hansen, P. C., *Rank-deficient and discrete ill-posed problems: Numerical aspects of linear inversion*, SIAM, Philadelphia, 1998.

Hanssen, R. A., *Radar interferometry: Data interpretation and error analysis*, Kluwer Academic Publishers, Dordrecht, The Netherlands, 2001.

Harmsen, S. C., The Little Skull Mountain, Nevada, earthquake of 29 June 1992: Aftershock focal mechanisms and tectonic stress field implications, *Bull. Seism. Soc. Amer.*, *84*, 1484–1505, 1994.

Harris, R. A., and P. Segall, Detection of a locked zone at depth on the Parkfield, California, segment of the San Andreas Fault, *J. Geophys. Res.*, *92*, 7945–7962, 1987.

Heizler, M. T., F. V. Perry, B. M. Crowe, L. Peters, and R. Appelt, The age of Lathrop Wells volcanic center; an $^{40}Ar/^{39}Ar$ dating investigation, *J. Geophys. Res.*, *104*, 767–804, 1999.

Hessami, K., H. A. Koyi, and C. J. Talbot, The significance of strike-slip faulting in the basement of the Zagros fold and thrust belt, *J. Pet. Geol.*, *24*, 5–28, 2001.

Hirose, H., K. Hirahara, F. Kimata, N. Fujii, and S. Miyazaki, A slow thrust slip event following the two 1996 hyuganada earthquakes beneath the Bungo channel, southwest Japan, *Geophys. Res. Lett.*, *26*, 3237–3240, 1999.

Hreinsdottir, S., J. T. Freymueller, H. J. Fletcher, C. F. Larsen, and R. Burgmann, Coseismic slip distribution of the 2002 M_W7.9 Denali fault earthquake, Alaska, determined from GPS measurements, *Geophys. Res. Lett.*, *30*, doi:10.1029/2003GL017,408, 2003.

Husen, S., E. Kissling, E. Flueh, and G. Asch, Accurate hypocentre determination in the seismogenic zone of the subducting Nazca Plate in northern Chile using a combined on-/offshore network, *Geophys. J. Int.*, *138*, 687–701, 1999.

Ide, S., M. Takeo, and Y. Yoshida, Source process of the 1995 Kobe earthquake: Determination of spatio-temporal slip distribution by Bayesian modeling, *Bull. Seism. Soc. Amer.*, *86*, 547–566, 1996.

Ihmlé, P. F., and J.-C. Ruegg, Source tomography by simulated annealing using broad-band surface waves and geodetic data: Application to the M_w=8.1 Chile 1995 event, *Geophys. J. Int.*, *131*, 146–158, 1997.

Jackson, D. D., and M. Matsú'ura, A Bayesian approach to nonlinear inversion, *J. Geophys. Res.*, *90*, 581–591, 1985.

Jackson, J., and T. J. Fitch, Basement faulting and the focal depths of the larger earthquake in the Zagros mountains (Iran), *Geophys. J. R. Astr. Soc.*, *64*, 561–586, 1981.

Jackson, J., and D. McKenzie, The relationship between plate motions and seismic moment tensors, and the rates of active deformation in the Mediterranean and Middle East, *Geophsy. J. Int.*, *93*, 45–73, 1988.

Jones, L. E., and D. V. Helmberger, Earthquake source parameters and fault kinetics in the eastern California shear zone, *Bull. Seism. Soc. Amer.*, *88*, 1337–1352, 1998.

Jónsson, S., Modeling volcano and earthquake deformation from satellite radar interferometric observations, Ph.D. thesis, Stanford University, 2002.

Jónsson, S., H. Zebker, P. Segall, and F. Amelung, Fault slip distribution of the 1999 m_w 7.1 hector mine, california, earthquake, estimated from satellite radar and gps measurements, *Bull. Seism. Soc. Amer.*, *92*, 1377–1389, 2002.

Kanamori, H., and M. Kikuchi, The 1992 Nicaragua earthquake: a slow tsunami earthquake associated with subducted sediments, *Nature*, *361*, 714–716, 1993.

Klotz, J., D. Angermann, G. W. Michel, R. Porth, C. Reigber, J. Reinking, J. Viramonte, R. Perdomo, V. H. Rios, S. Barrientos, R. Barriga, and O. Cifuentes, GPS-derived deformation of the central Andes including the 1995 Antofagasta M_w=8.0 earthquake, *Pure Appl. Geophys.*, *154*, 709–730, 1999.

Larsen, S., R. Reilinger, H. Neugebauer, and W. Strange, Global Positioning System measurements of deformations associated with the 1987 Supersition Hills earthquake: Evidence for conjugate faulting, *J. Geophys. Res.*, *97*, 4885–4902, 1992.

Lohman, R., M. Simons, and B. Savage, Location and mechanism of the Little Skull Mountain earthquake as constrained by satellite radar interferometry and seismic waveform modeling, *J. Geophys. Res.*, *107*, doi:10.1029/2001JB000,627, 2002.

Lowry, A. R., K. M. Larson, V. Kostoglodov, and R. Bilham, Transient fault slip in Guerrero, southern Mexico, *Geophys. Res. Lett.*, *28*, 3753–3756, 2001.

Maggi, A., J. A. Jackson, K. Priestley, and C. Baker, A re-assessment of focal depth distributions in southern Iran, the Tien Shan and northern India: do earthquakes really occur in the continental mantle?, *Geophys. J. Int.*, *143*, 629–661, 2000.

Massonnet, D., and K. L. Feigl, Radar interferometry and its application to changes in the earth's surface, *Rev. Geophys.*, *36*, 441–500, 1998.

Matthews, M. V., and P. Segall, Estimation of depth-dependent fault slip from measured surface deformation with application to the 1906 San Francisco earthquake, *J. Geophys. Res.*, *98*, 12,153–12,163, 1993.

McGuire, J., and P. Segall, Imaging of aseismic fault slip transients recorded by dense geodetic networks, *Geophys. J. Int.*, *155*, 778–788, 2003.

McQuarrie, N., Crustal scale geometry of the Zagros fold-thrust belt, Iran, *J. Struct. Geol.*, *26*, 519–535, 2004.

Menke, W., *Geophysical Data Analysis: Discrete Inverse Theory*, vol. 45 of *International Geophysical Series*, revised ed., Academic Press, Inc., 1989.

Meremonte, M., J. Gomberg, and E. Cranswick, Constraints on the 29 June 1992 Little Skull Mountain, Nevada, earthquake sequence provided by robust hypocenter estimates, *Bull. Seism. Soc. Amer.*, *85*, 1039–1049, 1995.

Michel, R., and J. P. Avouac, Deformation due to the 17 August Izmit earthquake measured from spot images, *J. Geophys. Res.*, *107*, 10 1029/2000JB000,102, 2002.

Monfret, T., L. Dorbath, J. P. Caminade, M. Pardo, D. Comte, and L. Ponce, The July 30, Antofagasta earthquake: An 'hypocritical' seismic event (abstract), *Eos Trans. AGU*, *76*, 427, 1995.

Okada, Y., Surface deformation due to shear and tensile faults in a half space, *Bull. Seism. Soc. Amer.*, *75*, 1135–1154, 1985.

Price, E. J., Coseismic and postseismic deformations associated with the 1992 Landers, California, earthquake measured by synthetic aperture radar interferometry, Ph.D. thesis, University of California, San Diego, San Diego, CA, 1999.

Pritchard, M. E., M. Simons, P. A. Rosen, S. Hensley, and F. H. Webb, Co-seismic slip from the 1995 July 30 Mw = 8.1 Antofagasta, Chile, earthquake as constrained by InSAR and GPS observations, *Geophys. J. Intl.*, *150*, 362–376, 2002.

Reigber, C., G. W. Michel, J. Klotz, and D. Angermann, The Antofagasta 1995 earthquake: Crustal deformation pattern as observed by GPS and D-INSAR, in *Proceedings of ERS symposium on Space at the service of our environment, Florence, Italy*, vol. 414, pp. 507–513, 1997.

Rice, J. R., Constitutive relations for fault slip and earthquake instabilities, *Pure. Appl. Geophys.*, *121*, 443–475, 1983.

Romanowicz, B., D. Dreger, M. Pasyanos, and R. Uhrhammer, Monitoring of strain release in Central and Northern California using broadband data, *Geophys. Res. Lett.*, *20*, 1643–1646, 1993.

Rosen, P. A., S. Hensley, I. R. Joughin, F. K. Li, S. N. Madsen, E. Rodriguez, and R. M. Goldstein, Synthetic aperture radar interferometry, *Proc. of the IEEE*, *88*, 333–382, 2000.

Rosen, P. A., S. Hensley, G. Peltzer, and M. Simons, Updated repeat orbit interferometry package released, *EOS*, *85*, 2004.

Ruegg, J. C., J. Campos, R. Armijo, S. Barrientos, P. Briole, R. Thiele, M. Arancibia, J. Canuta, T. Duquesnoy, M. Chang, D. Lazo, H. Lyon-Caen, L. Ortlieb, J. C. Rossignol, and L. Serrurier, The M_w=8.1 Antofagasta (North Chile) earthquake July 30, 1995: First results from teleseismic and geodetic data, *Geophys. Res. Lett.*, *23*, 917–920, 1996.

Ruina, A. L., Slip instability and state variable friction laws, *J. Geophys. Res.*, *88*, 10,359–10,370, 1993.

Sagiya, T., and W. Thatcher, Coseismic slip resolution along a plate boundary megathrust: The Nankai Trough, southwest Japan, *J. Geophys. Res.*, *104*, 1111–1129, 1999.

Sambridge, M., Geophysical inversion with a neighborhood algorithm - I, Searching a parameter space, *Geophys. J. Int.*, *138*, 479–494, 1998a.

Sambridge, M., Geophysical inversion with a neighborhood algorithm - II, Appraising the ensemble, *Geophys. J. Int.*, *138*, 727–746, 1998b.

Savage, J. C., M. Lisowski, W. K. Gross, N. E. King, and J. L. Svarc, Strain accumulation near Yucca Mountain, Nevada, *J. Geophys. Res.*, *99*, 18,103–18,107, 1994.

Savage, J. C., J. L. Svarc, and W. H. Prescott, Strain accumulation at Yucca Mountain, Nevada, *J. Geophys. Res.*, *104*, 17,627–17,631, 1999.

Sawyer, D. A., R. J. Fleck, M. A. Lanphere, R. G. Warren, D. E. Broxton, and M. R. Hudson, Episodic caldera volcanism in the Miocene southwestern Nevada volcanic field: Revised stratigraphic framework, $^{40}Ar/^{39}Ar$ geochronology, and implications for magmatism and extension, *Geol. Soc. Amer. Bull.*, *106*, 1304–1318, 1994.

Segall, P., and R. Harris, Earthquake deformation cycle on the San Andreas Fault near Parkfield, California, *J. Geophys. Res.*, *92*, 10,511–10,525, 1987.

Simons, M., Y. Fialko, and L. Rivera, Coseismic deformation from the 1999 Mw 7.1 Hector Mine, California, earthquake as inferred from InSAR and GPS observations, *Bull. Seism. Soc. Amer.*, *92*, 1390–1402, 2002.

Smith, K. D., J. N. Brune, D. dePolo, M. K. Savage, R. Anooshehpoor, and A. F. Sheehan, The 1992 Little Skull Mountain earthquake sequence, Southern Nevada Test Site, *U. S. Geol. Surv. Digital Data Series DDS-058*, *Chapter K*, 1–16, 2000.

Song, A. T., and M. Simons, Large trench-parallel gravity variations predict seismogenic behavior in subduction zones, *Science*, *301*, 630–633, 2003.

Talebian, M., and J. Jackson, Offset on the main recent fault of NW Iran and implications for the late Cenozoic tectonics of the Arabia-Eurasia collision zone, *Geophys. J. Int.*, *150*, 422–439, 2002.

Talebian, M., and J. Jackson, A reappraisal of earthquake focal mechanisms and active shortening in the Zagros mountains of Iran, *Geophys. J. Int.*, *156*, 506–526, 2004.

Tarantola, A., and B. Valette, Inverse problems = quest for information, *J. Geophys.*, *50*, 159–170, 1982a.

Tarantola, A., and B. Valette, Generalized nonlinear inverse problems solved using the least squares criterion, *Rev. Geophys. and Space Phys.*, *20*, 219–232, 1982b.

Tatarski, V. L., *Wave propagation in a turbulent medium*, McGraw-Hill, New York, 1961.

Treiman, J. A., K. J. Kendrick, W. A. Bryant, T. K. Rockwell, and S. F. McGill, Primary surface rupture associated with the m_w 7.1 16 October 1999 Hector Mine earthquake, San Bernadino County, California, *Bull. Seism. Soc. Amer.*, *92*, 1171–1191, 2002.

Tse, S., and J. Rice, Crustal earthquake instability in relation to the depth variation of frictional slip properties, *J. Geophys. Res.*, *91*, 9452–9472, 1986.

Wallace, R. E., Patterns and timing of late Quaternary faulting in the Great Basin Province and relation to some regional tectonic features, *J. Geophys. Res.*, *89*, 5763–5769, 1984.

Walter, W., Source parameters of the June 29, 1992 Little Skull Mountain earthquake from complete regional waveforms at a single station, *Geophys. Res. Lett.*, *20*, 403–406, 1993.

Wang, C. Y., and R. B. Herrmann, A numerical study of P, SV, and SH-wave generation in a plane layered medium, *Bull. Seism. Soc. Amer.*, *70*, 1015–1036, 1980.

Ward, S., and G. R. Valensie, Fault parameters and slip distribution of the 1915 Avezzano, Italy, earthquake derived from geodetic observations, *Bull. Seism. Soc. Amer.*, *79*, 690–710, 1989.

Wells, R. E., R. J. Blakely, Y. Sugiyama, D. W. Scholl, and P. A. Dinterman, Basin-centered asperities in great subduction zone earthquakes: A link between slip, subsi-

dence, and subduction erosion, *J. Geophys. Res.*, *108*, doi:10.1029/2002JB002,072, 2003.

Wernicke, B., J. L. Davis, R. A. Bennett, P. Elosegui, M. J. Abolins, R. J. Brady, M. A. House, N. A. Niemi, and J. K. Snow, Anomalous strain accumulation in the Yucca Mountain area, Nevada, *Science*, *279*, 2096–2100, 1998.

Williams, S., Y. Bock, and P. Fang, Integrated satellite interferometry: Tropospheric noise, gps estimates and implication for interferometric synthetic aperture radar products, *J. Geophys. Res.*, *103*, 27,051–27,067, 1998.

Yabuki, T., and M. Matsu'ura, Geodetic data inversion using a Bayesian information criterion for spatial distribution of fault slip, *Geophys. J. Int.*, *109*, 363–375, 1992.

Zebker, H. A., and J. Villasenor, Decorrelation in interferometric radar echoes, *IEEE Trans. Geo. Rem. Sensing*, *30*, 950–959, 1992.

Zebker, H. A., P. A. Rosen, and S. Hensley, Atmospheric effects in interferometric synthetic aperture radar surface deformation and topographic maps, *J. Geophys. Res.*, *102*, 7547–7563, 1997.

Zhao, L., and D. V. Helmberger, Source estimation from broadband regional seismograms, *Bull. Seism. Soc. Amer.*, *84*, 91–104, 1994.

Zreda, M. G., F. M. Phillips, P. W. Kubik, P. Sharma, and D. Elmore, Cosmogenic ^{36}Cl dating of a young basaltic eruption complex, Lathrop Wells, Nevada, *Geology*, *82*, 57–60, 1993.